U.S.NRC
United States Nuclear Regulatory Commission
Protecting People and the Environment

NUREG/CR-6964
ANL-07/12

Crack Growth Rates and Metallographic Examinations of Alloy 600 and Alloy 82/182 from Field Components and Laboratory Materials Tested in PWR Environments

Office of Nuclear Regulatory Research

U.S.NRC
United States Nuclear Regulatory Commission
Protecting People and the Environment

NUREG/CR-6964
ANL-07/12

Crack Growth Rates and Metallographic Examinations of Alloy 600 and Alloy 82/182 from Field Components and Laboratory Materials Tested in PWR Environments

Manuscript Completed: February 2008
Date Published: May 2008

Prepared by
B. Alexandreanu, O.K. Chopra, and W. J. Shack

Argonne National Laboratory
Argonne, IL 60439

S. Crane and H.J. Gonzalez, NRC Project Managers

NRC Job Code Y6388

Office of Nuclear Regulatory Research

This page is intentionally left blank.

Abstract

In light water reactors, components made of nickel-base alloys are susceptible to environmentally assisted cracking. This report summarizes the crack growth rate results and related metallography for field and laboratory-procured Alloy 600 and its weld alloys tested in pressurized water reactor (PWR) environments. The report also presents crack growth rate (CGR) results for a shielded-metal-arc weld of Alloy 182 in a simulated PWR environment as a function of temperature between 290°C and 350°C. These data were used to determine the activation energy for crack growth in Alloy 182 welds. The tests were performed by measuring the changes in the stress corrosion CGR as the temperatures were varied during the test. The difference in electrochemical potential between the specimen and the Ni/NiO line was maintained constant at each temperature by adjusting the hydrogen overpressure on the water supply tank. The CGR data as a function of temperature yielded activation energies of 252 kJ/mol for a double-J weld and 189 kJ/mol for a deep-groove weld. These values are in good agreement with the data reported in the literature. The data reported here and those in the literature suggest that the average activation energy for Alloy 182 welds is on the order of 220-230 kJ/mol, higher than the 130 kJ/mol commonly used for Alloy 600. The consequences of using a larger value of activation energy for SCC CGR data analysis are discussed.

This page is intentionally left blank.

Foreword

This report presents crack growth rate (CGR) data and the results of the corresponding fracture surface and metallographic examinations from cyclic loading and primary water stress-corrosion cracking (PWSCC) tests of two nickel-base Alloy 182 (A182) weldments. These weldments are typical of those used in vessel penetrations and piping butt welds in nuclear power plants. The effect of crack orientation with respect to dendrite orientation is the most significant variable investigated in this study. However, this report also compiles data from other laboratories that describe the effects of material composition, loading characteristics, and chemistry of the aqueous environment. The PWSCC growth rates described for the A182 specimens in the report are comparable to the CGR that characterize the performance of Alloy 600 (A600).

This report is one of a series of reports documenting the results of CGR testing in vessel head penetration materials. This report focuses on the Alloy 82 (A82) and A182 weld metals. This report also presents results from tests of the A600 base metal. The researchers tested (1) a laboratory-fabricated, shielded-metal-arc deposit of A182; (2) a weldment sample from the J-groove weld of a control rod drive mechanism nozzle from the Davis–Besse Nuclear Power Plant; and (3) a hot leg nozzle-to-safe end weld from the Virgil C. Summer Nuclear Station.

The objective of the research was to generate PWSCC crack growth rates in A82 and A182 assist NRC in determining the validity and acceptability of licensee flaw analyses Title 10 of the *Code of Federal Regulations* Part 50.55a (10 CFR 50.55a). In addition, the results will also assist NRC in its review of licensees' requests for relief to some in-service inspection requirements of 10 CFR 50.55a, if submitted.

This page is intentionally left blank.

Contents

Abstract iii

Foreword v

Executive Summary xiii

Acknowledgments xv

Acronyms and Abbreviations xvii

1 Introduction 1

2 Experimental 3

2.1 Material and Specimen Design 3

2.2 Test Facilities 5

2.2.1 Facility with 6-Liter Autoclave 5

2.2.2 Facility with 1-Liter Autoclave 6

2.2.3 Facility with a 2-Liter Autoclave 8

2.2.4 Primary Water Environment 10

2.3 Test Procedure 13

2.4 Analysis of Crack Growth Rate Data 14

3 Microstructural Characterization 17

3.1 Laboratory-Prepared Alloys 17

3.2 Field Alloys 19

4 Crack Growth Test Results 23

4.1 Double-J Weld Specimen A182-1 23

4.2 Deep-Groove Weld Specimen CT933H-1 26

4.3 Deep-Groove Weld Specimen CT933H-2 28

5. Discussion 31

5.1. SCC Growth Rates 31
5.1.1 Alloy 600 31
5.1.2 Ni-Alloy Welds 32
5.2. Activation Energy for SCC Crack Growth 36
5.3. Consequence of Using a Larger Activation Energy 39
5.4 Cyclic Crack Growth Rates in PWR Environment 40
5.4.1 Alloy 600 40
5.4.2 Ni-Alloy Welds 43
6 Summary 47
References 49
Appendix A: Crack Growth Rate Data for Davis-Besse and V. C. Summer Ni-base alloys 55

Figures

1. Configuration of the 1-T and 1/2-T CT specimens used for this study. 3

2. Schematic of the weld joint design and weld passes for Alloy 182 SMA double-J weld and the deep-groove weld. 4

3. Orientation of the CT specimens from the Alloy 182 SMA double-J weld and the deep-groove weld. 4

4. Photograph of the specimen load train. 5

5. Schematic diagram of the recirculating 6-liter autoclave system. 6

6. Photograph of the specimen load train for the 1-liter autoclave. 7

7. Schematic diagram of the recirculating 1-liter autoclave system. 8

8. Layout of the 2-liter autoclave system. 9

9. Photograph of the specimen load train for the 2-liter autoclave. 9

10. Schematic diagram of the recirculating 2-liter autoclave system. 10

11. Hydrogen concentration at Ni/NiO phase transition as a function of temperature. 12

12. Dendritic microstructure on a laboratory-preapred Alloy 182 weld specimen. 17

13. Micrograph showing one of the matrix precipitates observed on the surface of sample 3A and EDX spectra resulting from the bulk and the precipitate. 17

14. OIM maps from a plane parallel to the direction of dendrites showing the grain orientations. 18

15. Grain boundary character distribution for laboratory-prepared welds. 19

16. Microstructures observed on planes 03-1 and 03-2 of the CRDM nozzle alloy. 20

17. Microstructure observed on the Alloy 182 J-groove weld specimen from Davis-Besse. 20

18. Microstructure of the butter Alloy 182. 21

19. Microstructure of the weld Alloy 82 from the V.C. Summer plant. 21

20. Grain boundary sliding at the weld-pipe interface 21

21. Fracture surface of specimen A182-1: optical image and SEM image. 24

22. Crack length vs. time for Alloy 182 weld specimen A182-1 in simulated PWR environment during test periods precracking, 1-2, 3, and 4-7. 25

23. Fracture surface of Alloy 182 weld specimen CT933H-1 tested in simulated PWR environment at temperatures of 290-310°C. 26

24. Crack length vs. time for Alloy 182 weld specimen CT933H-1 in simulated PWR environment during test periods precracking-2, 3-4, 5-6, and 7-8. 27

25. Fracture surface of Alloy 182 weld specimen CT933H-2 tested in simulated PWR environment at temperatures of 290-350°C. 29

26. Crack length vs. time for Alloy 182 weld specimen CT933H-2 in simulated PWR environment during test periods 1-5, 6-12, and 13-18. 30

27. CGR data for Alloy 600 from Davis-Besse CRDM nozzle #3 in PWR water at 316°C under constant load and log-normal distribution of constant α for 26 heats of Alloy 600. 31

28. Transition from TG to IG fracture mode in specimen N3CL-1. 32

29. SCC crack growth data for the Argonne Alloy 182 welds plotted as a function of K and compared with the available data for Alloy 182 and 82 welds in simulated PWR environment. 33

30. CGR data for Alloy 182 from the Davis-Besse CRDM nozzle J-groove weld in PWR environment at 316°C under constant load. 34

31. Comparison of the CGR data for the V.C. Summer weld and butter alloys with the data obtained on laboratory-prepared welds in the present study and V.C. Summer weld and butter alloys by Jacko et al. 35

32. Log-normal distribution of constant α for several heats of Alloy 82 and 182. 35

33. Micrographs from the fracture surface of weld specimens: Davis-Besse J11CC-1, and V.C. Summer BCR-01. 36

34. Temperature dependence of the CGR data for Alloy 82 obtained at Bechtel Bettis, ETH, and Lockheed Martin at temperatures between 290°C and 360°C. 37

35. Temperature dependence of the CGR data for Alloy 182 obtained at Westinghouse and CEA at temperatures between 290°C and 340°C. 37

36. Temperature dependence of the CGR data for Alloy 182 obtained at ANL at temperatures between 290°C and 350°C. 38

37. Comparison of observed activation energies for Alloy 182 with a normal distribution. 38

38. Cumulative distribution of the parameter α in the CGR relationship for Ni-alloy welds with the data normalized to 325°C using an activation energy of 130 kJ/mol and 220 kJ/mol. 39

39. CGR data for the V.C. Summer weld and Davis-Besse weld alloys. 40

40. Cyclic CGR data for several Alloy 600 heats in deaerated water at 320°C under cyclic loading.. 41

41. CGR data for Davis-Besse CRDM nozzle #3 Alloy 600 in PWR water at 316°C under cyclic loading..... 42

42. CGR data in PWR environment for Alloy 182 SMA weld at 320°C, and Alloy 82 and Alloy 52 welds at 315°C as a function of the growth rates for Alloy 182 weld in air. 43

43. Transition from TG to IG fracture and higher magnification micrograph of the boxed area showing the tip of a few secondary cracks. 44

44 CGR data for Alloy 182 SMA weld-metal specimens as a function of growth rates for Ni-weld alloy in air. 44

45. Cyclic CGR data for Alloy 182 and Alloy 82 from the Davis-Besse CRDM nozzle J-groove weld and V.C. Summer reactor vessel nozzle-to-pipe weld. 45

46. Micrographs of the fracture surface of specimen WCR-01 and WLR-01. 46

Tables

1. Welding process and conditions for various weld passes. 4

2. Chemical composition (wt.%) of Alloy 182 weld metals. 4

3. Test conditions for various temperature and hydrogen tank overpressures. 12

4. Test conditions and crack growth data for specimen A182-1 of Alloy 182 SMA weld in PWR water. 23

5. Test conditions and crack growth data for specimen CT933H-1 of Alloy 182 SMA weld in PWR water. 27

6. Test conditions and crack growth data for specimen CT933H-2 of Alloy 182 SMA weld in PWR water. 29

Executive Summary

Ni-base alloys used as construction material in light water reactors (LWRs) have experienced stress corrosion cracking (SCC). Such cracking was first observed in steam generator tubes, but it has also occurred in Ni alloys used in applications such as instrument nozzles and heater thermal sleeves in the pressurizer and penetrations for control-rod drive mechanisms in the reactor-vessel closure heads. In operating plants, weld metals composed of Alloys 82 and 182 are used with Alloy 600. Less cracking has been observed in the weld materials than in the Alloy 600 wrought material. However, laboratory tests indicate that in PWR coolant environments, the SCC susceptibility of Alloy 182 may be greater than that of Alloy 600, while the susceptibility of Alloy 82 may be comparable to that of Alloy 600.

A program is being conducted at Argonne National Laboratory (ANL) to evaluate the resistance of Ni alloys and their welds to environmentally assisted cracking in simulated LWR coolant environments. The report summarizes the crack growth rate (CGR) results and related metallography for field and laboratory-prepared Alloy 600 and Ni-base alloy welds obtained in the program. This report also presents CGR results for Alloy 182 shielded-metal-arc welds in a simulated PWR environment as a function of temperature. These results were used to determine the activation energy for crack growth in Alloy 182 welds.

Metallographic examinations of the Ni–based alloy welds showed that the weld structure consists of vertically aligned columnar grains and dendrites. Orientation imaging microscopy (OIM), a diffraction-based technique, was used to determine the orientations of the grains and the type of grain boundaries present. The results show that a large proportion (70%) of the grain boundaries are random or high-angle boundaries, which are more susceptible to cracking than those in specific orientation relationships, also known as coincident site lattice boundaries. In addition, the OIM maps show the presence of clusters of grains that share similar orientations.

Tests used to determine the activation energy for SCC crack growth were performed in a simulated PWR environment at temperatures between 290°C and 350°C (554 - 662°F). The tests were performed by transitioning a fatigue crack into a stress corrosion crack in a specimen, and by measuring the changes in the stress corrosion CGR as the temperatures were varied during the test. The difference in electrochemical potential between the specimen and the Ni/NiO line was maintained constant at each temperature by adjusting the hydrogen overpressure on the water supply tank.

Activation energies for SCC crack growth in Alloy 182 SMA weld alloy were calculated from the results for SCC CGR as a function of temperature. Activation energies of 252 kJ/mol (59 kcal/mol) were obtained for the double-J weld material and 189 kJ/mol (33 kcal/mol) for the deep-groove weld material. These values are in agreement with the range of values reported in the literature. The data reported here and those in the literature suggest that the average activation energy for Alloy 182 welds is on the order of 220-230 kJ/mol, which is higher than the 130 kJ/mol (31 kcal/mol) commonly used for Alloy 600. The activation energy data for Alloy 82 are more limited. The average value from the literature data is ≈169 kJ/mol, which is somewhat higher than the value for Alloy 600. The consequences of using these larger values for the analysis of SCC CGR data were analyzed. The analysis showed that when an activation energy of 220 kJ/mol is used for calculation of the temperature-corrected CGRs for Alloy 182, the 75th percentile value of ln(α), which has been the value used for a disposition curve, becomes -27.54, yielding a value of 1.1×10^{-12} at 325°C (617°F) for the α parameter. This results in a disposition curve for Ni-alloy welds that is ≈36% lower than the curve based on data normalized with 130 kJ/mol; thus, the use of the 130 kJ/mol value leads to somewhat more conservative results.

In addition to the tests on laboratory prepared welds, CGR tests were performed on weldment samples from a Davis–Besse CRDM J-groove nozzle weld and from a V.C. Summer hot–leg nozzle to safe-end weld. For the Davis-Besse Alloy 182 weld specimens, the SCC CGRs under constant load are an order of magnitude lower than the disposition curve proposed for Alloy 182 weld metals. For the V.C. Summer weld specimens, the CGR data under constant load were lower than data obtained by others on the same alloys and lower than the proposed disposition curve. The data from the field welds correspond to values in the lower quartile of the distribution of crack growth rate data obtained on laboratory specimens. These results are not so statistically unlikely that they can be said to prove that there is a difference between field and laboratory welds, but such a difference would be consistent with the observations that operating experience indicates that PWSCC appears to occur more frequently in wrought Ni-base Alloy 600 components than in the weld metal Alloys 82 and 182 used with Alloy 600, despite the fact that in laboratory tests in PWR coolant environments, the stress corrosion cracking (SCC) susceptibility of Alloy 182 is usually found to be greater than that of Alloy 600, while that of Alloy 82 is comparable to that of Alloy 600.

Such a difference is also supported by the metallographic observations of extensive secondary cracking along the crack faces of specimens from field welds that is not observed in tests on laboratory welds. The reasons for these differences are unclear. The most obvious difference between field and laboratory welds is the degree of structural constraint imposed on the welds during the welding process, which is typically much greater for the field welds on actual components. However, metallographic studies on the welds away from the crack planes do not show hot cracks so that the secondary cracks seem to be part of the corrosion process. In any case, the use of the current database developed on laboratory welds would appear to be conservative.

The report also discusses the crack growth rate results for actual Alloy 600 component material and the environment enhancement of CGRs under cyclic loading. The SCC CGRs of the Alloy 600 nozzle from Davis-Besse are a factor of 4–8 higher than those of the median curve for Alloy 600. The growth rates correspond to the ≈95th percentile of the various data sets used in developing the median curve, i.e., the nozzle material exhibits very high susceptibility to SCC. The material exhibits predominantly IG fracture, even during precracking.

The environmental enhancement of CGRs under cyclic loading was determined relative to the CGRs that would be expected under the same loading conditions for Ni-weld alloys in air. The cyclic CGRs were analyzed by a superposition model to establish the individual contributions of mechanical fatigue, corrosion fatigue, and SCC.

Acknowledgments

The authors thank E. Listwan, T. Galvin, and R. Clark for their contributions to the experimental effort. The authors are also grateful to W. H. Cullen, Jr., for many helpful discussions. This work is sponsored by the Office of Nuclear Regulatory Research, U.S. Nuclear Regulatory Commission, under Job Code Y6388; Program Managers: S. Crane and H. J. Gonzalez.

This page is intentionally left blank.

Acronyms and Abbreviations

ANL	Argonne National Laboratory
ASTM	American Society for Testing and Materials
BWR	Boiling Water Reactor
C	Circumferential
CF	Corrosion Fatigue
CGR	Crack Growth Rate
CRDM	Control Rod Drive Mechanism
CSL	Coincident Site Lattice
CT	Compact Tension
DO	Dissolved Oxygen
ECP	Electrochemical Potential
EDX	Energy Dispersive X-ray
GBC	Grain Boundary Coverage
GBCD	Grain Boundary Character Distribution
GTA	Gas Tungsten Arc
HAB	High Angle Boundary
HAZ	Heat Affected Zone
IG	Intergranular
L	Longitudinal
LAB	Low Angle Boundary
LWR	Light Water Reactor
MA	Mill Annealed
NRC	Nuclear Regulatory Commission
NWC	Normal Water Chemistry
OIM	Orientation Imaging Microscopy
PWSCC	Primary Water Stress Corrosion Cracking
PWR	Pressurized Water Reactor
R	Radial
RTZ	Rolled Transition Zone
S	Side
SA	Solution Annealed
SCC	Stress Corrosion Cracking
SEM	Scanning Electron Microscopy
SHE	Standard Hydrogen Electrode
SMA	Shielded Metal Arc
SS	Stainless Steel

T	Transverse
TG	Transgranular
TT	Thermally Treated

1 Introduction

Nickel-base alloys used as construction material in pressurized water reactors (PWRs) have experienced primary water stress corrosion cracking (PWSCC). Such cracking has occurred in Alloy 600 and Alloy 182/82 components such as steam generator tubes, heater thermal sleeves and penetrations in the pressurizer, penetrations for the control rod drive mechanisms (CRDMs) in the reactor pressure vessel head, bottom-mounted instrumentation nozzles, and dissimilar metal welds between the low-alloy steel reactor vessel nozzle and stainless steel (SS) safe-end or pipe. Initiation of PWSCC involves a significant incubation period that depends primarily on temperature and material susceptibility. In general, cracking has occurred much earlier in the Alloy 600 base metal than in the Alloy 182 and Alloy 82 welds and at higher temperature locations within the reactor coolant system.[1] Also, small-bore pipes and tubes have cracked earlier than larger components.[1]

The PWSCC of Alloy 600 steam generator tubes in PWRs has been studied intensively.[2-4] In general, cracking occurs in regions of high residual stress due to cold work, such as the tube roll transition zone (RTZ), U-bends, tube denting locations, and plugs and sleeves.[5-7] The RTZ at the top of the tube sheet is the most common location for such cracking, and the cracks are most frequently axial, although circumferential cracks also occur. The PWSCC at U-bends has been associated with high residual stresses from the bending process. The PWSCC at dented tube support plates has also been related to the presence of stresses caused by the denting, and this problem has largely been resolved. Tube plugs, which typically have high residual stresses, are themselves prone to PWSCC. Heats of Alloy 600 show a wide variability in their susceptibility to PWSCC.[8-10] The use of improved thermal processing and a more resistant material, Alloy 690, has greatly reduced the incidence of this cracking in steam generator tubes.

The earliest location of PWSCC in components other than the steam generator tubes has been in the base metal of instrument nozzles and heater thermal sleeves in the pressurizer.[11] In these cases, the cracks were always axial and occurred at locations at the highest temperature and in materials with yield strength as low as ≈240 MPa (≈35 ksi), which is the minimum value allowed.

The other major locations of PWSCC of Alloy 600 components are at the nozzle penetrations for the CRDM in the reactor vessel closure heads.[12] In the fall of 1991, during an overpressurization test, a leak was discovered in the CRDM nozzle at the Bugey 3 plant in France. Metallurgical evaluations indicated that the leak was caused by PWSCC.[13] The main crack had initiated in Alloy 600 base metal and propagated into the Alloy 182 weld metal. Subsequent inspections of CRDM penetrations in the early 1990s in foreign PWRs indicated that ≈6.5% of the nozzles in French plants had axial cracks on the nozzle inner surface, while only ≈1.25% of the nozzles that were inspected in other plants had axial cracks. Inspection of the CRDM nozzles in seven plants in the United States (Point Beach 1, Oconee 2, Cook 2, Palisades, North Anna 1, Millstone 2, and Ginna) at this time suggested that the cracking was much less frequent than in the French plants. None of the cracks found in U.S. plants was through-wall, and until late 2000, no more leaks were found in pressure-vessel head penetrations.

In November 2000, leaks from axial through-wall cracks were identified at Oconee Unit 1, and in February 2001, at Arkansas Nuclear One Unit 1.[14] During the next 15 months, inspections at Oconee Units 2 and 3 and follow-up inspection at Unit 1 identified both axial and OD-initiated circumferential cracks in reactor vessel head penetrations.[15] The presence of circumferential cracks, in particular, raised concerns regarding structural integrity.[16,17] Also, in October 2000, significant boron deposits were discovered near the Loop "A" reactor vessel nozzle to the hot-leg reactor coolant pipe weld at the

V. C. Summer plant.[18] Ultrasonic inspection of the pipe revealed an axial crack and a short, intersecting circumferential crack at the top of the pipe in the dissimilar metal butt weld. The failed region was repaired with a new SS spool piece and Alloy 152 weld filler metal. Earlier in 2000, two shallow axial flaws were found in the outlet nozzle-to-safe-end weld of Ringhals Unit 3, and four axial indications were found in the same region of Ringhals Unit 4, in Sweden.[19] Cracks were also found in pressure-vessel head penetrations at North Anna Unit 2,[20] the Davis-Besse nuclear power plant,[21] and more recently, in the bottom-mounted instrumentation nozzles at South Texas Unit 1.[22,23]

Other instances of PWSCC in components fabricated from Ni alloys include cracking of the nozzle-coupling-to-vessel weld at the steam-generator lower head bowl drain, observed at Catawba Unit 2 in 2001,[24] and cracking in the heat-affected zone of an Alloy 600 safe end in a power-operated relief valve, near the connection to the pressurizer at the Palisades nuclear plant in 1993.[25]

In some incidents of PWSCC (e.g., cracking of the CRDM nozzle at the Davis-Besse plant),[21] leakage of the primary coolant resulted in significant degradation of ferritic steel components. At Davis-Besse, downstream of nozzle #3, a triangular cavity, about 127 mm (50 in.) wide and 178 mm (70 in.) long, had penetrated completely through the thickness of the low-alloy steel used for the reactor pressure-vessel head, leaving only a layer of SS cladding.

Plant operating experience indicates that PWSCC appears to occur more frequently in wrought Ni-base Alloy 600 components than in the weld metal Alloys 82 and 182 used with Alloy 600.[1] However, in laboratory tests in PWR coolant environments, the stress corrosion cracking (SCC) susceptibility of Alloy 182 is usually found to be greater than that of Alloy 600, while that of Alloy 82 is comparable to that of Alloy 600. This apparent inconsistency between field and laboratory experience is an issue that needs to be better understood.

This report summarizes the technical data obtained to date in the ANL study on Ni-alloy cracking in the PWR environment. New data are presented on CGRs in Alloy 182 welds in PWR environments at temperatures between 290°C and 350°C (554 - 662°F). As with the previous SCC tests conducted at ANL, precracking was carried out in the PWR environment and continued with loading cycles with increasing load ratios and increasing rise times prior to setting those samples at constant load to determine the SCC CGRs. This approach assured a complete SCC engagement and a uniform crack front. Each test was complemented by a detailed fractographic examination. The CGR data were analyzed to determine the activation energy for SCC growth rates in Alloy 182 welds in the PWR environment. The results from the present study and data available in the literature have been reviewed to determine the effects of material and environmental parameters on the cyclic and constant-load CGRs in these alloys. The alloys being investigated include laboratory-procured Alloys 600 and 690,[26-31] laboratory-prepared deep-groove and double-J welds of Alloy 182,[32] Alloy 600 from Davis-Besse CRDM nozzle #3, Alloy 182 from a J-groove weld in Davis-Besse nozzle #11, and Alloys 182 and 82 from a hot-leg nozzle-to-pipe weld in the V.C. Summer reactor coolant system.[33] The results have been compared with the existing CGR data to determine the relative susceptibility of these alloys to PWSCC and to determine whether the crack growth data in the field materials are consistent with our general understanding of CGRs in Ni-base alloys.

2 Experimental

2.1 Material and Specimen Design

All crack growth rate tests on Ni alloys and Ni-base welds were conducted in simulated PWR environments at temperatures of 290-350°C in accordance with American Society for Testing and Materials (ASTM) Designation E 647, "Standard Test Method for Measurement of Fatigue Crack Growth Rates," and ASTM E-1681, "Standard Test Method for Determining a Threshold Stress Intensity Factor for Environment-Assisted Cracking of Metallic Materials under Constant Load." The tests were performed on both 1-T and 1/2-T compact tension (CT) specimens; the configurations of the CT specimens are shown in Fig. 1.

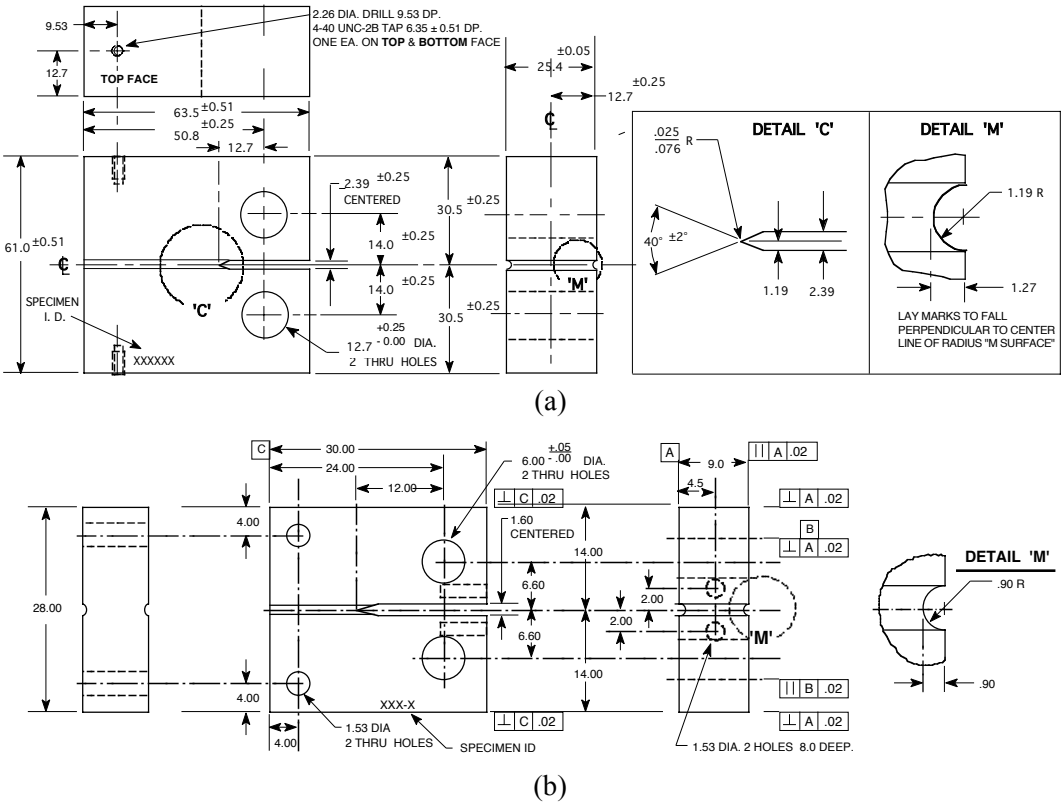

Figure 1. Configuration of the (a) 1-T and (b) 1/2-T CT specimens used for this study.

For the tests focused on determining the activation energy for SCC crack growth in Alloy 182 weld, one 1-T CT specimen (A182-1) was machined from a laboratory-prepared double-J weld (Fig. 2a), and two 1/2-T specimens (CT933H-1 and CT933H-2) were machined from a deep-groove filled weld (Fig. 2b). The welds were prepared following ASME Boiler and Pressure Vessel Code, Section IX. The double-J weld was produced by joining two Alloy 600 plates and was prepared by 48 weld passes. Root passes 1 to 5 involved gas tungsten arc (GTA) welding with Alloy 82 filler/electrode, and the other passes, shielded-metal-arc (SMA) welding with Alloy 182 filler. A schematic of the weld design and various passes is shown in Fig. 2a. The conditions for each weld pass are listed in Table 1. During welding, the maximum inter-pass temperature was ≈120°C (250°F), and the weld surfaces were cleaned by wire brushing and grinding and were rinsed with de-mineralized water or alcohol. The deep-groove filled weld was prepared by using a 51-mm (2.0 in.) thick Alloy 600 plate with a deep groove that was

filled by several passes of SMA welding with Alloy 182 filler/electrode that was either 1/8 or 5/32 in. in size (Fig. 2b). The chemical compositions of the weld metals are given in Table 2.

Table 1. Welding process and conditions for various weld passes.

Weld Pass	Process	Filler Metal	Filler/Electrode Size (in.)	Current (A)	Voltage (V)	Travel Speed (in./min)
1 - 5	GTA	Alloy 82	3/32	185 - 215	21 - 22	2 - 4
6 - 10	SMA	Alloy 182	3/32	140 - 155	24 - 26	6 - 7
11 -27	SMA	Alloy 182	1/8	155 - 170	25 - 27	6 - 7
28 - 48	SMA	Alloy 182	5/32	170 - 180	26 - 28	6 - 7

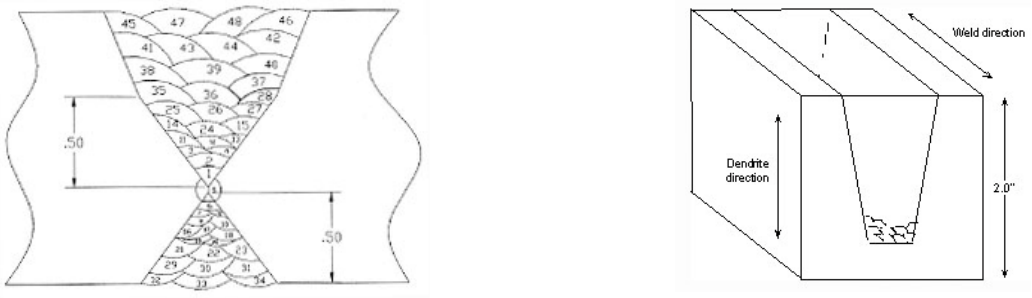

(a) (b)

Figure 2. Schematic of the weld joint design and weld passes for (a) Alloy 182 SMA double-J weld and (b) the deep-groove weld (dimensions are in inches).

Table 2. Chemical composition (wt.%) of Alloy 182 weld metals.

Alloy ID (Heat)	Analysis	C	Mn	Fe	S	P	Si	Cu	Ni	Cr	Ti	Nb	Co
A 182	Spec.	0.10*	5.0-9.5	6.0-10.0	0.015*	–	1.0*	0.5*	Bal	13.0-17.0	1.0*	1.0-2.5	0.12*
A 182 Double-J	ANL	0.0415	7.095	6.005	0.008	0.06	0.53	0.03	65	14.35	0.43	1.585	0.03
A 182 Deep Groove	ANL	0.04	7.08	6.82	0.005	0.025	0.35	0.03	70.44	13.81	0.30	1.06	0.02

*Maximum.

Specimen A182-1 was cut from a double-J Alloy 182 SMA weld in the TS orientation,* as shown schematically in Fig. 3a. The two 1/2-T CT specimens, both in the TS orientation, were cut from the deep-groove Alloy 182 weld (Fig. 3b). In order to accommodate the 1-T CT dimensions, Alloy 600 plate was EB-welded as shown schematically in the figures.

(a) (b)

Figure 3. Orientation of the CT specimens from (a) the Alloy 182 SMA double-J weld and (b) the deep-groove weld.

*The first letter represents the direction normal to the fracture plane and the second represents the direction of crack advance. As shown in Fig. 3, the three directions are: T = transverse, L = longitudinal, and S = side.

2.2 Test Facilities

The CGR tests in simulated primary water environments were conducted in the following test facilities. Specimen A182-1 was tested in a 6-liter SS autoclave configured for 1-T CT specimens. One 1/2-T CT specimen, CT933H-1, was tested in a 1-liter SS autoclave, while the companion 1/2-T CT specimen, CT933H-2, was tested in a 2-liter SS autoclave. This section provides a description of these testing facilities.

2.2.1 Facility with 6-Liter Autoclave

The 6-liter autoclave facility is typically used for CGR tests at temperatures not exceeding 320°C (608°F). The facility consists of a closed-loop electro-hydraulic material test system equipped with an extended column load frame rated at 89 kN (20,000 lb) maximum. The 5.7-liter Type 316 SS autoclave has a 175-mm (6.875-in.) outside diameter and is rated for a working pressure of 5050 psig (35 MPa) at 343°C (650°F). The load frame is accessorized with an Instron Model 8800 control console, and a hydraulic pump. The autoclave is connected to a recirculating water system. The test facility also consists of a temperature control unit, a DC potential control console, a DC potential measurement unit, and a data acquisition and recording system. The autoclave, mounted within the load-frame, has been modified to permit a ≈19-mm (0.75-in.) dia shaft to load the test specimen through a "Bal-Seal" gland in the top of the autoclave cover. Up to three 1-T or 1/2-T CT specimens can be tested in series inside the autoclave.

The test facility is designed for easy access to the specimens during assembly of the test train. The actuator assembly, consisting of the hydraulic actuator, load cell, autoclave plug, and the internal specimen load train, may be raised and lowered hydraulically to position the specimens at a convenient height. A photograph of the specimen load train is shown in Fig. 4. A CT specimen may be substituted for any or all of the three central in-line blocks.

The autoclave is continuously supplied with simulated primary water solution from a feedwater tank. Figure 5 shows a schematic diagram of the water system. The water system consists of a feedwater storage tank, high-pressure pump, regenerative heat exchanger, autoclave preheater, test autoclave, electrochemical potential (ECP) cell, regenerative heat exchanger, back-pressure regulator, and return line to the feedwater tank. The storage tank has a hydrogen cover gas to maintain a desired dissolved hydrogen concentration in the water. In the once-through mode, the return line is connected to the drain. Water is circulated at relatively low flow rates (15-25 mL/min).

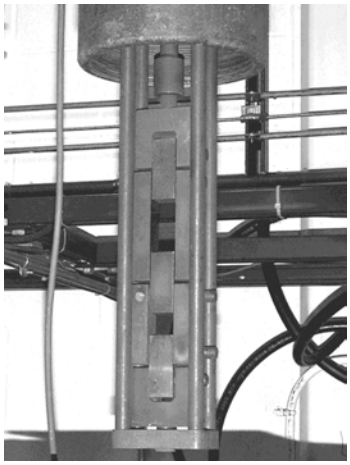

Figure 4.
Photograph of the specimen load train.

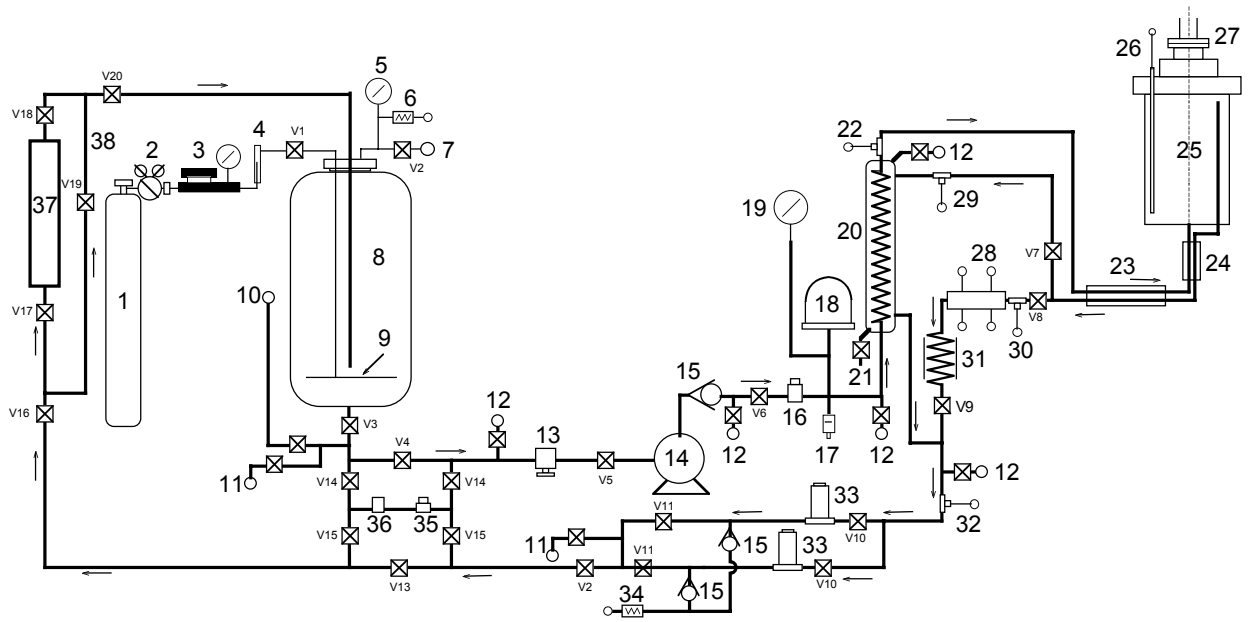

1. COVER GASS SUPPLY TANK	20. HEAT EXCHANGER (HX)
2. TWO-STAGE HIGH-PRESSURE REGULATOR	21. DRAIN
3. LOW-PRESSURE REGULATOR	22. HX FEEDWATER OUTLET TC
4. FLOW METER	23. AUTOCLAVE & ECP CELL PREHEATER
5. COMPOUND VACUUM & PRESSURE GAUGE	24. HEAT EXCHANGER
6. PRESSURE RELIEF VALVE	25. COMMERCIAL AUTOCLAVE
7. VENT TO AIR & FLASH ARRESTOR	26. THERMOWELL
8. FEEDWATER STORAGE TANK	27. “BAL SEAL” RETAINER
9. SPARGE TUBE	28. ECP CELL
10. FEEDWATER FILL PORT	29. HX EFFLUENT INLET TC
11. WATER SAMPLE PORT	30. ECP CELL INLET TC
12. SYSTEM BLEED PORT	31. AIR-COOLED COIL
13. SOLENOID VALVE	32. BPR INLET TC
14. HIGH-PRESSURE PUMP	33. BACK-PRESSURE REGULATOR (BPR)
15. CHECK VALVE	34. PRESSURE RELIEF VALVE
16. PRESSURE TRANSDUCER	35. CONDUCTIVITY METER
17. RUPTURE DISC	36. PH METER
18. ACCUMULATOR	37. ION EXCHANGE BED
19. HIGH-PRESSURE GAUGE	38. ION EXCHANGE BED BYPASS LINE

Figure 5. Schematic diagram of the recirculating 6-liter autoclave system.

2.2.2 Facility with 1-Liter Autoclave

The 1-liter autoclave facility is a modified version of an in-cell facility for conducting CGR tests on irradiated materials and is capable of test temperatures up to 310°C (590°F). The actuator assembly consisting of a hydraulic actuator, a 22-kN (5-kip) load cell, an autoclave cover plate, an internal specimen load train, and a furnace that is mounted on top of a portable wheeled cart that can be easily relocated. A 1-liter SS autoclave is installed inside the furnace for conducting tests in simulated PWR environments. The furnace and the autoclave body are mounted on a pneumatic cylinder and can be raised to enclose the internal specimen load train and the specimen during the test. Water is circulated through a port in the autoclave cover plate that serves both as inlet and outlet.

The 1/2-T CT specimen is mounted in the clevises with Zircaloy pins (Fig. 6). The two sets of clevises are at 90º opposition, forming a pair of universal joints. The specimen and clevises are kept electrically insulated from the load train by using oxidized Zircaloy pins and mica washers to connect the clevises to the rest of the load train. The crack length is monitored by reversing-current DC potential drop measurements. Platinum wires are used for the current and potential leads. The current leads are attached to SS split pins that are inserted into the holes at the top and bottom of the specimen. The potential leads are attached by screwing short SS pins into threaded holes in the specimen and attaching the platinum wires with in-line SS crimps. This system does not operate with a reference bar for correcting the DC potential. An Instron Model 8500+ Dynamic Materials Testing System is used to load the specimen.

Figure 6.
Photograph of the specimen load train for the 1-liter autoclave.

A schematic diagram of the recirculating water system is shown in Fig. 7. The recirculating water system consists of a storage tank, high pressure pump, an accumulator, regenerative heat exchanger, autoclave preheater, autoclave, ECP cell preheater, ECP cell, air-cooled coil, water-cooled chill block, Mity Mite^{TM} back-pressure regulator, and return line to the storage tank. In the recirculating mode, the ECP cell is bypassed, and water from the autoclave is returned to the storage tank through the regenerative heat exchanger, water-cooled chill block, and back-pressure regulator. With the ECP cell in use, to avoid any possible contamination of chlorides from the reference electrode, the system is operated only in the once-through mode; water from the autoclave is circulated through the ECP cell preheater, ECP cell, air-cooled coil, water-cooled chill block, back-pressure regulator, and drain to the sump. Water is circulated at flow rates of 45-160 mL/min.

The feedwater storage tank, manufactured by Filpaco Industries, has 130-L capacity and is constructed of stainless steel. The tank is designed for vacuum and overpressure to 414 kPa (60 psig). The storage tank has a hydrogen cover gas to maintain a desired dissolved hydrogen concentration in the water.

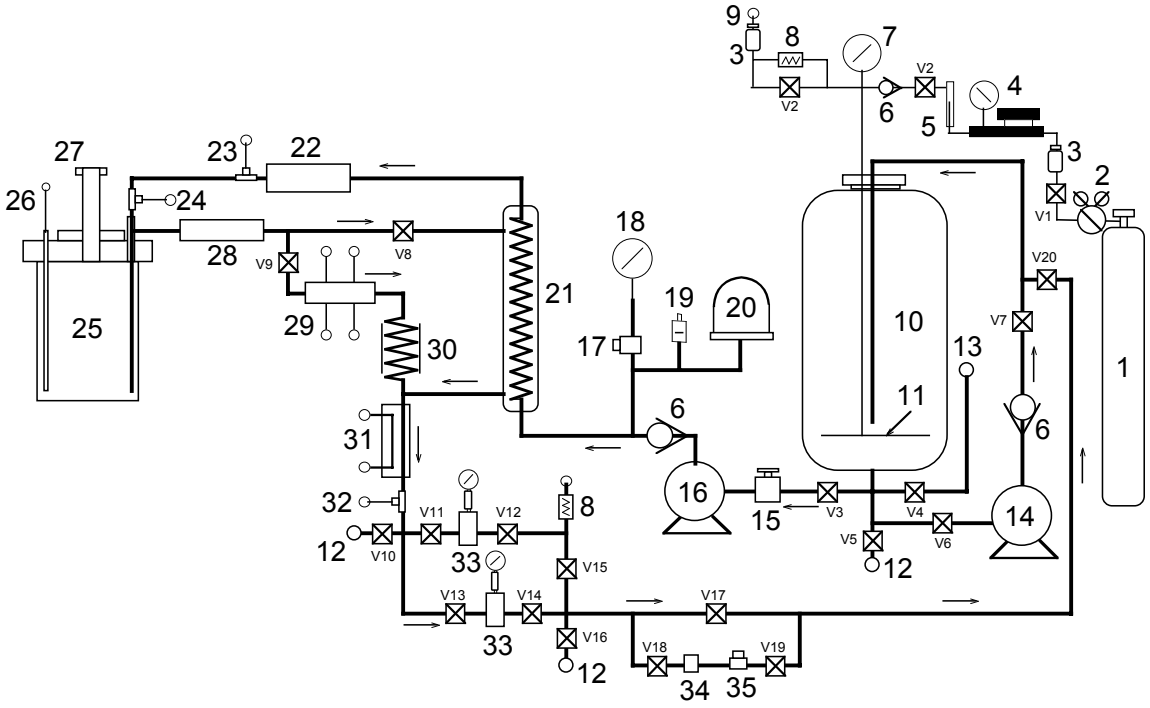

1. COVER GASS SUPPLY TANK	19. RUPTURE DISC
2. TWO-STAGE HIGH-PRESSURE REGULATOR	20. ACCUMULATOR
3. FLASH ARRESTOR	21. HEAT EXCHANGER (HX)
4. LOW-PRESSURE REGULATOR	22. AUTOCLAVE PREHEATER
5. FLOW METER	23. PREHEATER OUTLET TC
6. CHECK VALVE	24. AUTOCLAVE INLET TC
7. COMPOUND VACUUM & PRESSURE GAUGE	25. COMMERCIAL AUTOCLAVE
8. PRESSURE RELIEF VALVE	26. THERMOWELL
9. VENT TO AIR & FLASH ARRESTOR	27. “BAL SEAL” RETAINER
10. FEEDWATER STORAGE TANK	28. ECP CELL PREHEATER
11. SPARGE TUBE	29. ECP CELL
12. WATER SAMPLE PORT	30. AIR-COOLED COIL
13. FEEDWATER FILL PORT	31. WATER COOLED HEAT EXCHANGER
14. FEEDWATER TANK RECIRCULATION PUMP	32. BPR INLET TC
15. SOLENOID VALVE	33. BACK-PRESSURE REGULATOR (BPR)
16. HIGH-PRESSURE PUMP	34. PH METER
17. PRESSURE TRANSDUCER	35. CONDUCTIVITY METER
18. HIGH-PRESSURE GAUGE	

Figure 7. Schematic diagram of the recirculating 1-liter autoclave system.

2.2.3 Facility with a 2-Liter Autoclave

The 2-liter autoclave test facility was built by Cortest Inc. and allows test temperatures of up to 350°C (662°F). The servohydraulic test frame consists of a load cell, load train, autoclave, and furnace. The hydraulic actuator is mounted on bottom of the test frame, with the test train components suspended above it. The load cell is located at the bottom of the pull rod. An Instron Model 8800 control console is used to load the specimen. A 2-liter autoclave is installed inside the furnace for conducting tests in simulated LWR environments. The heater bands are mounted on the autoclave vessel. Figure 8 is a photograph showing the entire test system.

Figure 8. Layout of the 2-liter autoclave system.

The load cage that contains the test specimen consists of the cover plate of the autoclave and a thick bottom plate separated by four compression rods (Fig. 9). The lower two-piece clevis assembly is fastened to the bottom plate of the cage, and the upper piece is connected to the pull rod. A 1/2T CT or dog-bone tensile specimen can be mounted between the clevises. The specimen and clevises are kept electrically insulated from the load train by using oxidized Zircaloy pins and mica washers to connect the clevises to the rest of the load train. The crack length is monitored by the same method as for the previous two facilities. Water is circulated through a port in the autoclave body, which serves both as inlet and outlet. A schematic diagram of the recirculating water system is shown in Fig. 10.

Figure 9.
Photograph of the specimen load train for the 2-liter autoclave.

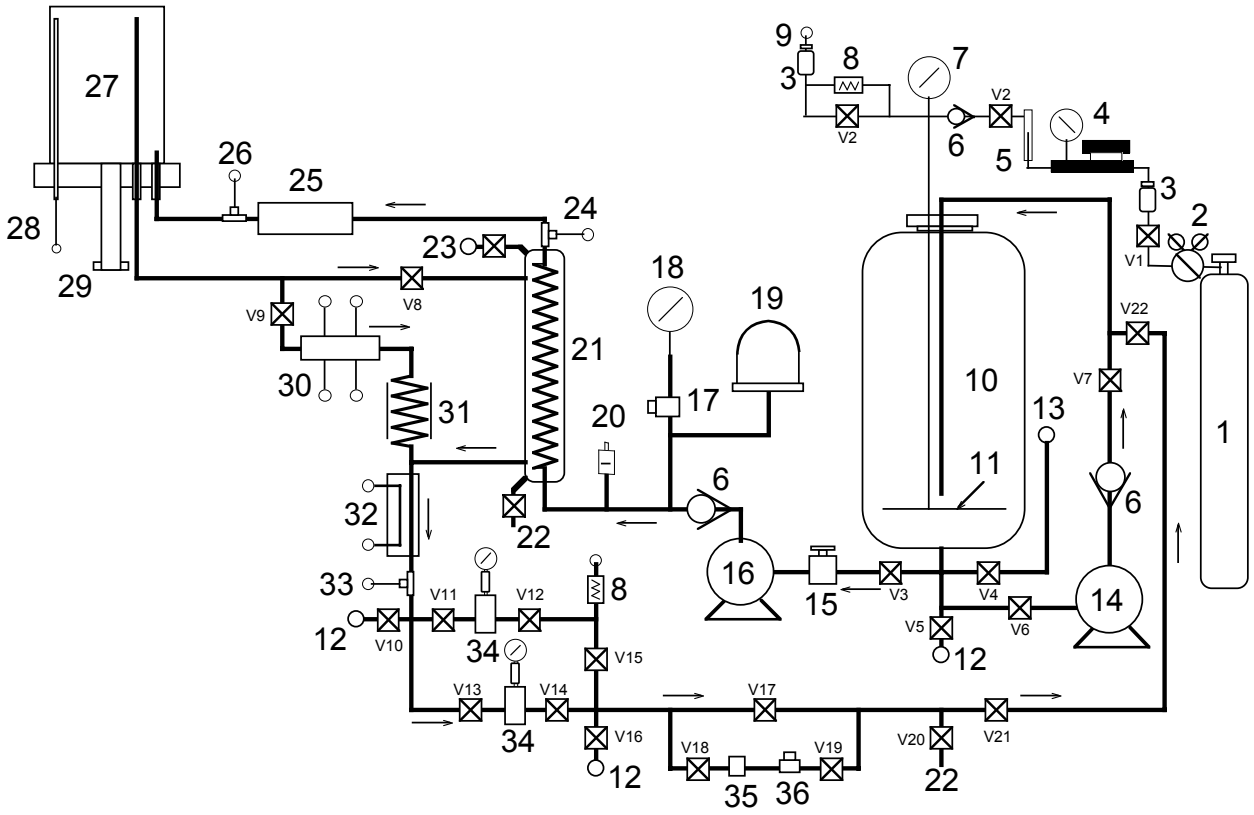

1. COVER GASS SUPPLY TANK
2. TWO-STAGE HIGH-PRESSURE REGULATOR
3. FLASH ARRESTOR
4. LOW-PRESSURE REGULATOR
5. FLOW METER
6. CHECK VALVE
7. COMPOUND VACUUM & PRESSURE GAUGE
8. PRESSURE RELIEF VALVE
9. VENT TO AIR & FLASH ARRESTOR
10. FEEDWATER STORAGE TANK
11. SPARGE TUBE
12. WATER SAMPLE PORT
13. FEEDWATER FILL PORT
14. FEEDWATER TANK RECIRCULATION PUMP
15. SOLENOID VALVE
16. HIGH-PRESSURE PUMP
17. PRESSURE TRANSDUCER
18. HIGH-PRESSURE GAUGE
19. ACCUMULATOR
20. RUPTURE DISC
21. HEAT EXCHANGER (HX)
22. DRAIN
23. SYSTEM BLEED PORT
24. HEAT EXCHANGER OUTLET TC
25. AUTOCLAVE PREHEATER
26. PREHEATER OUTLET TC
27. COMMERCIAL AUTOCLAVE
28. THERMOWELL
29. "BAL SEAL" RETAINER
30. ECP CELL
31. AIR-COOLED COIL
32. WATER COOLED HEAT EXCHANGER
33. BPR INLET TC
34. BACK-PRESSURE REGULATOR (BPR)
35. PH METER
36. CONDUCTIVITY METER

Figure 10. Schematic diagram of the recirculating 2-liter autoclave system.

2.2.4 Primary Water Environment

The simulated PWR feedwater contains 2 ppm Li as LiOH, 1000 ppm B as HBO_3, ≈2 ppm dissolved hydrogen (≈23 cm^3/kg), and less than 10 ppb dissolved oxygen (DO). It is prepared from the laboratory supply of deionized water by first passing this water through a local filtration system that

includes a carbon filter, an Organex-Q filter, two ion exchangers, and a 0.2-mm capsule filter. The DO in the deionized water is reduced to <10 ppb by bubbling/sparging pure H_2 through the water. To speed deoxygenation of a fresh tank of water, a vacuum may be applied to the feedwater tank at the vent port. The PWR water is prepared by dissolving boric acid and lithium hydroxide in 20 L of deionized water before adding the solution to the supply tank. The dissolved hydrogen in the water is calculated from the supply tank hydrogen pressure and temperature.

Water samples are taken periodically to measure pH, resistivity, and DO concentration both upstream and downstream from the autoclave. An Orbisphere meter and CHEMetrics™ ampoules are used to measure the DO concentrations in the supply and effluent water. The redox and open-circuit corrosion potentials are monitored at the autoclave outlet by measuring the ECPs of platinum and an Alloy 600 electrode, respectively, against a 0.1 M KCl/AgCl/Ag external (cold) reference electrode. The measured ECPs, $E_{(meas)}$ (mV), were converted to the standard hydrogen electrode (SHE) scale, $E_{(SHE)}$ (mV), by the polynomial expression[34]

$$E_{(meas)} + 286.637 - 1.0032 \cdot (\Delta T) + 1.7447 \times 10^{-4} \cdot (\Delta T)^2 - 3.03004 \times 10^{-6} \cdot (\Delta T)^3, \quad (1)$$

where ΔT(°C) is the temperature difference of the salt bridge in a 0.1 M KCl/AgCl/Ag external reference electrode (i.e., the test temperature minus ambient temperature).

The effect of the proximity of the corrosion potential for the SCC test to the potential at the Ni/NiO phase transition on crack growth rates is well-established. While the mechanistic origin is unclear, there are consistent data showing that CGRs of Ni-base alloys peak near the Ni/NiO phase boundary.[35-37] Thus, to isolate the effect of temperature, the tests are conducted so that the difference between the corrosion potential of the specimen and that of the Ni/NiO phase transition was maintained approximately constant. The Ni/NiO phase transition is very close to the H_2/H_2O phase transition, and the latter controls the corrosion potential of the simulated primary water environment. As such, the corrosion potential difference reduces to the difference of two hydrogen electrodes:[37]

$$\Delta E = E_{test} - E_{Ni/NiO} = -\frac{RT}{2F} \ln\left(\frac{[H_2]_{test}}{[H_2]_{Ni/NiO}}\right) \quad (2)$$

where:
- E_{test} = potential at test temperature T
- $E_{Ni/NiO}$ = potential of the Ni/NiO transition at test temperature T
- R = universal gas constant
  = 8.314 x 10^{-3} kJ/mol K (1.103 x 10^{-3} kcal/mol°R)
- F = Faraday constant
  = 96485 C/mol
- $[H_2]_{test}$ = hydrogen concentration at test conditions
- $[H_2]_{Ni/NiO}$ = hydrogen concentration at the Ni/NiO transition

For two tests, conducted at temperatures T_1 and T_2 and satisfying the constant corrosion potential difference to the Ni/NiO line, Eq. 2 transforms into the following relationship between hydrogen concentrations and test temperatures:

$$\frac{RT_2}{2F} \ln\left(\frac{[H_2]_{test2}}{[H_2]_{Ni/NiO-test2}}\right) = \frac{RT_1}{2F} \ln\left(\frac{[H_2]_{test1}}{[H_2]_{Ni/NiO-test1}}\right) \quad (3)$$

where: $[H_2]_{test2}$ = hydrogen concentration at test temperature T_2
$[H_2]_{test1}$ = hydrogen concentration at test temperature T_1
$[H_2]_{Ni/NiO\text{-}test2}$ = hydrogen concentration at Ni/NiO transition for test 2
$[H_2]_{Ni/NiO\text{-}test1}$ = hydrogen concentration at Ni/NiO transition for test 1

The hydrogen concentration at the Ni/NiO transition as a function of temperature was determined by fitting the data by Attanasio et al.[36] with a fourth-order polynomial (Fig. 11). The best fit was found to be given by the following expression:

$$[H_2]_{Ni/NiO}(T) = -8783.1+53.803\cdot T- 0.11961\cdot T^2+ 0.00011238\cdot T^3- 3.628899\times10^{-8}\cdot T^4 \quad (4)$$

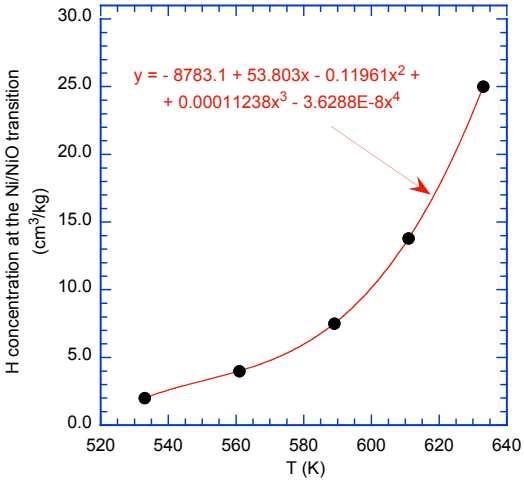

Figure 11.
Hydrogen concentration at Ni/NiO phase transition as a function of temperature (data taken from Ref. 36).

Equation 3 can be solved for the hydrogen concentration at test temperature T_2. This concentration maintains the potential difference to the Ni/NiO line similar to that of a test conducted at temperature T_1. For the purpose of this calculation, test conditions "1" are considered those typical of tests conducted in a PWR environment at 320°C (T_1 = 593 K, $[H_2]_{test1}$ = 23 cm^3/kg). The results for several temperatures of interest are shown in Table 3. For each temperature, the hydrogen concentration at the Ni/NiO transition is calculated by Eq. 4, and then the concentration needed to maintain the corrosion potential difference constant is calculated by Eq. 3.

Table 3. Test conditions for various temperature and hydrogen tank overpressures.

Test Temperature		$[H_2]_{Ni/NiO}$	$[H_2]_{test}$	ΔE
(°C)	(K)	(cm^3/kg)	(cm^3/kg)	(mV)
290	563	3.0	11.01	31.5
300	573	3.9	13.81	31.3
305	578	4.5	15.60	31.1
310	583	5.2	17.71	30.8
320	593	7.1	23.00	30.1
350	623	17.8	47.59	26.4

2.3 Test Procedure

The CGR tests were conducted in the load-control mode using a triangular, sawtooth, or trapezoidal waveform with load ratio R of 0.3-0.7. The CT specimens were fatigue precracked with a triangular waveform in the test environment at load ratio R = 0.3, frequency ≈1 Hz, and maximum stress intensity factor K_{max} of 20-25 MPa $m^{1/2}$ (18.2-22.8 ksi $in^{1/2}$). After ≈0.5-mm (20 mils) extension, R was increased incrementally to 0.5-0.7, and the loading waveform changed to a slow/fast sawtooth with rise times of 30-1000 s, and unload time of 12 s This loading sequence is considered to result in reproducible CGRs.[38] For sawtooth loading, the CGRs were calculated on the basis of the rise time. During individual test periods, K_{max} was maintained approximately constant by periodic load shedding (less than 2% decrease in load at any given time).

Crack extensions were monitored by the reversing-DC potential difference method. The current leads were attached to the holes on the top and bottom surfaces of the specimen (Fig. 1), and potential leads were either welded on the front face of the specimen across the machined notch but on diagonal ends (1T-CT specimens, Fig. 1a) or attached to pre-machined taps (1/2T-CT specimens, Fig. 1b). Also, to compensate for the effects of changes in resistivity of the material with time, an Alloy 182 internal reference bar was installed near the test specimen. The CT specimen and reference bar were connected in series, and the DC potential across the specimen as well as the reference bar was monitored continuously during the test. The results for the reference bar were used to normalize potential drop measurements for the CT test specimen.

During crack growth tests in high-temperature water, environmental enhancement of CGRs does not occur from the start of the test. Under more rapid cyclic loading, the crack growth is dominated by mechanical fatigue. The CGRs during precracking and initial periods of cyclic loading were primarily due to mechanical fatigue. In general, environmental enhancement is typically observed under loading conditions that would lead to CGRs between 10^{-10} and 10^{-9} m/s in air.

The stress intensity factor range ΔK was calculated in accordance with ASTM E 1681 and E 647 as follows:

$$\Delta K = \frac{\Delta P}{\left(B B_N W\right)^{1/2}} \frac{\left(2+\frac{a}{W}\right)}{\left(1-\frac{a}{W}\right)^{3/2}} f\left(\frac{a}{W}\right) \tag{5}$$

$$\Delta P = P_{max} - P_{min} \qquad \text{for } R > 0 \tag{6}$$

$$f\left(\frac{a}{W}\right) = 0.886 + 4.64\left(\frac{a}{W}\right) - 13.32\left(\frac{a}{W}\right)^2 + 14.72\left(\frac{a}{W}\right)^3 - 5.6\left(\frac{a}{W}\right)^4, \tag{7}$$

where P_{max} and P_{min} are maximum and minimum applied load, a is crack length, W is the specimen width, and effective thickness $B_{eff} = (B\ B_N)^{0.5}$. The applied K and crack size limits for the tests met the ASTM E 1681 and E 647 criteria. These criteria are intended to ensure applicability and transferability of the cracking behavior of a component or specimen of a given thickness under a specific loading condition to a crack associated with a different geometry, thickness, and loading condition. The K/size criteria

require that the plastic zone at the tip of a crack is small relative to the specimen geometry. For constant load tests, ASTM E 1681 requires that

$$B_{eff} \text{ and } (W - a) \geq 2.5\ (K/\sigma_{ys})^2, \tag{8}$$

and for cyclic loading ASTM 647 requires that

$$(W - a) \geq (4/\pi)\ (K/\sigma_{ys})^2, \tag{9}$$

where K is the applied stress intensity factor, and σ_{ys} is the yield stress of the material. In high-temperature water, because the primary mechanism for crack growth during continuous cycling is not mechanical fatigue, Eq. 8 is probably the more appropriate criterion, but Eq. 9 may give acceptable results. For high-strain hardening materials (i.e., ultimate-to-yield stress ratio $\sigma_{ult}/\sigma_{ys} \geq 1.3$), both criteria allow the use of the flow stress defined as $\sigma_f = (\sigma_{ult} + \sigma_{ys})/2$ rather than the yield stress.

In an earlier report,[33] experimental CGR data were obtained at ANL on field Alloy 600 and weld Alloys 82 and 182. In that report, K values were calculated using the correlations for a disc-shaped specimen instead of a standard CT specimen. The earlier data have been corrected using Eqs. 5-7; the corrected data are given in Appendix A of this report. The difference between the K values based on the correlations for a disc-shaped specimen and standard CT specimen is <5%.

After the test the specimen was fractured in liquid nitrogen, and the fracture surfaces were examined by optical or electron microscopy to measure the final crack length using the 9/8 averaging technique; that is, the two near-surface measurements were averaged, and the resultant value was averaged with the remaining seven measurements.

2.4 Analysis of Crack Growth Rate Data

Under cyclic loading, the CGR (m/s) can be expressed as the superposition of the rate in air (i.e., mechanical fatigue) and the rates due to corrosion fatigue and SCC ($\dot{a}_{CF}$ and $\dot{a}_{SCC}$, respectively), given as

$$\dot{a}_{env} = \dot{a}_{air} + \dot{a}_{CF} + \dot{a}_{SCC}\,. \tag{10}$$

The cyclic CGRs for Ni alloys and welds in air were determined from the correlations developed earlier at ANL:[31,33]

$$\dot{a}_{air} = \left(\frac{da}{dN}\right)/t_r = \left[C \cdot (1 - 0.82 \cdot R)^{-2.2} \cdot (\Delta K)^{4.1}\right]/t_r\,, \tag{11}$$

where da/dN is the growth rate per cycle, t_r is the rise time for the loading cycle, R is the load ratio (i.e., ratio of the minimum and maximum stress intensity factors K_{min}/K_{max}), ΔK is K_{max} - K_{min} in MPa $m^{1/2}$, and the constant C depends on the material and temperature. For Alloy 600 the constant (C_{A600}) is a third-order polynomial with respect to temperature T (°C),

$$C_{A600} = 4.835\times10^{-14} - (1.622\times10^{-17})T + (1.490\times10^{-18})T^2 - (4.355\times10^{-21})T^3\ . \tag{12}$$

For Ni-alloy welds, the constant (C_{Niweld}) is given by a fourth-order polynomial with respect to temperature T (°C), expressed as

$$C_{Ni\text{-}weld} = 8.659\times10^{-14} - (5.272\times10^{-17})T + (2.129\times10^{-18})T^2 - (1.965\times10^{-20})T^3 + (6.038\times10^{-23})T^4 \quad (13)$$

In LWR coolant environments, the CGRs of Alloy 600 show frequency-dependent enhancement under cyclic loading conditions. In high-DO water [i.e., normal water chemistry (NWC) boiling water reactor (BWR) water], the environmental enhancement of the growth rates does not appear to depend on the material composition (e.g., C content) or material heat treatment. In contrast, environmental enhancement of CGRs of Alloy 600 in low-DO water does seem to be strongly dependent on material conditions. In the literature,[39-43] such variability has been attributed to thermomechanically controlled parameters, such as yield strength and grain boundary coverage of carbides, although the evidence for this dependence is more substantial for steam generator tubing than for structural components.

In earlier ANL work, correlations were developed to estimate the enhancement of cyclic CGRs in LWR environments relative to the CGRs in air under the same loading conditions. In the absence of any significant contribution of SCC to growth rate, the cyclic CGRs for Alloy 600, either in the solution annealed (SA) condition or the SA plus thermally treated condition, in ≈300 ppb DO water at 289°C is given by the expression[28]

$$\dot{a}_{env,A600} = \dot{a}_{air,A600} + 4.4\times10^{-7}\cdot\left(\dot{a}_{air,A600}\right)^{0.33}. \quad (14)$$

In low-DO environments (e.g., hydrogen water chemistry BWR or PWR environment) at 320°C (608°F), some alloys show little enhancement, while others show enhancement comparable to that predicted by Eq. 14.

Similarly, correlations describing the cyclic CGRs of Ni-alloy welds (e.g., Alloys 182 and 82) have been developed.[33] Under similar loading conditions, the CGRs of Ni-alloy welds are a factor of 2-3 higher than those of Alloy 600. The analysis[33] indicated that the cyclic CGRs of Ni-alloy welds in PWR water may either be bounded by $5 \times CGR_{air}$ or be represented by the expression

$$\dot{a}_{env,Ni-weld} = \dot{a}_{air,Ni-weld} + 0.018\cdot\left(\dot{a}_{air,Ni-weld}\right)^{0.78}. \quad (15)$$

The SCC growth rate data for Alloy 600 and its weld metals have been reviewed by White and Hickling[44,45] to determine the effects of critical parameters such as stress intensity factor, temperature, material heat treatment, cold work, and water chemistry on growth rates. For Alloy 600, the CGR (m/s) under SCC conditions is represented by the expression,[44]

$$\dot{a}_{A600} = \alpha\exp\left[-\frac{Q}{R}\left(\frac{1}{T}-\frac{1}{T_{ref}}\right)\right](K-K_{th})^{\beta}, \quad (16)$$

where: Q = activation energy for crack growth,
= 130 kJ/mol (31.1 kcal/mol) for Alloy 600,
R = universal gas constant,
= 8.314×10^{-3} kJ/mol K (1.103×10^{-3} kcal/mol°R),

T = absolute operating temperature in K (or °R),
T_{ref} = absolute reference temperature used to normalize the CGR data,
= 598 K (1076.67°R),
α = crack growth amplitude (2.67×10^{-12} at 325°C),
K = crack tip stress intensity factor (MPa $m^{1/2}$),
K_{th} = crack tip stress intensity factor threshold (9 MPa $m^{1/2}$), and
β = exponent 1.16.

The effect of K on the SCC growth rate for Ni-alloy welds in PWR environments has been represented by a modified[45] version of the above relationship. Unlike the CGR relationship for Alloy 600, the relationship for Ni-alloy welds has no threshold value for the stress intensity factor K,

$$\dot{a}_{Ni-weld} = \alpha \exp\left[-\frac{Q}{R}\left(\frac{1}{T} - \frac{1}{T_{ref}}\right)\right] K^{\beta}, \quad (17)$$

where Q, R, T, and T_{ref} are the same as in Eq. 16; crack growth amplitude α is 1.5×10^{-12} at 325°C; and exponent β is 1.6. Also, unlike Alloy 600 for which a reliable value for the activation energy for crack growth has been determined, no such number is available for the Ni-weld alloys. Thus, for Ni-weld alloys, the activation energy is assumed to be the same as that for Alloy 600.

3 Microstructural Characterization

The alloys used in the present project have been subject to an extensive metallograpic analysis. The results were presented in detail in previous reports.[32,33] This section summarizes the most important findings for laboratory-prepared alloys and for field components from the Davis-Besse and V. C. Summer reactors.

3.1 Laboratory-Prepared Alloys

A metallographic examination was performed to characterize the microstructure of the laboratory-prepared welds by scanning electron microscopy (SEM), energy dispersive X-ray (EDX) spectroscopy, and OIM. For this purpose, three rectangular pieces (1 cm × 2 cm × 0.5 cm) were cut from the double-J weld. All samples were mechanically polished through 1-μm diamond paste, followed by electrolytic etching for 10-20 s in a 70% H_3PO_4 and water solution at 5 V at room temperature to reveal the dendritic structure and carbides.

Scanning electron microscopy revealed a microstructure with elongated grains and dendritic features typical of weld alloys (Fig. 12). A large variation in grain size between the different weld passes was also observed. In addition, high angle boundaries were observed to extend from the weld into the weld heat-affected zone (HAZ). The implication of this observation is that once a crack initiates in the HAZ, it can then readily extend into the weld or vice-versa via such continuous, cracking-susceptible boundaries.

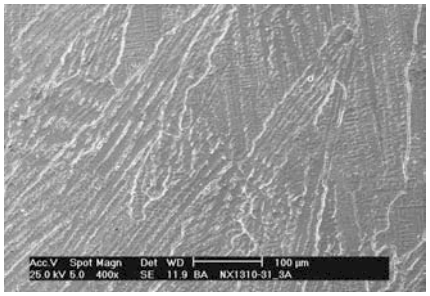

Figure 12.
Dendritic microstructure on a laboratory-preapred Alloy 182 weld specimen.

Both matrix and grain boundary precipitates were also investigated. Figure 13a shows an example of one such matrix precipitate, and Fig. 13b shows the EDX spectra resulting from the matrix and the precipitate. The comparison of the two spectra indicates that the Ti and O peaks are higher in the spectrum resulting from the precipitate, suggesting that the particle composition is TiO_2.

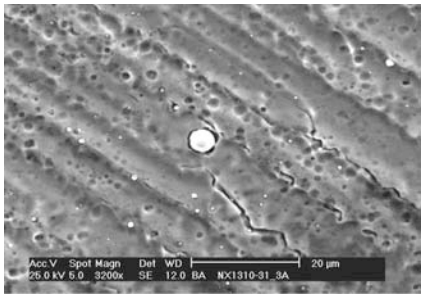

(a)

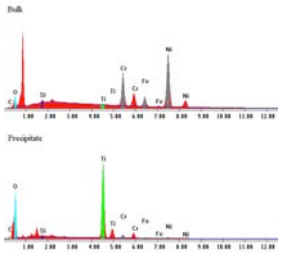

(b)

Figure 13. (a) Micrograph showing one of the matrix precipitates observed on the surface of sample 3A and (b) EDX spectra resulting from the bulk and the precipitate shown in (a).

The deep-groove weld was also examined by OIM to determine primarily the grain-boundary character distribution and to check for any texture in the microstructure. Both these parameters are known to influence the SCC behavior of austenitic alloys in high-temperature water environments.[46-52] The OIM analysis allows a classification of boundaries according to the coincident site lattice model as either coincident site lattice boundaries (CSLBs) or high-angle boundaries (HABs). The CSLBs are formed when the neighboring grains are in specific orientation relationships and have been shown to possess an increased resistance to SCC over HABs.[46-52] In addition, texture affects the high-temperature deformation behavior of a polycrystalline material and thus is expected to play a role in the SCC behavior as well.

The OIM maps obtained from a plane parallel to the direction of dendrites are shown in Figs. 14a and b. The microstructure consists of columnar grains, typical of those observed on this plane. Grains with similar orientations tend to cluster (the different orientations are shown with different colors). The boundary character distributions resulting from the two scans (Figs. 14b and d) show CSL fractions of 27.5% and 22.7%, much lower numbers than those typically found for solution-annealed Alloy 600.

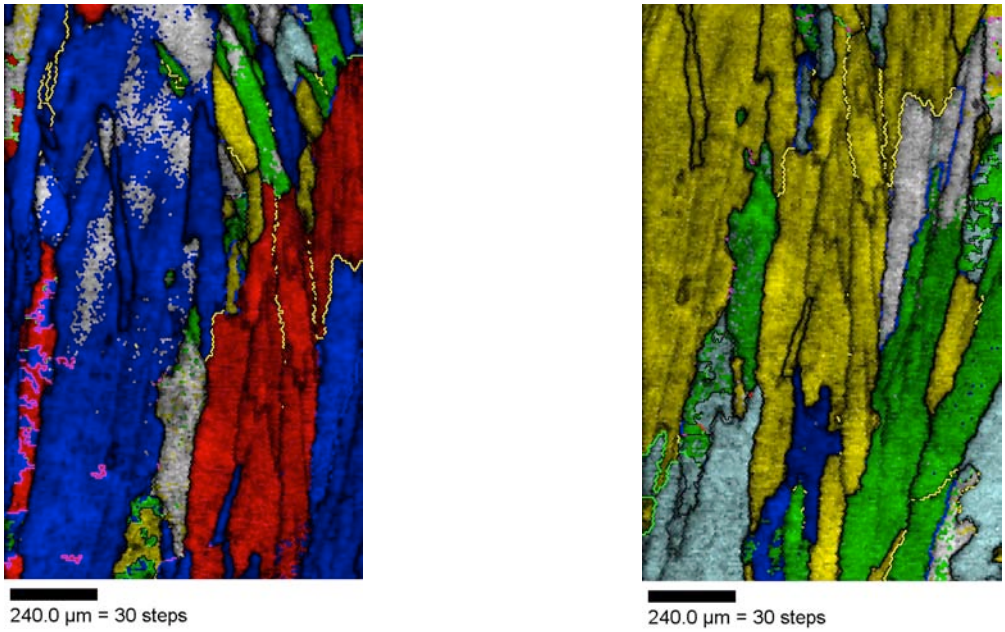

(a) (b)

Figure 14. OIM maps from a plane parallel to the direction of dendrites showing the grain orientations (a, c).

Figure 15 shows the grain-boundary character distribution (GBCD) of the weld alloys. This distribution is dominated by low-angle boundaries (LABs, Σ1*) and is consistent with the clustering of grains of similar orientations. The higher the proportion of neighboring grains that share some particular orientation, the higher becomes the probability that these grains have parallel crystal structures. The fact that the GBCD is dominated by Σ1 boundaries also makes the weld metal significantly different from Alloy 600, in which the GBCD is dominated by twin-related Σ3, Σ9, and Σ27 boundaries (of which approximately half are coherent).[52]

*In the CSL model the Σ number is the reciprocal of the density of coincident sites.

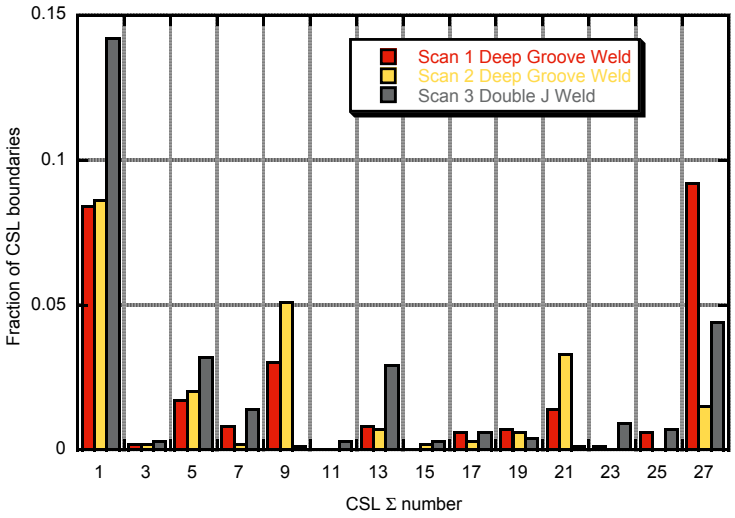

Figure 15.
Grain boundary character distribution for laboratory-prepared welds.

The OIM analysis presented in this section shows that the intragranular dendrites are coherent and are, therefore, expected to be resistant to cracking. In consequence, it appears that the grain boundary character distribution (along with residual deformation) will determine the cracking behavior of the welds. The proportion of cracking-resistant CSL boundaries in the weld was found to be relatively small; however, the grains having similar orientations were observed to cluster.

3.2 Field Alloys

Microstructural characterization of material from the Alloy 600 nozzle and J-groove weld from Davis-Besse was conducted on the planes of interest for crack formation and growth in cylindrical-tensile and CT specimens.[33] The specimens were mechanically polished with 1-µm diamond paste. The Alloy 600 specimens were etched with Marble's reagent (hydrochloric acid, copper sulfate, and distilled water). The weld specimens were electrochemically etched in a 5% nital solution at 5 V at room temperature to show grain boundaries, followed by etching in 70% phosphoric acid solution at 5 V at room temperature to show the interdendritic microstructure.

Figure 16 shows the microstructure observed on the Alloy 600 nozzle specimens. The grain size varies significantly, ranging from 30 to 200 µm, with an average size of ≈75 µm (ASTM grain size 4). Microhardness measurements indicated that the hardness was uniform across the nozzle wall. There was extensive grain boundary coverage (GBC) by Cr-rich carbides, and a few carbides were randomly distributed in the matrix. Although in most cases the boundaries were decorated with carbides, in some cases the carbides appeared to be present only on one side of the boundary (e.g., the boundary going from top left to bottom right in Fig. 16b). The average size of the grain-boundary carbides was ≈0.3 µm, and the GBC was estimated to be in the range 50-60%. The specimens were also examined by EDX spectroscopy to investigate the precipitates in the matrix and along the grain boundaries. The large precipitates in the grain matrix and boundaries were Ti-rich. The effect of Ti-rich precipitates on the SCC behavior is unknown. The precipitation of Ti carbides can reduce the concentration of free carbon retained in the matrix to a level which limits the precipitation of the desirable grain-boundary chromium carbides. If Ti carbides precipitate at grain boundaries, they may oxidize when exposed to the high temperature water environment, possibly leading to grain boundary embrittlement. However, crack tip examinations by TEM have found no evidence of Ti oxides,[53] suggesting that these particles do not participate directly in the SCC process.

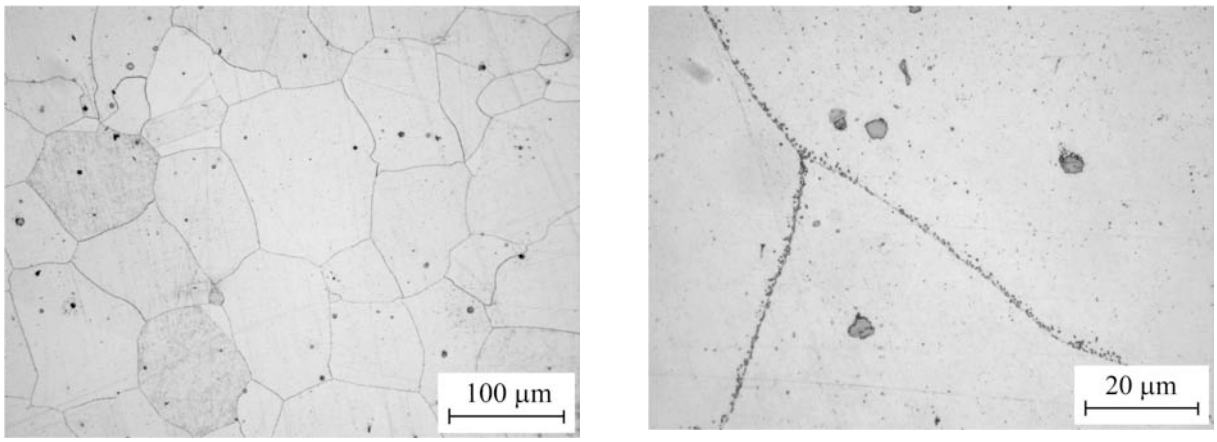

(a) (b)

Figure 16. Microstructures observed on planes (a) 03-1 and (b) 03-2 of the CRDM nozzle alloy.

Figure 17 shows the microstructures observed on the specimens cut from the Davis-Besse Alloy 182 J-groove weld. These micrographs show the interdendritic microstructure typical of welds and are consistent with the microstructure expected based the plane of observation.

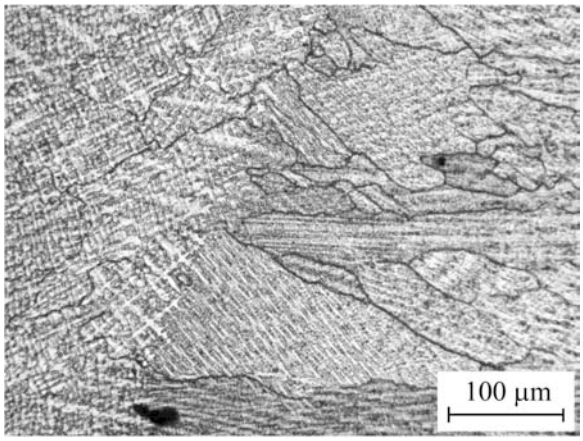

Figure 17.
Microstructure observed on the Alloy 182 J-groove weld specimen from Davis-Besse.

As with the material from Davis-Besse, the metallography for the weld alloys from the V. C. Summer power plant was also focused on the planes of interest for crack formation and growth in the cylindrical-tensile and CT specimens. Both the Alloy 182 butter and the Alloy 82 weld were examined. The samples were mechanically polished with 1-µm diamond paste, and electrochemically etched in a 70% phosphoric acid solution at 5 V.

Figure 18 shows a micrograph of the Alloy 182 butter microstructure. The micrograph shows interdendritic microstructure consistent with the plane of observation: the elongated grains (and dendrites) are oriented primarily in a horizontal direction.

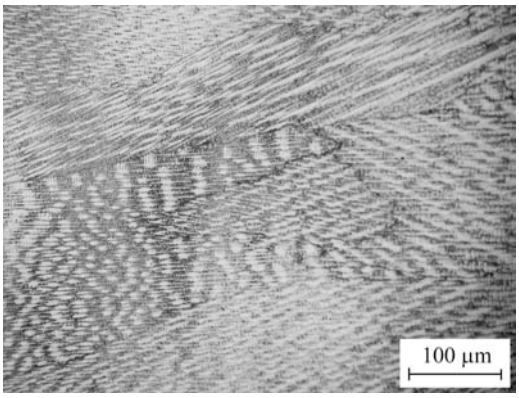

Figure 18.
Microstructure of the butter Alloy 182.

Figure 19 shows the microstructure of the Alloy 82 weld. This typical weld microstructure consists of dendrites (and columnar grains) oriented primarily in the vertical direction in the micrograph.

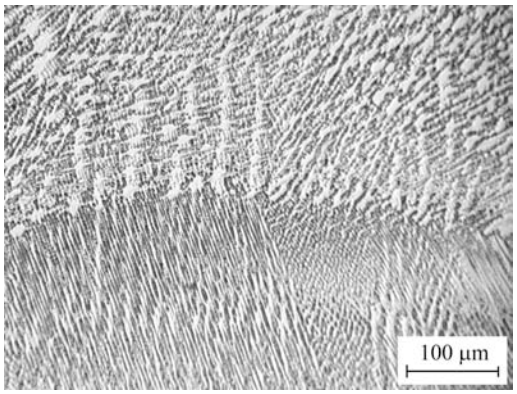

Figure 19.
Microstructure of the weld Alloy 82 from the V.C. Summer plant.

Of possible significance to the SCC behavior of this weld was the observation of grain boundary sliding at the interface between the Alloy 82 weld metal and the SS pipe. Several examples are indicated with white arrows in Fig. 20. Sliding occurred exclusively at grain boundaries (most likely high angle) extending from the pipe material to the weld material. Most likely, the grain boundary sliding occurred during the repair of this weld due to high residual stresses and local heating. Because grain boundary sliding is a precursor to intergranular SCC initiation,[54] these observations suggest that the interface may be quite susceptible to SCC. Nevertheless, the picture shown in Fig. 20 was taken from a location away from where the samples for SCC testing were cut; thus, the observed sliding is unlikely to have any bearing on the SCC results presented in this report.

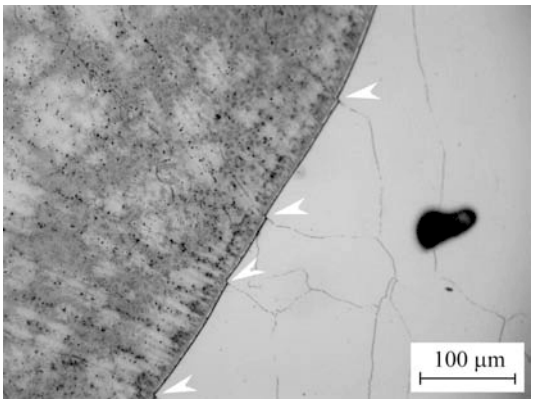

Figure 20.
Grain boundary sliding at the weld-pipe interface.

This page is intentionally left blank.

4 Crack Growth Test Results

This section focuses on the crack growth data obtained from the three Alloy 182 specimens described in Section 2.1. The objective of these tests was to determine the activation energy in Alloy 182 weld. The first specimen (A182-1) was a 1-T CT specimen cut from a laboratory-prepared double-J weld, while the other two (CT933H-1 and CT933H-2) were companion 1/2-T CT specimens machined from a laboratory-prepared deep-groove weld.

4.1 Double-J Weld Specimen A182-1

This test was conducted with the A182-1 specimen in the temperature range 290-320°C (554-608°F). The test was started at 320°C. After a steady-state CGR was obtained at 320°C, the temperature was reduced to 305°C and then to 290°C.

The specimen was fatigue precracked at K_{max} = 20 MPa $m^{1/2}$ (18.2 ksi $in^{1/2}$) R = 0.3, and a triangular waveform, and then cycled with a sawtooth waveform at R = 0.5 with increasing rise times up to 1000 s. The specimen was next set to constant load. After approximately 600 h and 0.270 mm (10 mils) of growth, the temperature was lowered to 305°C. The hydrogen gas concentration was lowered from 23 to 15 cc/kg by adjusting the hydrogen gas overpressure on the water supply tank. After approximately 1300 h and 0.1 mm (4 mils) of growth, the temperature was lowered to 290°C, and the hydrogen concentration was lowered to 11 cc/kg. After another approximately 1200 h and 0.06 mm (2.3 mils) of growth, the temperature was increased back to 320°C. The hydrogen concentration was also increased to 23 cc/kg.

The entire fracture surface of specimen A182-1 is shown in Fig. 21. Figure 21a shows the optical image, while Fig. 21b shows the SEM image. Both images show a relatively uniform crack surface, with an intergranular fracture mode in the second half of the test run. The fracture surface images were used for correcting the DC potential data. The correction factors were 1.29 for the transgranular region and 2.6 for the intergranular region. The resulting cyclic and constant load data obtained on this specimen are summarized in Table 4, and the changes in crack length and K_{max} with time are shown in Fig. 22.

Table 4. Test conditions and crack growth data for specimen A182-1 of Alloy 182 SMA weld in PWR water.[a]

Test Period	Test Time (h)	Temp. (°C)	H Conc. (cc/kg)	O_2 Conc.[b] (ppb)	Load Ratio R	Rise Time (s)	Down Time (s)	K_{max} (MPa $m^{1/2}$)	ΔK (MPa $m^{1/2}$)	CGR_{env} (m/s)	Estimated CGR_{air} (m/s)	Crack Length (mm)
Pre a	103	321.8	23	<10	0.30	0.5	0.5	20.8	14.5	1.48E-07	6.05E-08	12.820
Pre b	126	321.3	23	<10	0.30	5	5	22.4	15.6	3.54E-08	8.15E-09	14.253
Pre c	142	321.2	23	<10	0.30	100	100	22.4	15.7	3.93E-09	4.14E-10	14.354
Pre d	148	321.8	23	<10	0.3	5	5	23.2	16.3	4.60E-08	9.54E-09	15.027
Pre e	166	321.6	23	<10	0.3	100	100	23.3	16.3	3.95E-09	4.79E-10	15.073
Pre f	173	322.2	23	<10	0.3	5	5	24.1	16.9	5.37E-08	1.11E-08	15.828
Pre g	266	321.1	23	<10	0.3	100	100	25.2	17.6	4.24E-09	6.64E-10	16.574
1	365	321.8	23	<10	0.5	300	12	29.0	14.5	2.59E-09	1.71E-10	17.571
2	599	320.9	23	<10	0.5	600	12	30.7	15.3	1.43E-09	1.07E-10	18.772
3	867	320.8	23	<10	0.5	1000	12	32.1	16.0	1.04E-09	7.79E-11	19.705
4	1464	322.1	23	<10	1.0	-	-	33.7	0.0	5.88E-10	-	20.696
5	2776	307.3	15	<10	1.0	-	-	34.5	0.0	1.23E-10	-	21.196
6	3,982	291.1	11	<10	1.0	-	-	35.2	0.0	3.63E-11	-	21.552
7	4,819	321.4	23	<10	1.0	-	-	37.8	0.0	4.95E-10	-	23.057

[a]Simulated PWR water with 2 ppm Li, 1100 ppm B, and 2 ppm. Conductivity was 21 ± 3 µS/cm, and pH was 6.4.
[b]Represents values in the effluent.

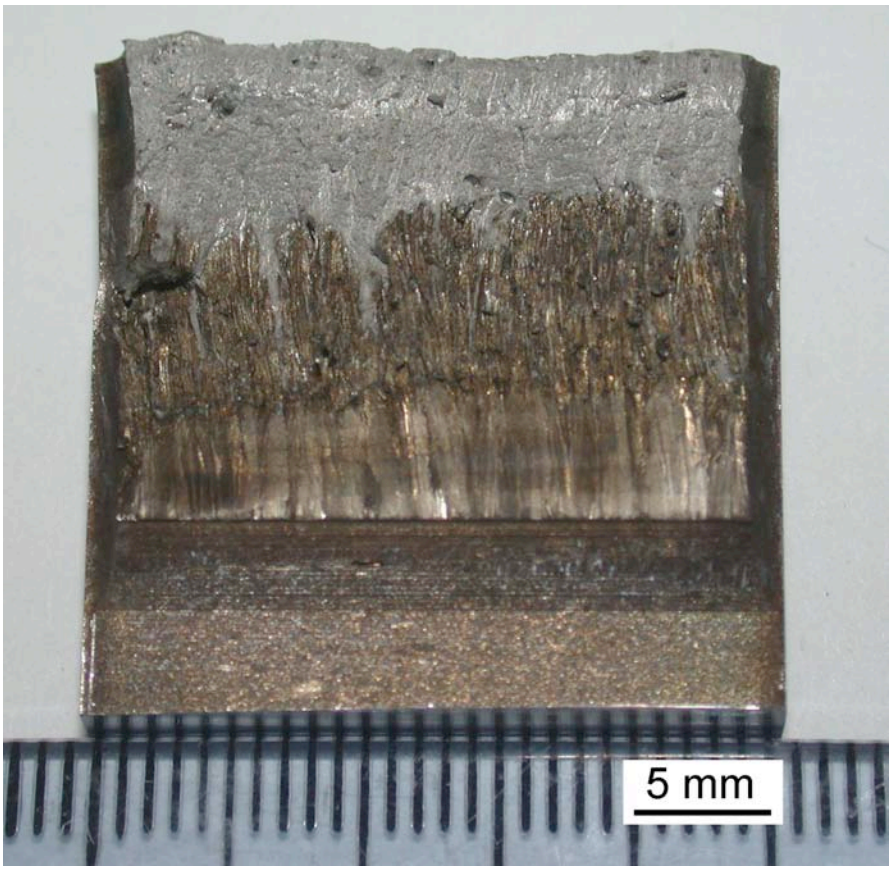

(a)

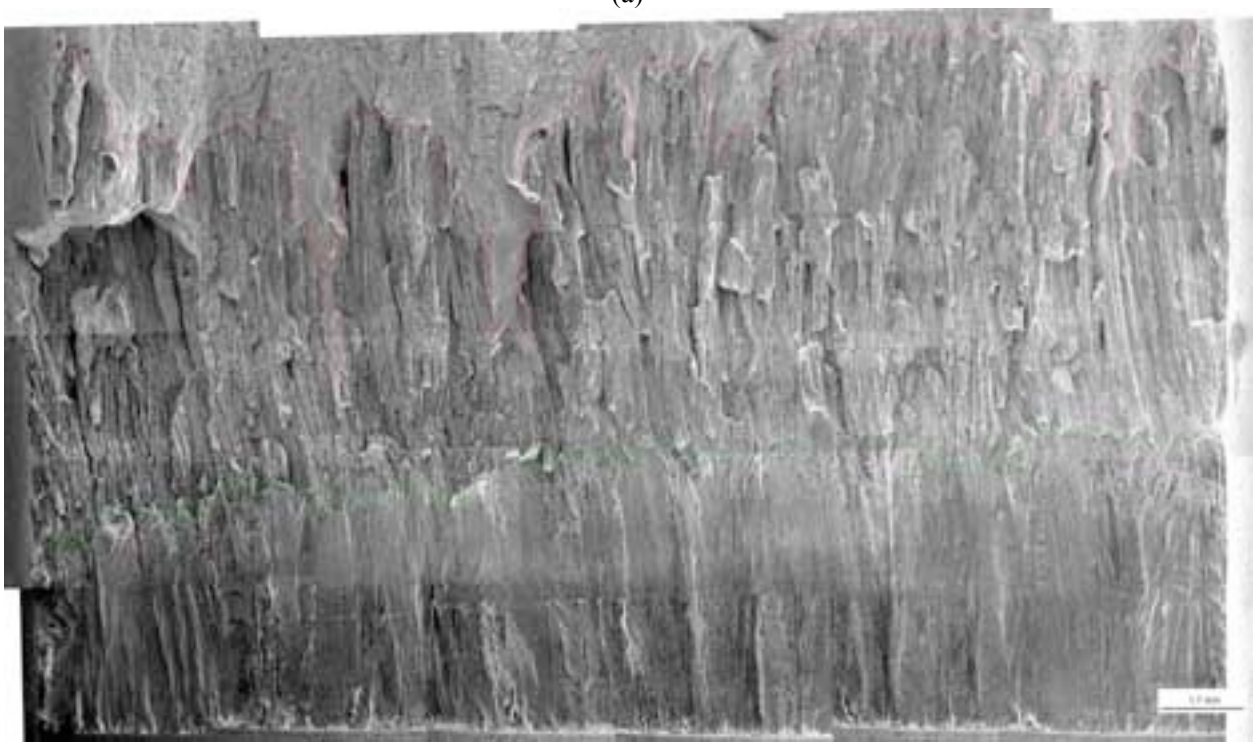

(b)

Figure 21. Fracture surface of specimen A182-1: (a) optical image and (b) SEM image.

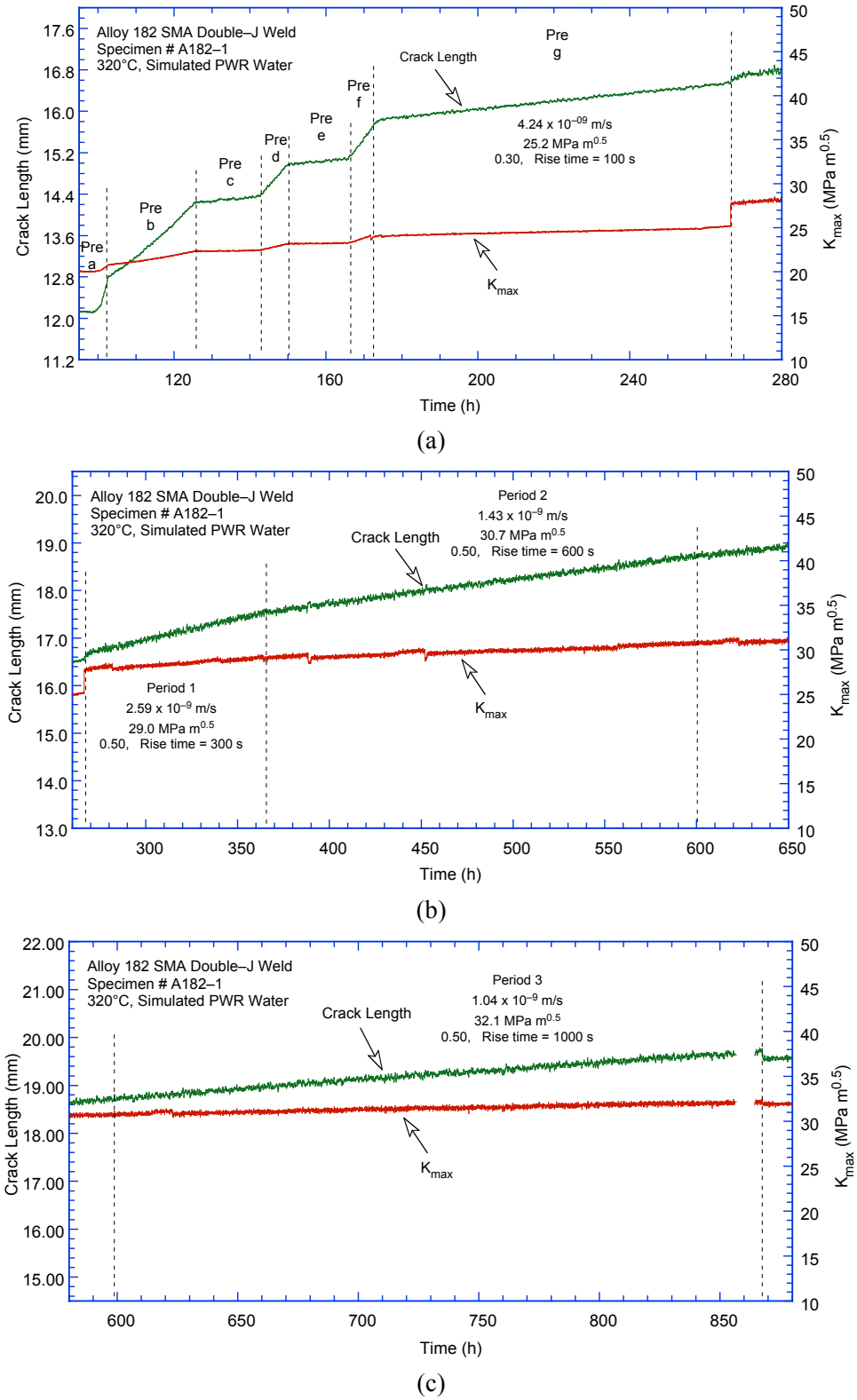

Figure 22. Crack length vs. time for Alloy 182 weld specimen A182-1 in simulated PWR environment during test periods (a) precracking, (b) 1-2, (c) 3, and (d) 4-7.

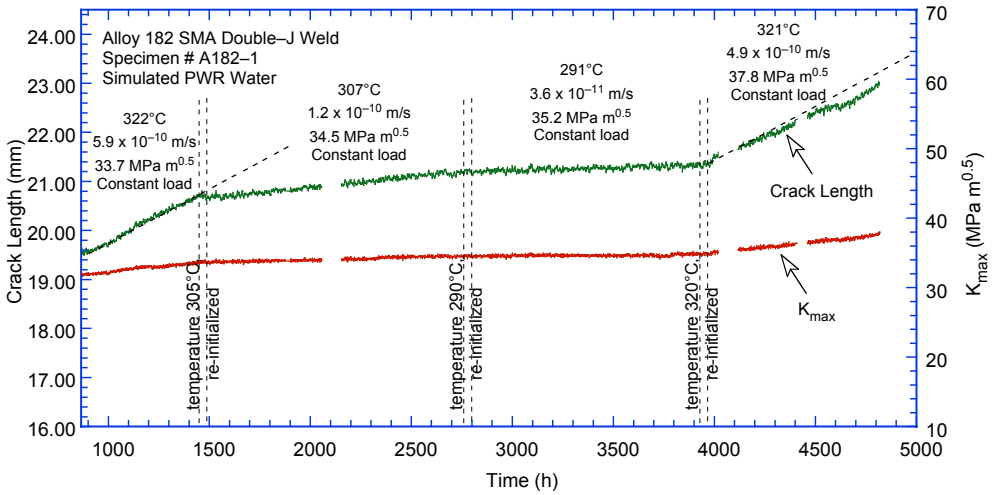

(d)

Figure 22. (Cont.)

4.2 Deep-Groove Weld Specimen CT933H-1

This test was conducted with the CT933H-1 specimen in the temperature range 290-310°C (554-590°F). The test was started at 310°C. After a steady-state CGR was obtained at 310°C, the temperature was reduced to 300°C and then to 290°C. At the end of the test, the temperature was increased back to 310°C.

The CT933H-1 specimen was fatigue precracked in the environment at 310°C with K_{max} = 20 MPa $m^{1/2}$ (18.2 ksi $in^{1/2}$), R = 0.3, and a triangular waveform, and then cycled with a sawtooth waveform at R = 0.5 with increasing rise times up to 500 s. The specimen was then set at constant load. After approximately 1900 h, the temperature was decreased to 300°C, and the supply tank hydrogen concentration was lowered from 18 to 14 cc/kg by adjusting the hydrogen gas overpressure on the water supply tank. After another 1600 h the temperature was further decreased to 290°C, and the water hydrogen concentration was lowered to 11 cc/kg. After approximately 700 h at 290°C the temperature was increased back to 310°C (hydrogen concentration 18 cc/kg) for the final period.

The entire fracture surface of the CT933H-1 specimen is shown in Fig. 23. This picture was used for data correction. The correction factors were 1.15 for the transgranular region and 4.3 for the intergranular region. The testing conditions are shown in Table 5, and the changes in crack length and K_{max} with time are shown in Fig. 24.

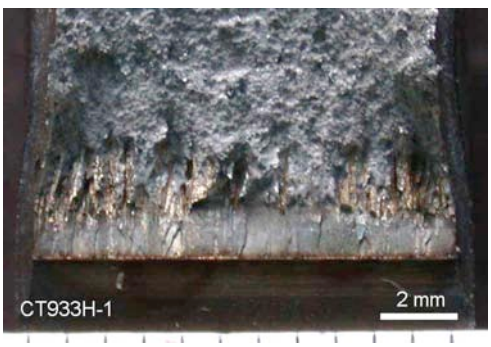

Figure 23.
Fracture surface of Alloy 182 weld specimen CT933H-1 tested in simulated PWR environment at temperatures of 290-310°C (554-590°F).

Table 5. Test conditions and crack growth data for specimen CT933H-1 of Alloy 182 SMA weld in PWR water.[a]

Test Period	Test Time (h)	Temp. (°C)	H Conc. (cc/kg)	O_2 Conc.[b] (ppb)	Load Ratio R	Rise Time (s)	Down Time (s)	K_{max} (MPa $m^{1/2}$)	ΔK (MPa $m^{1/2}$)	CGR_{env} (m/s)	Estimated CGR_{air} (m/s)	Crack Length (mm)
Pre a	51	310.8	18	<10	0.29	1.00	1.00	19.6	13.9	2.60E-08	2.22E-08	12.404
Pre b	66	311.1	18	<10	0.30	10	10.0	12.3	8.6	1.49E-09	3.20E-10	12.412
Pre c	69	311.1	18	<10	0.32	1.0	1.0	18.2	12.4	2.36E-08	1.47E-08	12.581
1	96	311.3	18	<10	0.16	50.0	12.0	18.7	15.7	1.85E-09	5.51E-10	12.636
2	146	310.5	18	<10	0.15	500.0	12.0	23.6	20.1	5.21E-10	1.45E-10	12.720
3	718	310.4	18	<10	0.50	500.0	12.0	24.8	12.4	1.27E-10	4.84E-11	13.084
4	2685	310.2	18	<10	1.00	0.0	-	26.0	0.0	5.88E-11	-	13.418
5	4294	301.2	14	<10	1.00	0.0	-	26.7	0.0	1.25E-11	-	13.493
6	4,968	292.1	11	<10	1.00	0.0	-	26.8	0.0	2.68E-11	-	13.541
7	6,870	310.7	18	<10	1.00	0.0	-	27.1	0.0	3.62E-11	-	13.689
8	6,958	310.7	18	<10	0.50	500.0	12.0	27.2	13.6	1.30E-10	7.02E-11	13.773

[a]Simulated PWR water with 2 ppm Li, 1100 ppm B, and 2 ppm. Conductivity was 21 ± 3 µS/cm, and pH was 6.4.
[b]Represents values in the effluent.

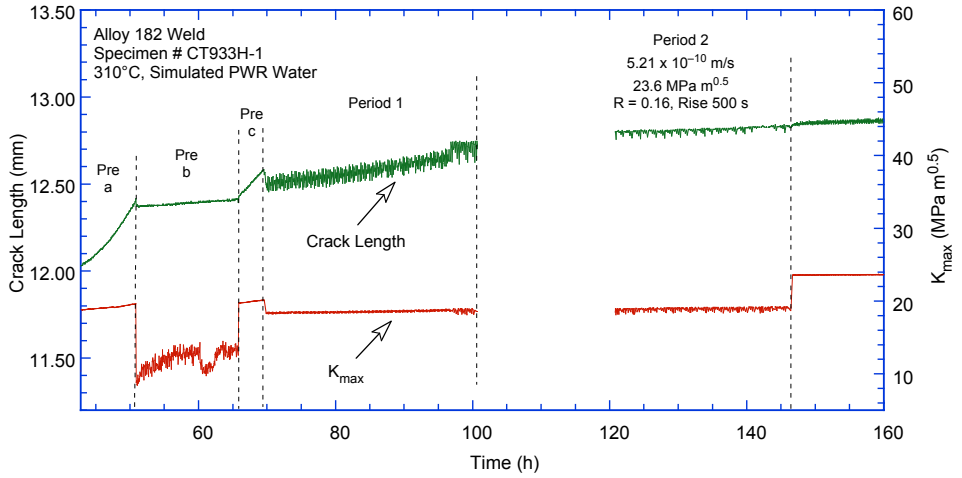

Figure 24. Crack length vs. time for Alloy 182 weld specimen CT933H-1 in simulated PWR environment during test periods (a) precracking-2, (b) 3-4, (c) 5-6, and (d) 7-8.

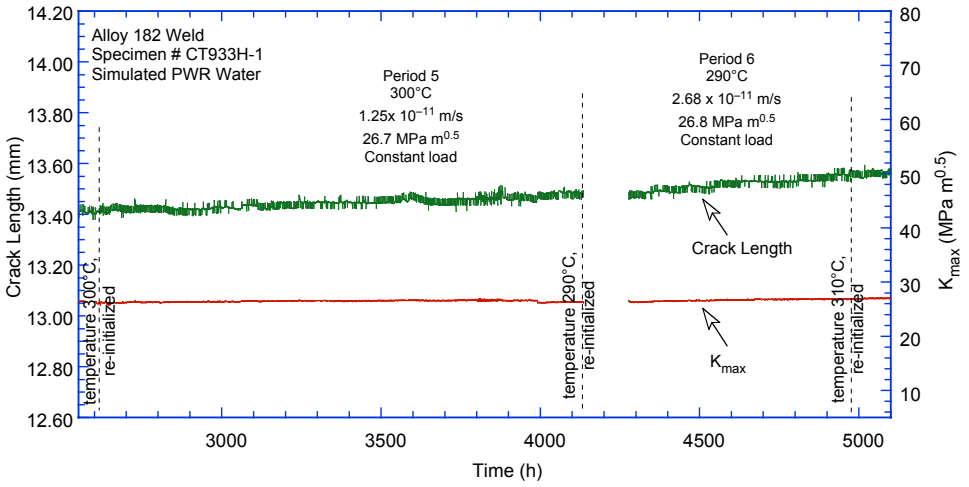

(c)

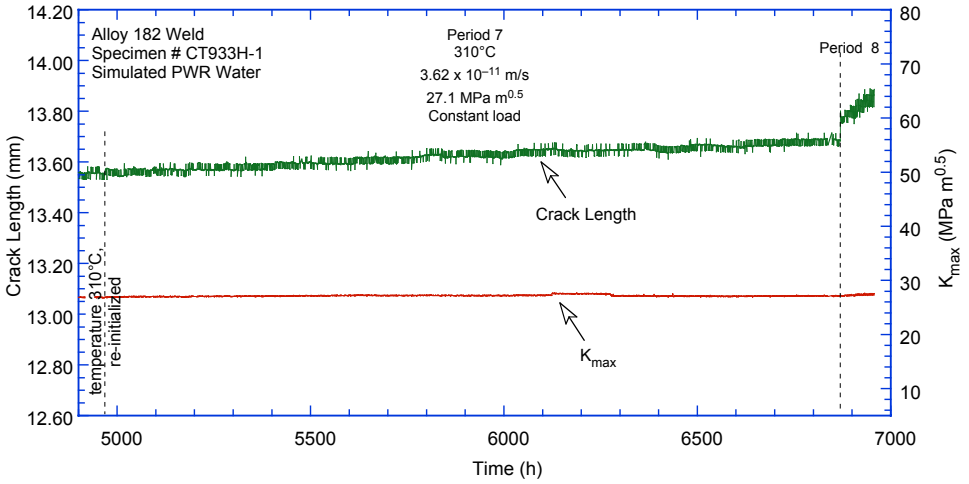

(d)

Figure 24. (Cont.)

4.3 Deep-Groove Weld Specimen CT933H-2

This test was conducted with the CT933H-2 specimen in the temperature range 290-350°C (554-662°F). The test on CT933H-2 (companion of CT933H-1) was started at 350°C. After a steady-state CGR was obtained at 350°C, the temperature was reduced to 320°C and then to 290°C. Finally, the temperature was increased back to 350°C.

The specimen CT933H-2 was fatigue precracked in the environment at 350°C with K_{max} = 25 MPa $m^{1/2}$ (22.8 ksi $in^{1/2}$), R = 0.45, and a triangular waveform, and then cycled at R = 0.60 with increasing rise times up to 500 s. The specimen was next set at constant load. The specimen was further cycled with increasing rise times, 500 and 1000 s, then set at constant load again. After the sequence was repeated three times, yielding three CGR measurements at 350°C, the temperature was decreased to 320°C. The hydrogen concentration in water was decreased from 48 to 23 cc/kg by lowering the hydrogen gas overpressure on the supply tank. Next, the temperature was further reduced to 290°C, and the hydrogen concentration was further reduced to 11 cc/kg. After approximately 800 h at 290°C the temperature was increased back to 350°C (hydrogen concentration of 48 cc/kg) for the final period.

The entire fracture surface of the CT933H-2 specimen is shown in Fig. 25. The image of Fig. 25 was used for data correction. The correction factors were 1.17 for the transgranular region and 3 for the intergranular region. The testing conditions are shown in Table 6, and the changes in crack length and K_{max} with time are shown in Fig. 26.

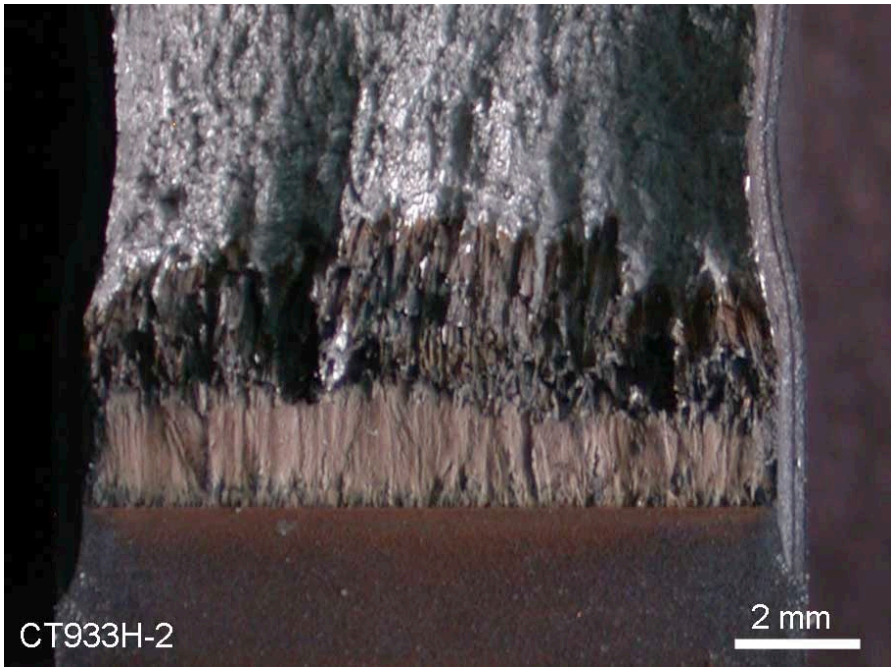

Figure 25. Fracture surface of Alloy 182 weld specimen CT933H-2 tested in simulated PWR environment at temperatures of 290-350°C.

Table 6. Test conditions and crack growth data for specimen CT933H-2 of Alloy 182 SMA weld in PWR water.[a]

Test Period	Test Time (h)	Temp. (°C)	H Conc. (cc/kg)	O_2 Conc.[b] (ppb)	Load Ratio R	Rise Time (s)	Down Time (s)	K_{max} (MPa $m^{1/2}$)	ΔK (MPa $m^{1/2}$)	CGR_{env} (m/s)	Estimated CGR_{air} (m/s)	Crack Length (mm)
1	49	351	47	<10	0.45	0.50	0	18.8	13.5	5.10E-08	6.06E-08	12.059
2	62	351	47	<10	0.46	100	100	18.4	13.2	2.05E-09	5.57E-10	12.101
3	69	351	47	<10	0.45	1.0	1	21.9	15.8	1.24E-07	1.15E-07	13.211
4	97	351	47	<10	0.61	50.0	12	22.3	8.7	2.12E-09	2.60E-10	13.288
5	269	351	47	<10	0.61	500.0	12	22.2	8.7	2.84E-10	2.55E-11	13.594
6	929	351	47	<10	1.00	-	-	23.4	0.0	6.49E-11	-	13.764
7	936	351	47	<10	0.50	500.0	12	25.8	12.9	1.02E-09	9.00E-11	13.794
8	1029	351	47	<10	0.50	1000.0	12	25.9	13.0	5.04E-10	4.60E-11	13.963
9	1096	351	47	<10	1	-	-	25.9	0.0	1.06E-10	-	14.009
10	1200	351	47	<10	0.50	500.0	12	26.8	13.4	2.34E-10	1.05E-10	14.111
11	1342	350	47	<10	0.50	1000.0	12	27.2	13.6	9.21E-11	5.58E-11	14.143
12	1717	351	47	<10	1	-	-	26.8	0.0	4.65E-11	-	14.177
13	2428	320	23	<10	1	-	-	27.0	0.0	1.36E-10	-	14.601
14	3240	291	11	<10	1	-	-	28.8	0.0	2.72E-11	-	14.683
15	3402	352	47	<10	1	-	-	29.3	0.0	4.53E-10	-	14.821
16	3434	352	47	<10	0.50	500.0	12	30.0	15.0	6.50E-09	1.68E-10	15.727
17	4,294	352	47	<10	1	-	-	35.2	0.0	6.59E-11	-	15.771
18	4,382	351	47	<10	0.50	500.0	12	35.5	17.7	3.84E-09	3.35E-10	16.036

[a]Simulated PWR water with 2 ppm Li, 1100 ppm B, and 2 ppm. Conductivity was 22 ± 3 μS/cm, and pH was 6.4.
[b]Represents values in the effluent.

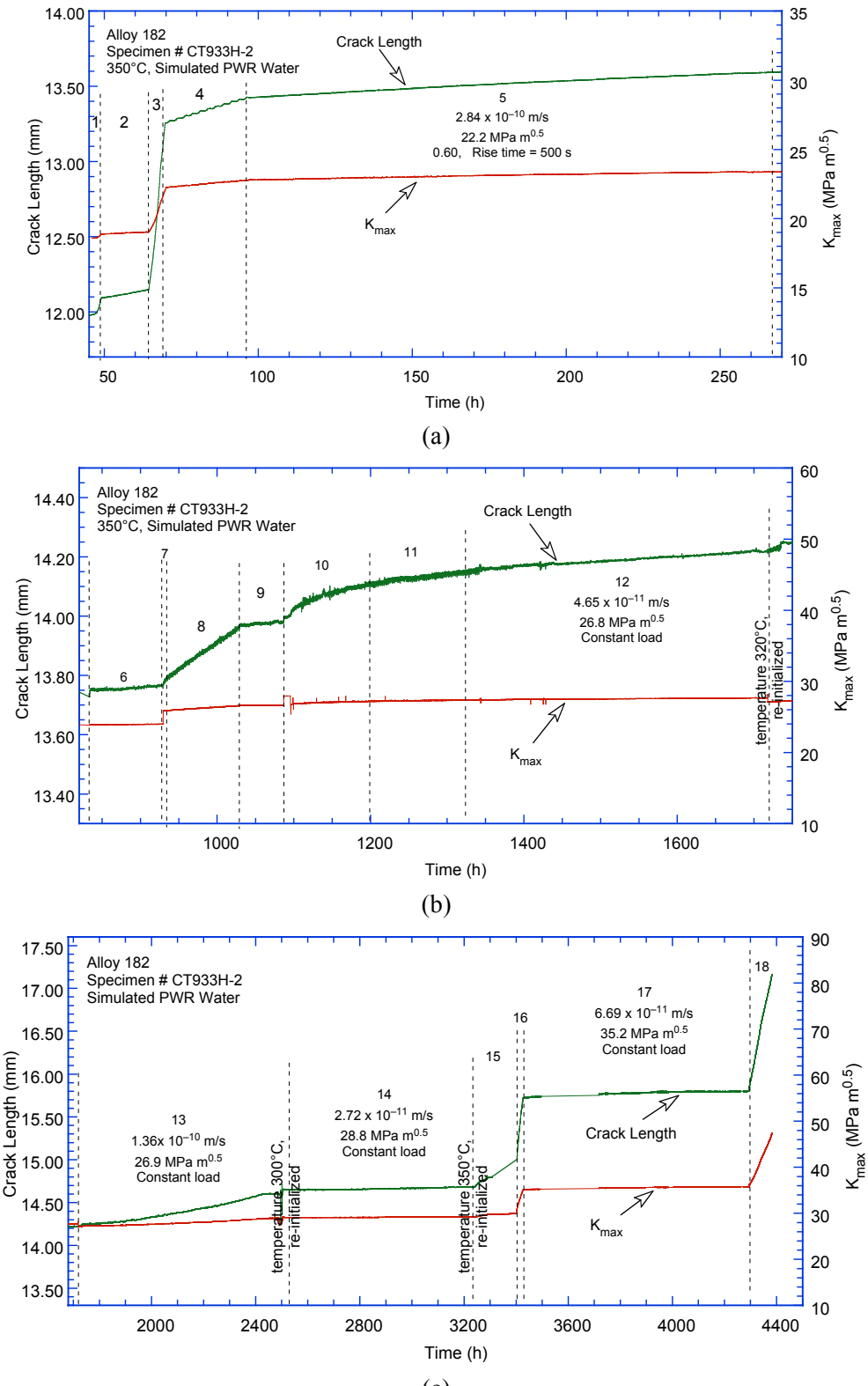

Figure 26. Crack length vs. time for Alloy 182 weld specimen CT933H-2 in simulated PWR environment during test periods (a) 1-5, (b) 6-12, and (c) 13-18.

5. Discussion

The section summarizes the crack growth rate results for Alloy 600 (obtained previously in the program) and Ni-base alloy welds (obtained from present and past efforts). The materials tested include both laboratory-prepared alloys and field components from Davis-Besse and V. C. Summer reactors. The most recent SCC CGR data on Alloy 182 are analyzed to extract the activation energy for crack growth in this alloy. In addition, the cyclic CGRs are analyzed with a superposition model for the purpose of establishing the individual contributions of mechanical fatigue, corrosion fatigue, and SCC.

5.1. SCC Growth Rates

5.1.1 Alloy 600

The experimental CGRs for Alloy 600 (Heat M3935) from the Davis-Besse CRDM nozzle under constant load, with or without partial unloading, are plotted as a function of applied K_{max} in Fig. 27a. The cumulative distribution of the log-normal fit to the ordered median ranking of the constant α (Eq. 16) for various data sets of Alloy 600 is shown in Fig. 27b. The experimental CGRs for Alloy 600 from the CRDM nozzle #3 correspond to the ≈95th percentile of the distribution fitted to the various data sets (i.e., Heat M3935 of Alloy 600 from the Davis-Besse CRDM nozzle #3 exhibits very high susceptibility to PWSCC). The median and 75th percentile CGR curves developed by the MRP for thick-wall Alloy 600 are also included in the figure.[44] The growth rates for the Davis-Besse nozzle Alloy 600 are a factor of ≈ 4-8 higher than the median curve and are a factor of ≈ 2-4 higher than the 75th percentile curve, which has been proposed as a disposition curve.

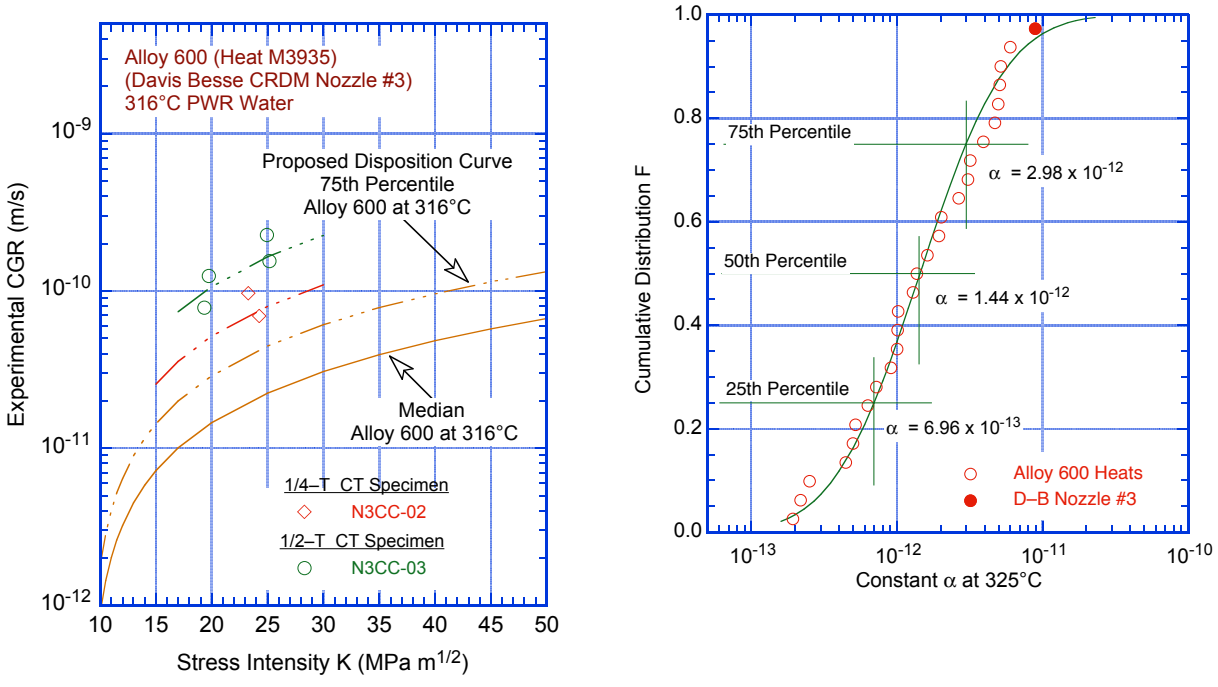

(a) (b)

Figure 27. (a) CGR data for Alloy 600 from Davis-Besse CRDM nozzle #3 in PWR water at 316°C (601°F) under constant load and (b) log-normal distribution of constant α for 26 heats of Alloy 600.

Based on the observed microstructure and tensile strength of the nozzle Alloy 600,[33] the experimental CGRs are somewhat surprising. Materials with good grain boundary carbide coverage (Fig. 16) and relatively low or average tensile yield stress are generally considered to have low susceptibility to SCC in PWR water.[4] A unique feature of the fracture surface for the Davis-Besse nozzle alloy is the predominantly IG fracture even during mechanical fatigue loading (Fig. 28).

The high susceptibility for the material to PWSCC cannot be reconciled in terms of the tensile strength or microstructure of the alloy. Additional CGR data and metallographic evaluation of Alloy 600 from service components are needed to understand better the environmentally assisted cracking behavior of Alloy 600 in PWR environments.

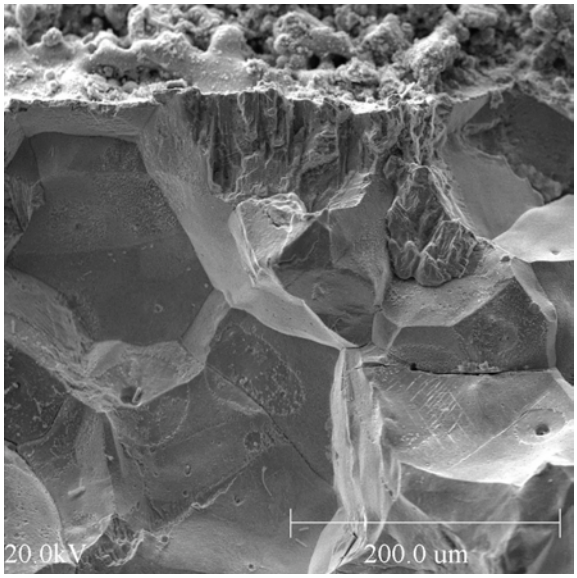

Figure 28.
Transition from TG to IG fracture mode in specimen N3CL-1. The sample notch is at the top of the figure, and crack advance is from top to bottom.

5.1.2 Ni-Alloy Welds

Experimental SCC CGRs obtained from the ANL tests on laboratory-prepared Alloy 182 weld specimens[32] are plotted as a function of stress intensity factor K in Fig. 29a and are compared with available CGR data for Ni-alloy welds[59-68] in Fig. 29b. The double-J and deep groove welds are different heats of material as well as different weld geometries. The disposition CGR curve proposed by the White and Hickling[45] for Alloy 182 in the PWR environment is also plotted in the figures. The disposition curve was developed for a temperature of 325°C (617°F), and the version of the disposition curve in Fig. 29a was normalized to 320°C (608°F) using Eq. 17 and an activation energy of 130 kJ/mol (31 kcal/mol). In Fig. 29b for comparison with the available SCC CGR data, the ANL test results were normalized to 325°C (640°F). Most of the data for Alloys 182 and 82 welds are between the median Alloy 600 curve and a factor of 10 above this curve, suggesting that the median curve for weld materials is about a factor of 3 greater than that for Alloy 600.

In the ANL tests, CGRs were measured along the plane of the columnar grains/dendrites in a direction parallel to the columnar grains (TS or LS orientation) and perpendicular to the columnar grains (TL orientation). Note that the crack planes for TS and LS orientations are along the columnar dendrites, although they are perpendicular to each other. The results indicate that at high K values the CGRs for cracks propagating along the direction of dendrites (orientations TS and LS) are about a factor of two

greater than the CGRs for crack propagation across the direction of dendrites (orientation TL) (Fig. 29a). Similar results have also been obtained in other studies.[59,60,63,64]

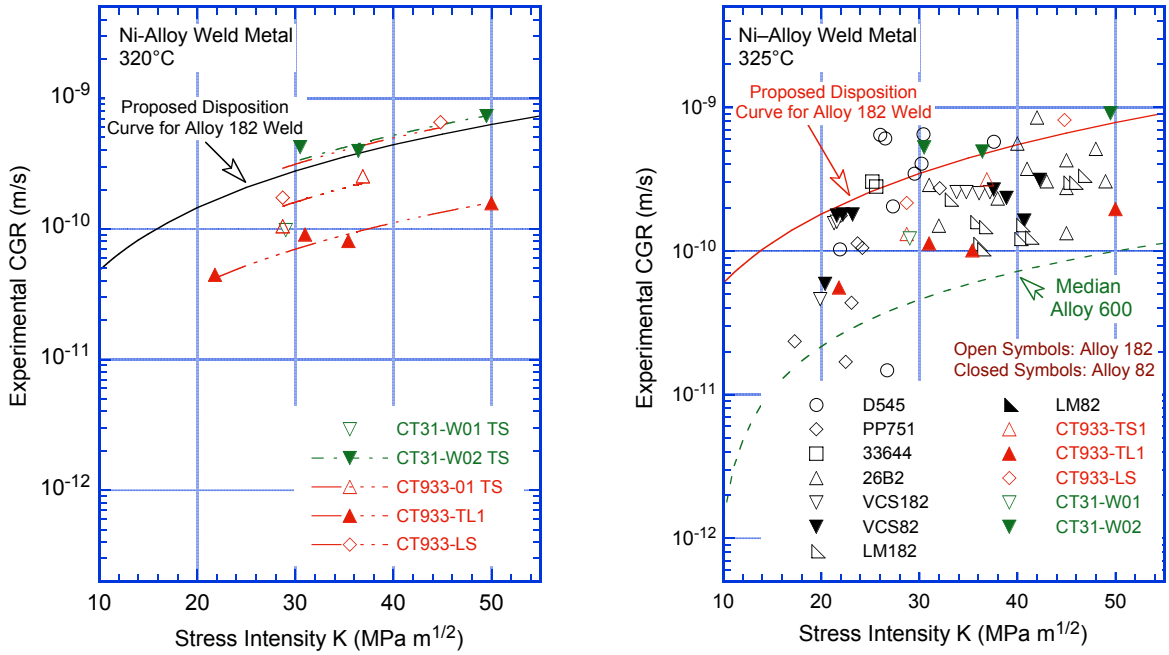

(a) (b)

Figure 29. SCC crack growth data for the Argonne Alloy 182 welds (a) plotted as a function of K and (b) compared with the available data for Alloy 182 and 82 welds in simulated PWR environment. Data from Refs. 59-68.

The experimental SCC growth rates for Alloy 182 from the Davis-Besse nozzle #11 J-groove weld under constant loading conditions (with or without periodic partial unloading) are shown in Fig. 30. The proposed disposition curve for Alloy 182 welds in a PWR environment[45] is also included in the figure. The disposition curve was normalized to 316°C (600°F) using Eq. 16 and an activation energy of 130 kJ/mol (31 kcal/mol). The CGRs for the Davis-Besse J-groove weld (in red in the figure) are an order of magnitude lower than the disposition curve proposed for Alloy 182 weld metals.[45]

The experimental CGRs under constant load for the two V.C. Summer weld and butter alloys are compared with similar data obtained on laboratory-prepared welds in Fig. 31a. The CGRs for the V.C. Summer alloys are comparable to those determined for the Davis-Besse CRDM nozzle J-groove weld. The proposed disposition curve for Alloy 182 welds in a PWR environment[45] is also included in the figure. The results indicate that the CGRs of Alloy 82 weld material (specimens WLR-01 and WCR-01) with growth direction along the dendrites are comparable to those of the Alloy 182 butter material (specimen BCR-01) with growth direction transverse to the dendrites. Note that the crack planes for LR and CR orientations are along the columnar dendrites, although they are perpendicular to each other (where L = longitudinal, C = circumferential, and R = radial). In general, CGRs in Alloy 182 are a factor of 2.6 higher than in Alloy 82; however, the rates along a direction transverse to the dendrites are a factor of ≈2 lower than those parallel to the dendrites.[45] The effects of alloy type and specimen orientation seem to have cancelled each other, yielding approximately the same growth rates for the weld and butter alloys.

Figure 31b shows the V.C. Summer CGR data plotted along with data obtained by Jacko et al.[67] on similar V.C. Summer weld and butter alloys in the PWR environment at 325°C (640°F); the ANL results were normalized to 325°C for comparison (Eq. 17). The CGRs obtained at ANL are a factor of ≈4 lower than those obtained by Jacko et al. The reasons for the differences in the results between the two studies are not clear. The crack fronts in the tests reported here are relatively straight. The crack fronts in the tests in Jacko et al.[67] do not appear to be as straight. The CGRs in isolated "fingers" may be more rapid than the overall growth of a straight crack front.

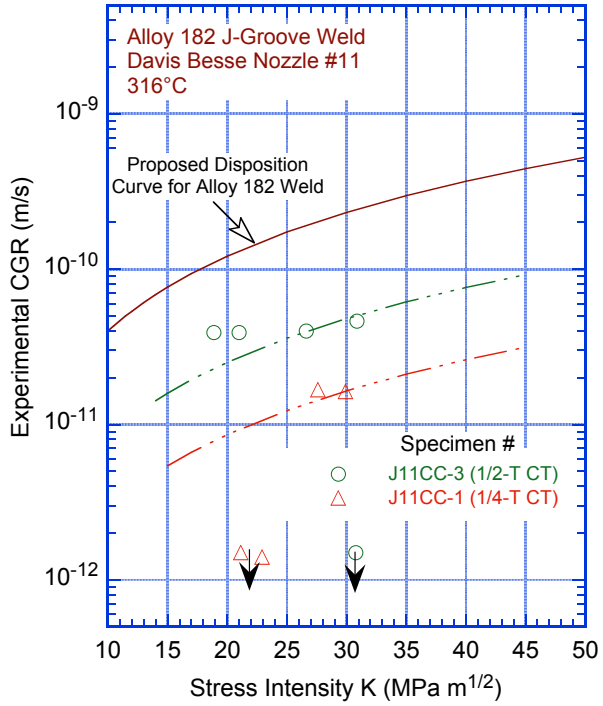

Figure 30.
CGR data for Alloy 182 from the Davis-Besse CRDM nozzle J-groove weld in PWR environment at 316°C (600°F) under constant load.

Figure 32 shows the cumulative distribution of the log-normal fit to the ordered median ranking of the constant α in Eq. 17 for various data sets of Ni-alloy welds available in the literature; it essentially represents a means of ranking the various heats with respect to their susceptibility to SCC. However, the experimental CGRs were first adjusted for incomplete initiation of SCC, temperature, orientation, and alloy type, as follows: (a) divide by the engagement fraction to allow for incomplete initiation, (b) use Eq. 17 and an activation energy of 130 kJ/mol (31 kcal/mol) to normalize the CGR data to a common reference temperature of 325°C (640°F), (c) multiply the CGRs for TL orientations by 2 to account for orientation effects, and (d) multiply the CGRs for Alloy 82 welds by 2.6 to account for the effects of alloy type. Also, studies at CEA[65] generally report only the maximum values of CGR; the average CGRs were determined from the maximum values by using the correlation proposed by Attanasio et al.[62] The ratio between the maximum and average CGR was assumed to be the same as the ratio between the maximum and average crack extension (i.e., $R = \Delta a_{max}/\Delta a_{ave}$). The ratio R is expressed as

$$\ln(R - 1) = 2.48 - 0.762 \ln(\Delta a_{ave}/0.051), \quad (18)$$

where crack extension is in millimeters. The results of Jacko et al.[67] suggest that the V. C. Summer weld and butter alloys correspond to the ≈95th and 80th percentile, respectively, of the distribution of the various heats, whereas the results from the present study indicate that they correspond to the ≈25th and 10th percentile, respectively.

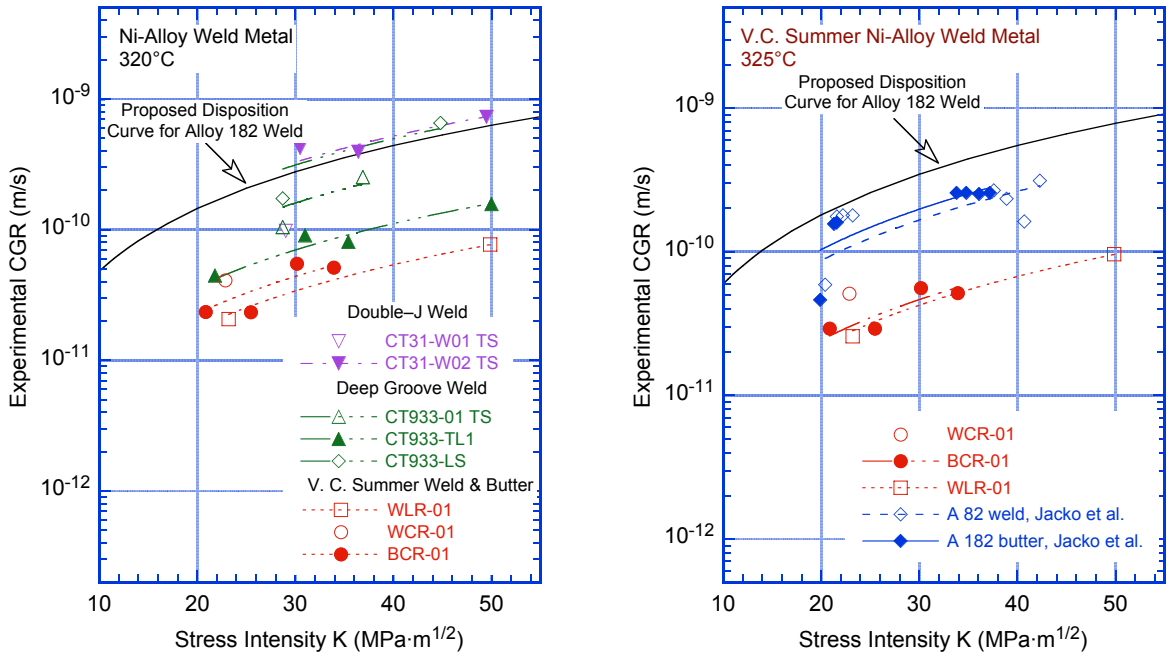

(a) (b)

Figure 31. Comparison of the CGR data for the V.C. Summer weld and butter alloys with the data obtained on (a) laboratory-prepared welds in the present study and (b) V. C. Summer weld and butter alloys by Jacko et al. (Ref. 67).

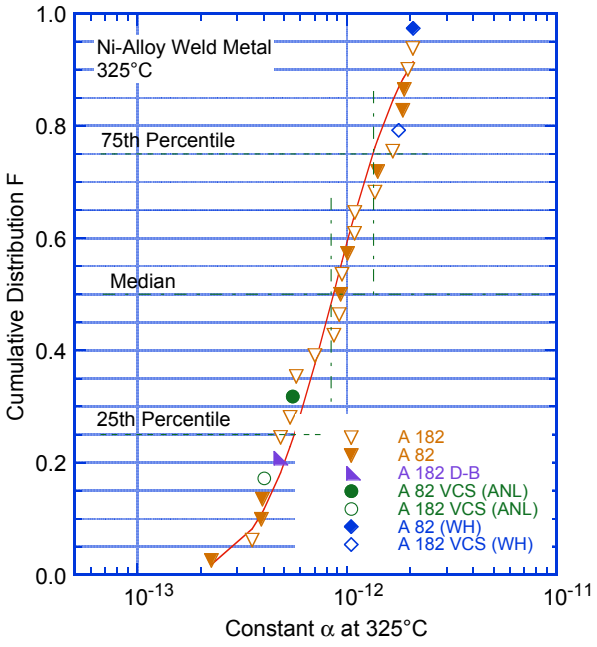

Figure 32.
Log-normal distribution of constant α for several heats of Alloy 82 and 182.

The ANL results indicate that the SCC growth rates for the field weld alloys from the Davis-Besse and V. C. Summer reactors are lower than the average CGRs for Alloy 182 welds. The results are not inconsistent with the heat-to-variability expected from laboratory tests. However, it is possible that other factors are at work. For example, field welds may be under a higher degree of structural constraint than laboratory-prepared welds.

A common feature observed in all test specimens, with the exception of one V.C. Summer specimen, is the cracks on the fracture surface where the propagating SCC cracks seem to arrest. Figure 33 illustrates this behavior with micrographs of the fracture surface from the Davis-Besse specimen J11CC-1 (Fig. 33a) and V. C. Summer specimen BCR-01 (Fig. 33b). The cracks occurred most likely during the laboratory CGR tests because they were not observed during the metallographic examinations. Furthermore, it can be hypothesized that the development of such cracks relieves the stress driving the propagation of the main crack. However, the cause for these cracks is unknown, although they could be associated with the greater constraint typically present in field welds, and determining their effect on the SCC behavior requires further investigation.

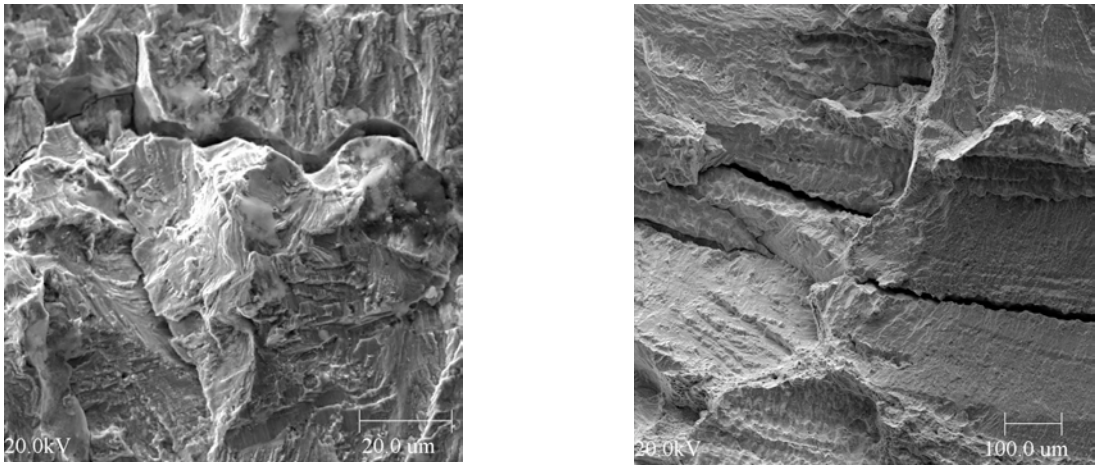

(a) (b)

Figure 33. Micrographs from the fracture surface of weld specimens: (a) Davis-Besse J11CC-1, and (b) V.C. Summer BCR-01.

5.2. Activation Energy for SCC Crack Growth

The available CGR vs. temperature data for Alloy 82 are plotted in Fig. 34. The different data sets yield activation energies that are either comparable to that observed for Alloy 600 (130 kJ/mol) (e.g., Bechtel Bettis[59,60] and ETH[61]) or a factor of ≈2 higher (e.g., Lockheed Martin[62]). However, the corrosion potential for the Bechtel Bettis tests conducted at 360°C (680°F) with 150 cc/kg hydrogen was farther removed from the Ni/NiO phase transition than in the case of the 338°C (640°F) tests with 40-60 cc/kg hydrogen. As such, since the CGRs are highest near the Ni/NiO phase transition and decrease as the potential deviates from this transition,[36,37] the CGRs in the 360°C tests may have been reduced because of the high dissolved hydrogen levels. Thus, the actual activation energy for the Bechtel Bettis data may be somewhat higher than that determined in Fig. 34a.

Figure 35 shows the Alloy 182 temperature dependence of the CGR data obtained at Westinghouse[63,64] and CEA[65]. The resulting activation energies, 228 and 248 kJ/mol, are in very good agreement with each other. While the data are limited, they seem to suggest that the activation energy for the temperature dependence of CGRs in Alloys 182 welds may be higher than that in Alloy 600.

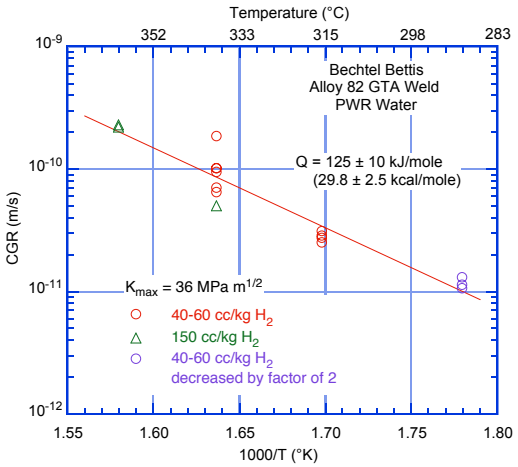

(a)

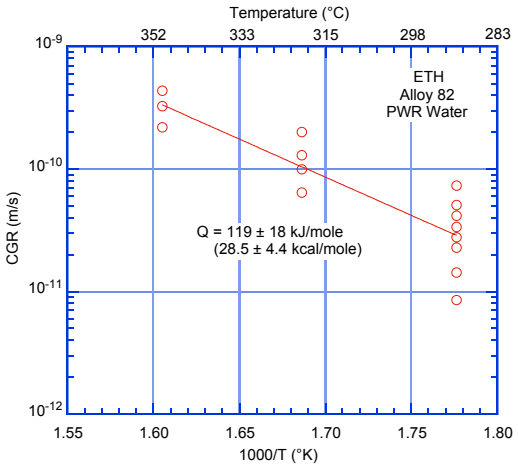

(b)

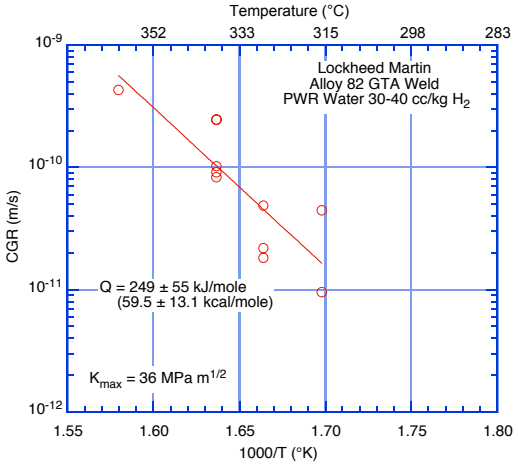

(c)

Figure 34.
Temperature dependence of the CGR data for Alloy 82 obtained at (a) Bechtel Bettis, (b) ETH, and (c) Lockheed Martin at temperatures between 290°C (554°F) and 360°C (680°F) (Refs. 59-62).

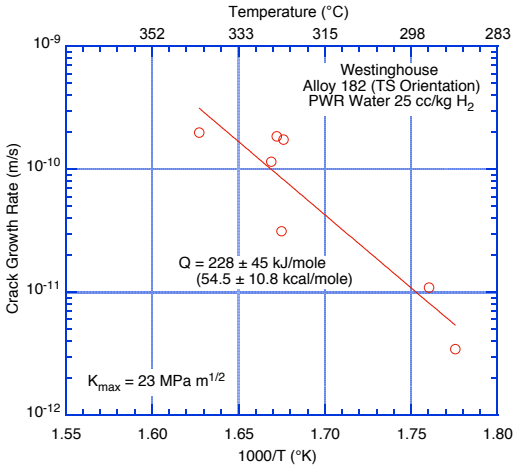

(a)

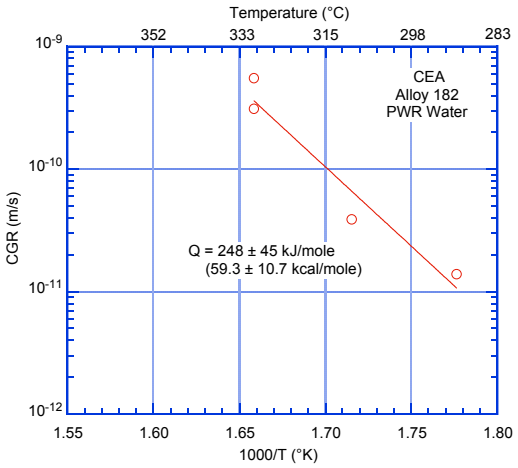

(b)

Figure 35. Temperature dependence of the CGR data for Alloy 182 obtained at (a) Westinghouse and (b) CEA at temperatures between 290°C (554°F) and 340°C (644°F) (Refs. 63-65).

Figure 36 shows the temperature dependence of the CGR data for the three specimens (A182-1, CT933H-1, and CT933H-2) tested at ANL. In addition, data generated previously at 320°C (608°F) are also included. The colors in the plot identify the type of weld: red for deep-groove and blue for double-J. Also, the 1-T specimens are shown with open symbols, and the 1/2-T specimens are shown with solid symbols. Note that in addition to the difference in weld geometry, the two welds were prepared from different heats of Alloy 182. The CGR data for the double-J welds yields an activation energy of 252 kJ/mol (59 kcal/mol). This value is in excellent agreement with the literature data shown in Fig. 35. Similarly, the activation energy for the deep-groove Alloy 182 weld was calculated to be 189 kJ/mol (33 kcal/mol). For this latter calculation, the CGR data points obtained at 350°C (662°F) were excluded because the data suggest a plateau in CGR at temperatures beyond 320°C (608°F) (see the dotted line in Fig. 36). The average value of the activation energy based on the available data is 229 kJ/mol (54.6 kcal/mol). As shown in Fig. 37, the distribution of observed values is at least roughly normal. The lower 5th percentile estimate of the activation energy is 182 kJ/mol (43 kcal/mol). Thus, the results clearly indicate that the activation energy for Alloy 182 is greater than that commonly used for Alloy 600, 130 kJ/mol (31 kcal/mol), and that a value of about 220-230 kJ/mol (52.4-54.8 kcal/mol) is a better descriptor for the CGR vs. temperature dependence of Alloy 182.

The average value for Alloy 82 is 164 kJ/mol (39 kcal/mol), which is somewhat greater than that assumed for Alloy 600, but the uncertainty in the value makes it more difficult to justify the use of a higher activation energy.

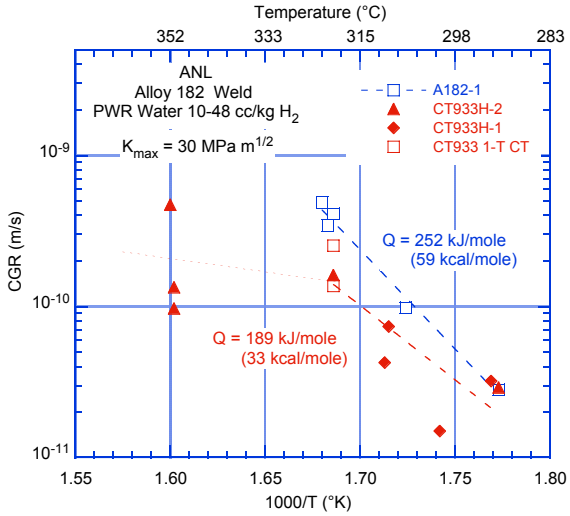

Figure 36.
Temperature dependence of the CGR data for Alloy 182 obtained at ANL at temperatures between 290°C (554°F) and 350°C (662°F).

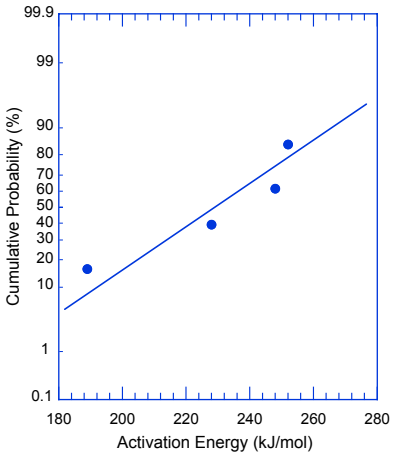

Figure 37.
Comparison of observed activation energies for Alloy 182 with a normal distribution.

5.3. Consequence of Using a Larger Activation Energy

Because much of the database on CGRs in Ni-alloy weld materials has been obtained at different test temperatures, it is necessary to normalize the data to a single temperature for the purpose of comparison.[45] This normalization has been previously done by using the activation energy for Alloy 600, 130 kJ/mol (31 kcal/mol).[45] This section analyzes the effect of using the larger value of 220 kJ/mol (52.4 kcal/mol) to carry out the normalization.

Figure 38 shows a comparison of the cumulative distribution of the parameter α in the CGR relationship (Eq. 17) for Ni-alloy welds[45] with the data normalized to 325°C (617°F) using activation energies of 130 kJ/mol and 220 kJ/mol. The 75th percentile value of ln(α) becomes -27.5396, yielding a value of 1.1 x 10^{-12} at 325°C for the α parameter, which is ≈36% lower than the corresponding value of α, 1.5 x 10^{-12}, obtained using a value of 130 kJ/mol for the normalization. Thus, the current approach yields somewhat more conservative values. If 1.1 x 10^{-12} is used instead of 1.5 x 10^{-12} in Eq. 17, the disposition curve takes the form:

$$\dot{a}_{Ni-weld} = 1.1\times10^{-12}\exp\left[-\frac{Q}{R}\left(\frac{1}{T}-\frac{1}{T_{ref}}\right)\right]K^{1.6}. \qquad (19)$$

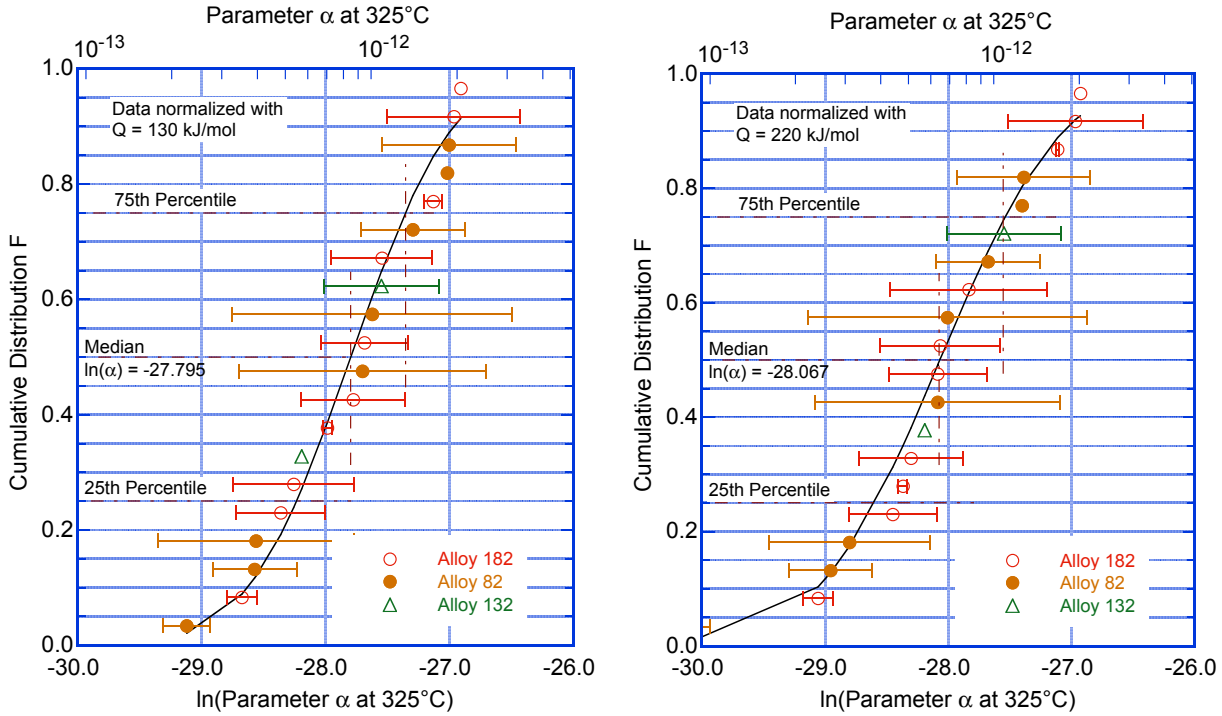

Figure 38. Cumulative distribution of the parameter α in the CGR relationship for Ni-alloy welds with the data normalized to 325°C (617°F) using an activation energy of (a) 130 kJ/mol and (b) 220 kJ/mol.

Figure 39 shows the effect of using the larger value of the activation energy on the proposed disposition curve for Alloy 182.[45] The data in the figure are from field welds from V. C. Summer and Davis-Besse plants. The data obtained in this program are shown with red symbols while the data from

the literature[67] are shown with blue symbols. Also included for comparison is the proposed disposition curve for Alloy 600.[45] While less conservative, the disposition curve obtained using an activation energy of 220 kJ/mole for normalization bounds the available data for field welds. This curve and the disposition curve for Alloy 600 bound most of the data obtained for field welds in the ANL program. The data obtained in the ANL program also seems close to the Alloy 600 disposition curve suggesting that the difference in cracking behavior between field weld alloys and Alloy 600 may not be as large as the two proposed disposition curves might suggest.

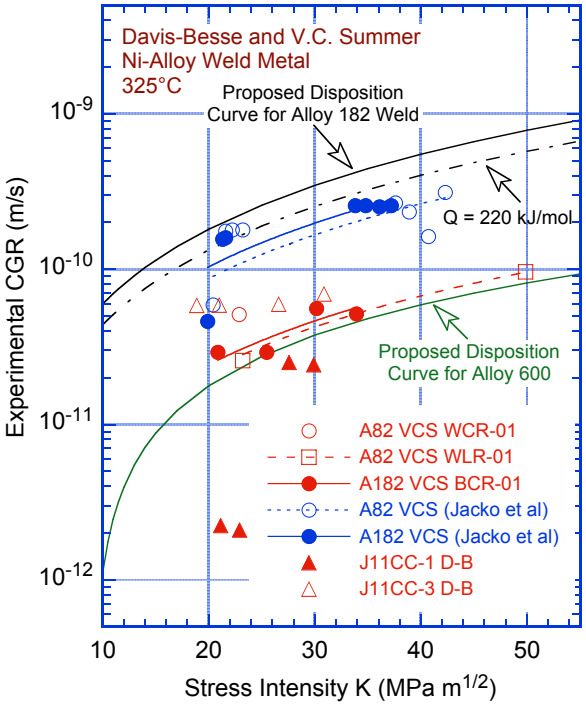

Figure 39.
CGR data for the V.C. Summer weld and Davis-Besse weld alloys. Also included are data on V.C. Summer weld alloys by Jacko et al. (Ref. 67).

5.4 Cyclic Crack Growth Rates in PWR Environment

5.4.1 Alloy 600

The cyclic CGRs for the Alloys 600 specimens obtained in the ANL program have been evaluated to develop correlations for estimating the cyclic CGRs in Alloy 600 as a function of loading and environmental conditions. The data were obtained from tests conducted with a triangular or slow/fast sawtooth waveform. The load ratio R was in the range of 0.2-0.9, K_{max} was in the range of 30-50 MPa $m^{1/2}$ (27.3-45.5 ksi $in^{1/2}$), and the rise time was 12 s for most of the tests.[26-28,31]

The experimental CGRs in the PWR environment at 320°C and those predicted in air for the same loading conditions for several heats (and heat treatment conditions) of Alloy 600 are shown in Fig. 40. Preparation conditions included mill annealing (MA), solution annealing (SA) plus thermal treatment (TT), and SA alone. The tests on Heats NX8844J-26 and NX131031 and some of the tests on Heat NX8197 were performed in deaerated water with <5 ppb DO. Also, the rise time for Heat NX131031 was 60-5000 s. In this figure, the data points that lie along the diagonal represent predominantly mechanical fatigue, and those away from the diagonal indicate environmentally enhanced crack growth. The results indicate that unlike the crack growth behavior in high-DO BWR water where all heats of

Alloy 600 showed environmental enhancement,[31] only two heats of Alloy 600 show environmental enhancement of CGRs in low-DO PWR water. Environmental enhancement is observed for solution-annealed Heat NX9244G and some specimens of this heat in the thermally treated condition, as well as for Heat NX131031; for the latter heat, the load ratio was 0.7, and rise times were 60-5000 s. These results indicate that in addition to material conditions such as yield strength and grain-boundary coverage of carbides, long rise times and high R values also seem to be important for environmental enhancement of growth rates in PWR water.

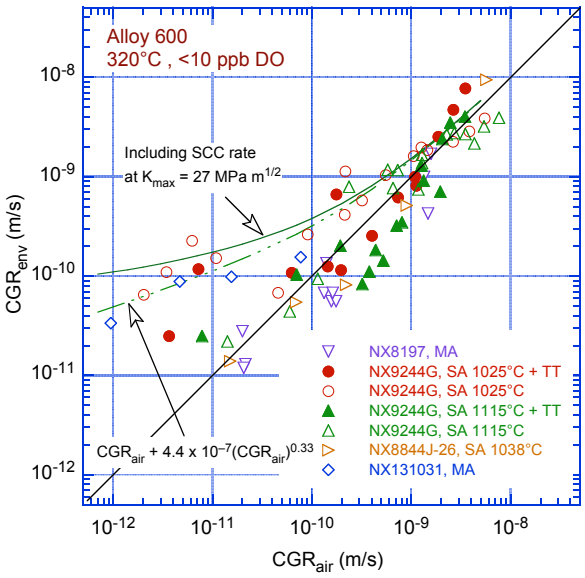

Figure 40.
Cyclic CGR data for several Alloy 600 heats in deaerated water at 320°C (608°F) under cyclic loading.

The uppermost solid line in the figure is based on the superposition model (Eq. 10), that is, the growth rate in the environment is determined from the superposition of the rate in air (Eqs. 11 and 12) and rates due to corrosion fatigue (Eq. 14) and SCC (Eq. 16). For cyclic loading using either a triangular or a slow/fast sawtooth waveform, $\dot{a}_{SCC}$ is determined by considering the contribution of SCC during the slow rise time of the cycle; an equivalent K_{max} is computed to determine the contribution of fatigue loading. The average value of K_{max} used in calculating the superposition curves is given in the figure.

The experimental CGRs for Alloy 600 from the Davis-Besse CRDM nozzle #3 and those predicted in air for the same loading conditions are shown in Fig. 41. The crack plane represents a circumferential crack in the CRDM nozzle for specimen N3CL-01 and an axial crack for specimens N3CC-02 and N3CC-03. The tests were conducted with a slow/fast sawtooth waveform, load ratio of 0.3-0.7, and rise times of 5-1000 s. As expected, specimen orientation does not seem to have any effect on growth rates (e.g., the CGRs for N3CL-1 and N3CC-3 are comparable and those for N3CC-2 are slightly lower).[33] Although the results show considerable scatter, the CGRs for the Davis-Besse CRDM nozzle Alloy 600 are generally higher than those for the heats of Alloy 600 tested earlier (Fig. 40).

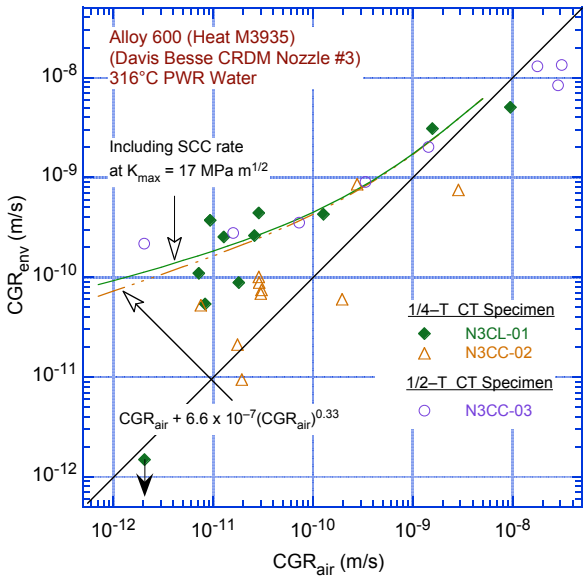

Figure 41.
CGR data for Davis-Besse CRDM nozzle #3 Alloy 600 in PWR water at 316°C (601°F) under cyclic loading.

The uppermost solid line in Fig. 41 is also based on the superposition model. For the loading conditions used in these tests, the average equivalent K_{max} is ≈17 MPa $m^{1/2}$ (15.5 ksi $in^{1/2}$) The contribution of the SCC growth rate, $\dot{a}_{SCC}$, is relatively small. Also, for the Davis-Besse nozzle alloy, the corrosion fatigue growth rate $\dot{a}_{CF}$ is better represented by

$$\dot{a}_{env} = \dot{a}_{air} + 6.6\times10^{-7} \cdot (\dot{a}_{air})^{0.33} . \qquad (20)$$

In Fig. 40 the cyclic CGRs in the PWR environment are represented by the best-fit curve for Alloy 600 in high-temperature water determined previously in our program (Eq. 14).[31] Even when the expected SCC contribution is added, the prediction underestimates the data. Therefore, a new best-fit curve was calculated based on cyclic data for Davis-Besse Alloy 600. This approach was warranted because, in all three Davis-Besse Alloy 600 specimens, the fracture mode was IG regardless of the loading conditions. The fracture mode appeared to have changed to IG from the very first grain boundary encountered (hence, the enhanced cyclic CGRs). The other two specimens exhibited either a predominant IG (N3CC-2) or a partial IG (N3CC-3) fracture mode during precracking.

The Davis-Besse CRDM nozzle Alloy 600 exhibits a predominantly IG fracture even during fatigue loading. The fracture surface of specimen N3CL-1 near the machine notch is shown Fig. 28. Transgranular growth is observed at the very beginning of the test (i.e., near the machine notch), but changes to IG when the first grain boundary is encountered. The fact that IG growth takes place in a regime dominated by mechanical fatigue (which normally results in TG cracking) suggests that the grain boundaries may have suffered some form of sensitization during fabrication and/or during two decades in service. As noted previously, metallographic examination of nozzle #3 revealed what is typically considered a "good" microstructure (i.e., extensive grain-boundary coverage of Cr-rich carbides and relatively low or average tensile strength). These conditions are typically associated with low susceptibility of the material to PWSCC. Differences in the microstructure in terms of extent and nature of carbide precipitation and segregation of other impurities on the grain boundaries may be important and should be investigated. As such, the chemical compositions of the grain boundary carbides should be determined as well as any impurity and/or major element segregation at the boundary.

5.4.2 Ni-Alloy Welds

The cyclic CGR data on Ni-alloy welds in simulated PWR environments are available from ≈120 tests conducted on Alloys 182, 82, 152, and 52 at 243-345°C (469-653°F).[55-58] The loading conditions for these tests include R = 0.1-0.75, K_{max} = 20-100 MPa $m^{1/2}$ (18.2-91 ksi $in^{1/2}$), and rise time of 0.5-5000 s. The results indicate very little effect of PWR environment on the cyclic CGRs of these welds. However, only about 10% of the data was obtained under conditions for which significant environmental enhancement would be expected.

The cyclic CGR data obtained at ANL on laboratory-prepared Alloy 182 weld specimens[32] in the PWR environment at 320°C (608°F) are shown in Fig. 42a. For comparison, similar cyclic CGR data obtained by Van der Sluys et al.[57] on Alloys 82 and 52 in PWR environment at 315°C (600°F) are shown in Fig. 42b. In both figures, rates predicted from the superposition model are shown by the solid line, and those predicted without the SCC component are shown by the dashed line. For Alloy 182, select loading conditions appear to show minimal environmental enhancement; however, the vast majority do not. Similarly, the Alloy 82 data do not appear to show environmental enhancement. The conditions that resulted in environmental enhancement of CGRs in Alloy 182 are load ratios of R ≈ 0.7 and rise times of 1000 s.

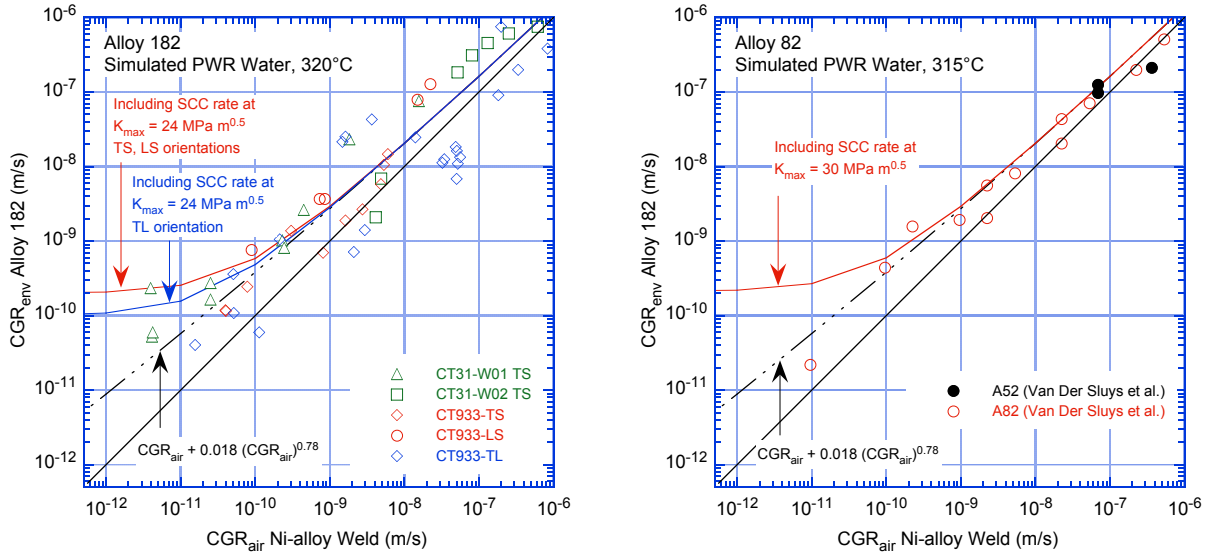

(a) (b)

Figure 42. CGR data in PWR environment for (a) Alloy 182 SMA weld at 320°C (608°F), and (b) Alloy 82 and Alloy 52 welds at 315°C (600°F) (Ref. 57) as a function of the growth rates for Alloy 182 weld in air.

Of the five laboratory-prepared Alloy 182 weld specimens (Fig. 42a), only specimen CT31-W01, tested at R = 0.7 and rise time = 1000 s, showed environmental enhancement of cyclic CGRs. For this specimen, the transition from TG to IG fracture mode is shown in Fig. 43. The images appear to indicate that the transition from TG to IG occurred readily.

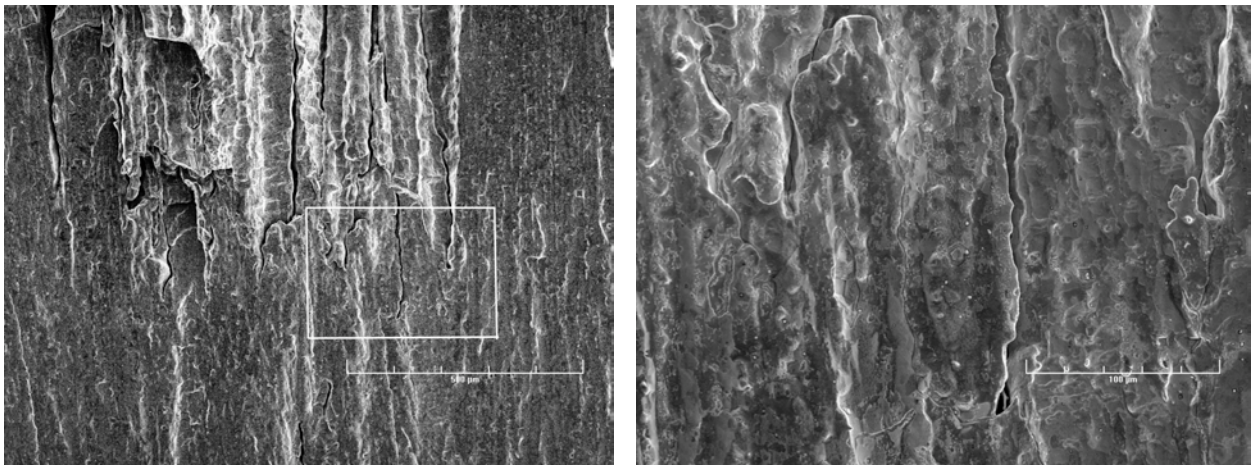

(a) (b)

Figure 43. (a) Transition from TG to IG fracture and (b) higher magnification micrograph of the boxed area showing the tip of a few secondary cracks. Crack extension from bottom to top.

Figure 44 shows the CGR data obtained at ANL on 1/2-T CT specimens of laboratory-prepared Alloy 182 weld in the PWR environment at 310-350°C (590-662°F) as a function of the rates for Alloy 182 weld in air under the same loading conditions. The solid lines represent rates predicted from the superposition model, and the dashed line represents the predicted rates without the SCC contribution. The cyclic CGR data for the three specimens are consistent with previous results summarized in Fig. 42. The loading conditions for these specimens did not include the conditions that resulted in enhanced growth rates in specimen CT31-W01 (R = 0.7 and rise time = 1000 s).

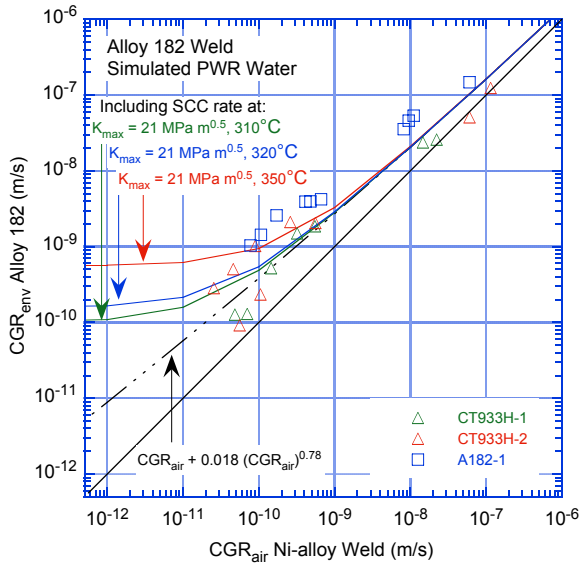

Figure 44.
CGR data for Alloy 182 SMA weld-metal specimens as a function of growth rates for Ni-weld alloy in air. The tests were conducted in simulated PWR environment in the 310-350°C (590-662°F) temperature range.

Figure 45 shows the cyclic CGR data in the PWR environment for Ni-alloy welds from field components plotted as a function of the growth rate in air under the same loading conditions. Figure 45a shows the data for Alloy 182 from the Davis-Besse CRDM nozzle #11 J-groove weld and V. C. Summer reactor vessel nozzle butter, and Fig. 45b shows the data for Alloy 82 from the V. C. Summer reactor vessel nozzle-to-pipe weld. For the V. C. Summer weld, the fracture plane in specimens WCR-01 and WLR-01 represents axial and circumferential through-wall cracks in the plane of the columnar

grains/dendrites and growing along the dendrites, while specimen BCR-01 represents axial through-wall cracks in the plane of the columnar grains/dendrites and growing across the dendrites.

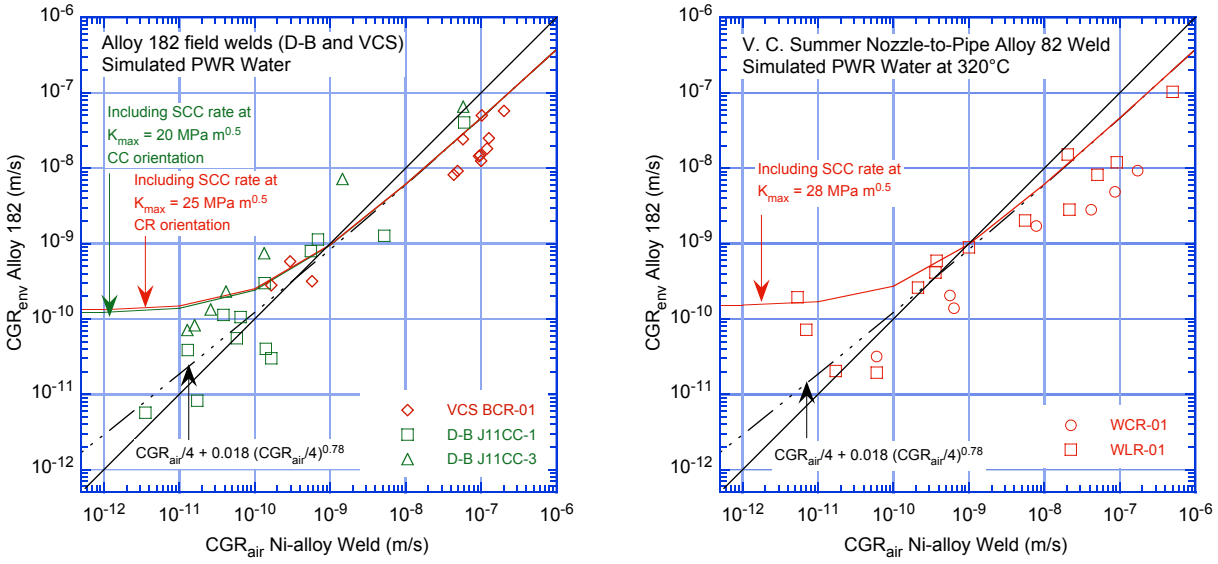

(a) (b)

Figure 45. Cyclic CGR data for (a) Alloy 182 and (b) Alloy 82 from the Davis-Besse CRDM nozzle J-groove weld and V.C. Summer reactor vessel nozzle-to-pipe weld.

The results indicate that the cyclic CGRs in air of the field welds are generally lower than those predicted by Eqs. 11 and 13 for laboratory-prepared Alloy 182 welds. In Fig. 45, under loading conditions that result in essentially mechanical fatigue (i.e., growth rates >1 x 10^{-9} m/s in air) the CGRs of the field welds are a factor of 3-6 lower than the predicted values. When environmental enhancement occurs, the CGRs in the PWR environment compared with those in air increase with decreasing CGRs in air. As before, the solid and dashed lines are based on the superposition model with and without the SCC contribution, respectively. The SCC contribution for the Alloy 82 weld was computed by considering the CGRs for Alloy 82 to be a factor of 2.6 lower than those for Alloy 182. After accounting for the difference in CGRs in air for the field welds and laboratory welds, the data in Fig. 45 show some environmental enhancement of CGRs for Ni-alloy welds in the PWR environment. As with the laboratory-prepared welds, the conditions that appear to show the most environmental enhancement are loading ratios of R ≈ 0.7 and rise times of 1000 s.

Figure 46 shows images from the fracture surfaces of specimens WLR-01 and WCR-01. In specimen WLR-01, the transition from a fatigue TG crack to SCC IG crack occurred apparently readily, while in specimen WCR-01 a more mixed fracture mode occurred. Nevertheless, the reason for the lower growth rates for the field welds relative to those for the laboratory-prepared welds is not clear.

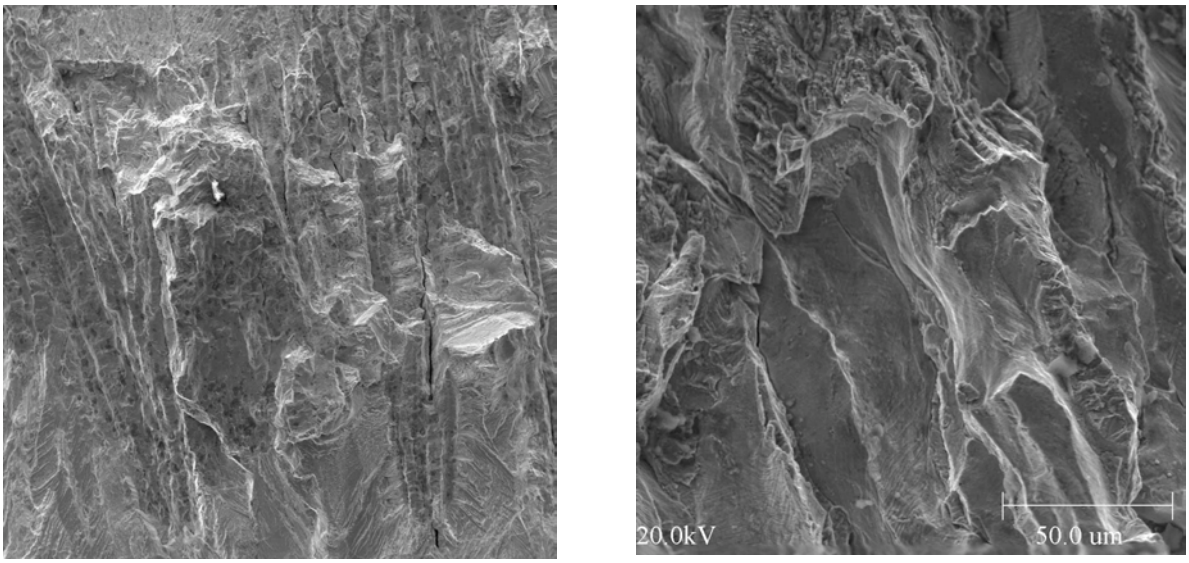

(a) (b)

Figure 46. Micrographs of the fracture surface of specimen (a) WCR-01 and (b) WLR-01. Crack advance is from top to bottom.

6 Summary

Crack growth rate results are presented for Alloy 182 SMA weld metal in the simulated PWR environment in the temperature range 290-350°C. The tests were conducted on a 1-T compact tension specimen from an Alloy 182 double-J weld and on two companion 1/2-T compact tension specimens from a deep-groove Alloy 182 weld. Metallographic examination of the fracture surfaces revealed relatively straight crack fronts. The fracture modes correlated well with the test conditions. High rise times or long hold periods favor IG SCC. Also, IG cracking apparently advanced more readily along some grain orientations than others, resulting in crack fronts with occasional unbroken ligaments and few regions of TG cracking.

In addition, metallographic examinations were performed to characterize the microstructure of the weld. The weld structure consisted of vertically columnar grains and dendrites. The weld microstructure was also examined by OIM to determine the orientations of the grains and the type of grain boundaries present. The results indicate that the intragranular dendrites are coherent and are, therefore, expected to be very resistant to cracking. The proportion of cracking-resistant, coincident-site lattice boundaries in the weld was found to be relatively small (≈30%) by comparison with that of Alloy 600 in a solution-annealed condition (≈50%). The comparison suggests that Alloy 182 is more susceptible to cracking than Alloy 600, and this inference is supported by the CGR findings presented in this report.

The activation energy for SCC crack growth in Alloy 182 SMA weld alloy was calculated from the SCC CGR vs. temperature curves. The curves yield activation energies of 252 kJ/mol for the double-J weld material and 189 kJ/mol for the deep-groove weld material. These values are in good agreement with the data reported in the literature. The data reported here and those in the literature suggest that the average activation energy for Alloy 182 welds is on the order of 220-230 kJ/mol, higher than the 130 kJ/mol commonly used for Alloy 600. The activation energy data for Alloy 82 are more limited. The average value from the literature data is about 169 kJ/mol. The consequences of using these larger values for the analysis of SCC CGR data were analyzed. The analysis showed that when an activation energy of 220 kJ/mol is used, the 75th percentile value of $\ln(\alpha)$, which has been the value used for a disposition curve, becomes -27.5396, yielding a value of 1.1×10^{-12} at 325°C for the α parameter. Thus, the disposition curve for Ni-alloy welds based on data that have been normalized with an activation energy of 220 kJ/mol is ≈36% lower than the curve based on data normalized with 130 kJ/mol; thus, the use of the 130 kJ/mol value leads to somewhat more conservative results.

In addition to the tests on laboratory prepared welds, CGR tests were performed on weldment samples from a Davis–Besse CRDM J-groove nozzle weld and from a V.C. Summer hot–leg nozzle to safe end weld. For the Davis-Besse Alloy 182 weld specimens, the SCC CGRs under constant load are an order of magnitude lower than the disposition curve proposed for Alloy 182 weld metals. For the V.C. Summer weld specimens, the CGR data under constant load were lower than data obtained by others on the same alloys and lower than the proposed disposition curve. The data from the field welds correspond to values in the lower quartile of the distribution of crack growth rate data obtained on laboratory specimens. These results are not so statistically unlikely that they can be said to prove that there is a difference between field and laboratory welds, but such a difference would be consistent with the observations that operating experience indicates that PWSCC appears to occur more frequently in wrought Ni-base Alloy 600 components than in the weld metal Alloys 82 and 182 used with Alloy 600, despite the fact that in laboratory tests in PWR coolant environments, the stress corrosion cracking (SCC) susceptibility of Alloy 182 is usually found to be greater than that of Alloy 600, while that of Alloy 82 is comparable to that of Alloy 600.

laboratory welds is the degree of structural constraint imposed on the welds during the welding process, which is typically much greater for the field welds on actual components. However, metallographic studies on the welds away from the crack planes do not show hot cracks so that the secondary cracks seem to be part of the corrosion process. Another factor that could also contribute to a difference between CGRs from field and laboratory welds are the adjustments that are often made to laboratory data to account for the non-uniformity and less than complete engagement of the crack fronts. In any case, the use of the current database developed on laboratory welds would appear to be conservative.

The report also discusses the crack growth rate results for actual Alloy 600 component material and the environment enhancement of CGRs under cyclic loading. The SCC CGRs of the Alloy 600 nozzle from Davis-Besse are a factor of 4–8 higher than those of the median curve for Alloy 600. The growth rates correspond to the ≈95th percentile of the various data sets used in developing the median curve, i.e., the nozzle material exhibits very high susceptibility to SCC. The material exhibits predominantly IG fracture, even during precracking.

The environmental enhancement of CGRs under cyclic loading was determined for the Alloy 600 and Ni-alloy welds tested relative to the CGRs that would be expected under the same loading conditions for the respective alloy in air. The cyclic CGRs were analyzed by a superposition model to establish the individual contributions of mechanical fatigue, corrosion fatigue, and SCC. Environmental enhancement was observed for solution-annealed Alloy 600 and for some specimens in the thermally treated condition. Although the results show considerable scatter, the CGRs for the Davis-Besse CRDM nozzle Alloy 600 are generally higher than those for the heats of Alloy 600 tested previously in the program. Both laboratory-prepared and field Ni-weld alloys showed minimal environmental enhancement for loading ratios $R \geq 0.5$ and rise time greater that 1000 s.

References

1. Bamford, W. H., and J. F. Hall, "A Review of Alloy 600 Cracking in Operating Nuclear Plants: Historical Experience and Future Trends ," The Vessel Penetration Inspection, Crack Growth and Repair Conference, Oct. 2, 2003, Gaithersburg, MD, 2003.

2. Scott, P., "An Analysis of Primary Water Stress Corrosion Cracking in PWR Steam Generators," Proc. of the Specialists Meeting on Operating Experience with Steam Generators, Brussels, Belgium, pp. 5-6, 1991.

3. Cattant, F., "Lessons Learnt from the Examination of Tubes Pulled from Electricite de France Steam Generators," Nucl. Eng. Des. 168, pp. 241-253, 1997.

4. Diercks, D. R., W. J. Shack, and J. Muscara, "Overview of Steam Generator Tube Degradation and Integrity Issues," Nucl. Eng. Des. 194, pp. 19-30, 1999.

5. U.S. NRC Information Notice No. 90-49, "Stress Corrosion Cracking in PWR Steam Generator Tubes," Aug. 1990.

6. U.S. NRC Information Notice No. 91-43, "Recent Incidents Involving Rapid Increases in Primary-to-Secondary Leak Rate," July 1991.

7. U.S. NRC Information Notice No. 94-05, "Potential Failure of Steam Generator Tubes with Kinetically Welded Sleeves," Jan. 1994.

8. U.S. NRC Information Notice No. 89-33, "Potential Failure of Westinghouse Steam Generator Tube Mechanical Plugs," March 1989.

9. U.S. NRC Information Notice No. 89-65, "Potential for Stress Corrosion Cracking in Steam Generator Tube Plugs Supplied by Babcock and Wilcox," Sept. 1989.

10. U.S. NRC Information Notice No. 94-87, "Unanticipated Crack in a Particular Heat of Alloy 600 Used for Westinghouse Mechanical Plugs for Steam Generator Tubes," Dec. 1994.

11. U.S. NRC Information Notice No. 90-10, "Primary Water Stress Corrosion Cracking (PWSCC) of Inconel 600," Feb. 1990.

12. U.S. NRC Generic Letter 97-01, "Degradation of Control Rod Drive Mechanism and Other Vessel Closure Head Penetrations," April 1, 1997.

13. Economou, J., A. Assice, F. Cattant, J. Salin, and M. Stindel, "NDE and Metallurgical Examination of Vessel Head Penetrations," 3rd Intl. Symp. of Fontevraud, Sept. 12-16, 1994.

14. Robinson, M. R., Duke Power Company, "Oconee Unit 1 and Unit 3 Reactor Vessel Head Leakage, Cracking of RV Head Penetrations due to Primary Water Stress Corrosion Cracking," NRC Meeting with the NEI EPRI Material Reliability Program Regarding CRDM Nozzle Cracking Issues, Rockville, MD, April 12, 2001.

15. Frye, C. R., T. Alley, M. L. Arey, Jr., and M. R. Robinson, "Cracking in Alloy 600/182 Reactor Vessel Head Penetrations," PVP-Vol. 437, Service Experience and Failure Assessment Applications ASME 2002, P. S. Lam, ed., American Society of Mechanical Engineers, New York, pp. 171-178, 2002.

16. U.S. NRC Information Notice 2001-05, "Through-Wall Circumferential Cracking of Reactor Pressure Vessel Head Control Rod Driver Mechanism Penetration Nozzle at Oconee Nuclear Station, Unit 3," April 30, 2001.

17. U.S. NRC Bulletin 2001-01, "Circumferential Cracking of Reactor Pressure Vessel Head Penetration Nozzles," Aug. 3, 2001.

18. U.S. NRC Information Notice 2000-17, "Crack in Weld Area of Reactor Coolant System Hot Leg Piping at V.C. Summer," Oct. 18, 2000; Suppl. 1, Nov. 16, 2000; Suppl. 2, Feb. 28, 2001.

19. Jenssen, A., K. Norrgard, J. Lagerstrom, G. Embring, and D. Tice, "Assessment of Cracking in Dissimilar Metal Welds," Proc. of the Tenth Intl. Conf. on Environmental Degradation of Materials in Nuclear Power Systems-Water Reactors, NACE International, Houston, TX, 2001.

20. Bennetch, J. I., G. E. Modzelewski, L. L. Spain, and G. V. Rao, "Root Cause Evaluation and Repair of Alloy 82/182 J-Groove Weld Cracking of Reactor Vessel Head Penetrations at North Anna Unit 2," PVP-Vol. 437, Service Experience and Failure Assessment Applications ASME 2002, P. S. Lam, ed., American Society of Mechanical Engineers, New York, pp. 179-185, 2002.

21. U.S. NRC Information Notice 2002-11, "Recent Experience with Degradation of Reactor Pressure Vessel Head," March 12, 2002.

22. U.S. NRC Information Notice 2003-11, "Leakage Found on Bottom-Mounted Instrumentation Nozzles," Aug. 13, 2003; Suppl. 1, Jan. 8, 2004.

23. U.S. NRC Bulletin 2003-02, "Leakage from Reactor Pressure Vessel Lower Head Penetrations and Reactor Coolant Pressure Boundary Integrity," Aug. 21, 2003.

24. Licensee Event Report 414-2001-002, Rev. 0, Nov. 12, 2001, U.S. Nuclear Regulatory Commission.

25. Licensee Event Report 255-1993-009, Rev. 1, Nov. 18, 1993, U.S. Nuclear Regulatory Commission.

26. Ruther, W. E., W. K. Soppet, and T. F. Kassner, "Corrosion Fatigue of Alloys 600 and 690 in Simulated LWR Environments," NUREG/CR-6383, ANL-95/37, April 1996.

27. Ruther, W. E., W. K. Soppet, and T. F. Kassner, "Environmentally Assisted Cracking of Alloys 600 and 690 in Simulated LWR Water," Environmentally Assisted Cracking in Light Water Reactors, Semiannual Report, July 1997-December 1997, NUREG/CR-4667, Vol. 25, ANL-98/18, pp. 42-75, Sept. 1998.

28. Ruther, W. E., W. K. Soppet, T. F. Kassner, and W. J. Shack, "Environmentally Assisted Cracking of Alloys 600 and 690 in Simulated LWR Water," Environmentally Assisted Cracking in Light Water Reactors, Semiannual Report, January 1998-July 1998, NUREG/CR-4667, Vol. 26, ANL-98/18, pp. 25-32, March 1999.

29. Ruther, W. E., W. K. Soppet, T. F. Kassner, and W. J. Shack, "Environmentally Assisted Cracking of Alloys 600 and 690 in Simulated LWR Water," Environmentally Assisted Cracking in Light Water Reactors, Semiannual Report, July 1998-December 1998, NUREG/CR-4667, Vol. 27, ANL-99/11, pp. 45-54, October 1999.

30. Soppet, W. K., O. K. Chopra, and W. J. Shack, "Environmentally Assisted Cracking of Alloys 600 and 690 in Simulated LWR Water," Environmentally Assisted Cracking in Light Water Reactors, Semiannual Report, July 1999-December 1999, NUREG/CR-4667, Vol. 29, ANL-00/23, pp. 39-45, November 2000.

31. Chopra, O. K., W. K. Soppet, and W. J. Shack, "Effects of Alloy Chemistry, Cold Work, and Water Chemistry on Corrosion Fatigue and Stress Corrosion Cracking of Nickel Alloys and Welds," NUREG/CR-6721, ANL-01/07, April 2001.

32. Alexandreanu, B., O. K. Chopra, and W. J. Shack, "Crack Growth Rates of Nickel Alloy Welds in a PWR Environment," NUREG/CR-6907, ANL-04/3, May 2006.

33. Alexandreanu, B., O. K. Chopra, and W. J. Shack, "Crack Growth Rates of Nickel Alloys from the Davis-Besse and V. C. Summer Power Plants in a PWR Environment," NUREG/CR-6921, ANL-05/55, November 2001.

34. Macdonald, D. D., A. C. Scott, and P. Wentrcek, "External Reference Electrodes for Use in High Temperature Aqueous Systems," J. Electrochem. Soc. 126, pp. 908-911, 1979.

35. Attanasio, S. A., and D. S. Morton, "Measurement of the Nickel/Nickel Oxide Transition in Ni-Cr-Fe Alloys and Updated Data and Correlations to Quantify the Effect of Aqueous Hydrogen on Primary Water SCC," Proc. 11th Intl. Conf. on Environmental Degradation of Materials in Nuclear Power Systems-Water Reactors, NACE International, Houston, TX, 2003.

36. Attanasio, S. A., D. S. Morton, M. A. Ando, N. F. Panayotou, and C. D. Thompson, "Measurement of the Nickel/Nickel Oxide Phase Transition in High Temperature Hydrogenated Water Using the Contact Electric Resistance (CER) Technique," Proc. Tenth Intl. Conf. on Environmental Degradation of Materials in Nuclear Power Systems-Water Reactors, NACE International, Houston, TX, 2001.

37. Morton, D. S., S. A. Attanasio, and G. A. Young, "Primary Water SCC Understanding and Characterization Through Fundamental Testing in the Vicinity of the Nickel/Nickel Oxide Phase Transition," Proc. Tenth Intl. Conf. on Environmental Degradation of Materials in Nuclear Power Systems-Water Reactors, NACE International, Houston, TX, 2001.

38. Andresen, P. L., and P. G. Campbell, "The Effects of Crack Closure in High-Temperature Water and its Role in Influencing Crack Growth Data," Proc. of the Fourth Intl. Symp. on Environmental Degradation of Materials in Nuclear Power Systems-Water Reactors, D. Cubicciotti, ed., NACE International, Houston, TX, pp. 4.86-4.111, 1990.

39. Cassagne, T. B., and A. Gelpi, "Crack Growth Rate Measurements on Alloy 600 Steam Generator Tubes in Steam and Primary Water," Proc. of the Fifth Intl. Symp. on Environmental Degradation of Materials in Nuclear Power Systems-Water Reactors, American Nuclear Society, La Grange Park, IL, pp. 518-524, 1991.

40. Foster, J. P., W. H. Bamford, and R. S. Pathania, "Initial Results of Alloy 600 Crack Growth Rate Testing in a PWR Environment," Proc. of the Seventh Intl. Symp. on Environmental Degradation of Materials in Nuclear Power Systems-Water Reactors, NACE International, Houston, TX, pp. 25-39, 1995.

41. Magdowski, R., F. Vaillant, C. Amzallag, and M. O. Speidel, "Stress Corrosion Crack Growth Rates of Alloy 600 in Simulated PWR Coolant," Proc. of the 8th Intl. Symp. on Environmental Degradation of Materials in Nuclear Power Systems-Water Reactors, S. M. Bruemmer, ed., American Nuclear Society, La Grange Park, IL, pp. 333-338, 1997.

42. Le Hong, S., C. Amzallag, and A. Gelpi, "Modeling of Stress Corrosion Crack Initiation on Alloy 600 in Primary Water of PWRs," Proc. of the Ninth Intl. Symp. on Environmental Degradation of Materials in Nuclear Power Systems-Water Reactors, F. P. Ford, S. M. Bruemmer, and G. S. Was, eds., Minerals, Metals, and Materials Society, Warrendale, PA, pp. 115-122, 1999.

43. Raquet, O., and G. Santarini, "Stress Corrosion Crack Propagation Rate of Alloy 600 in the Primary Water of PWR Influence of a Cold Worked Layer," Proc. of the Ninth Intl. Symp. on Environmental Degradation of Materials in Nuclear Power Systems-Water Reactors, F. P. Ford, S. M. Bruemmer, and G. S. Was, eds., Minerals, Metals, and Materials Society, Warrendale, PA, pp. 207-213, 1999.

44. White, G. A., Hickling, J., and Mathews, L. K., "Crack Growth Rates for Evaluating PWSCC of Thick-Wall Alloy 600 Material," Proc. of the 11th Intl. Symp. on Environmental Degradation of Materials in Nuclear Power Systems-Water Reactors, NACE International, Houston, TX, pp. 166-179, 2003.

45. White, G., J. Hickling, and C. Harrington, "MRP Development of Crack Growth Rate Disposition Curves for Primary Water Stress Corrosion Cracking (PWSCC) of Thick-Section Alloy 600 Components and Alloy 82, 182 and 132 Weldments," 2005 EPRI International PWSCC of Alloy 600 Conference, Santa Ana Pueblo, NM, March 7-10, 2005.

46. Palumbo, G., K. T. Aust, E.M. Lehockey, U. Erb, and P. Lin, "On a More Restrictive Geometric Criterion for 'Special' CSL Grain Boundaries," Acta Metallurgica, 14, pp. 1685-1690, 1998.

47. Was, G., V. Thaveeprungsriporn, and D. C. Crawford, "Grain Boundary Misorientation Effects on Creep and Cracking in Ni-Based Alloys," Journal of Materials, 50 (2), pp. 44-49, 1998.

48. Alexandreanu, B., B. Capell, and G. S. Was, "Combined Effect of Special Grain Boundaries and Grain Boundary Carbides on IGSCC of Ni-16Cr-9Fe-xC Alloys," Materials Science and Engineering A, 300, pp. 94-104, 2001.

49. Palumbo, G., P.J. King, and K.T. Aust, "Grain Boundary Design and Control for Intergranular Stress Corrosion Resistance," Scripta Metallugica et Materialia, 25 (8), pp. 1775-1780, 1991.

50. Cheung, C., U. Erb, and G. Palumbo, "Application of Grain Boundary Engineering Concepts to Alleviate Intergranular Cracking in Alloys 600 and 690," Materials Science and Engineering A, 185, pp. 39-43, 1994.

51. Pan, Y., B. L. Adams, T. Olson, and N. Panayotou, "Grain-Boundary Structure Effects on Intergranular Stress Corrosion Cracking of Alloy X-750," Acta Materialia, 44 (12), pp. 4685-4695, 1996.

52. Lehockey, E. M., A.M. Brennenstuhl, and I. Thompson, "On the Relationship between Grain Boundary Connectivity, Coincident Site Lattice Boundaries, and Intergranular Stress Corrosion Cracking," Corrosion Science, 46, pp. 2383-2404, 2004.

53. Shei, S. A., and W. J. Wang, "Stress Corrosion Crack Tip Microstructure in Nickel-base Alloys," Proc. Corrosion 94, National Association of Corrosion Engineers International Annual Conference, NACE International, Houston, TX, 1994.

54. Alexandreanu, B., and G. S. Was, "Grain Boundary Deformation-Induced Intergranular Stress Corrosion Cracking of Ni-16Cr-9Fe in 360°C Water," Corrosion 59 (8), pp. 705, 2003.

55. Amzallag, C., G. Baudry, and J. L. Bernard, "Effects of PWR Environment on the Fatigue Crack Growth of Different Stainless Steels and Inconel Type Alloy," Proc. IAEA-Specialists Meeting on Subcritical Crack Growth, NUREG/CP-0044, Vol. 1, pp. 263-294, 1983.

56. James, L. A., and W. J. Mills, "Fatigue-Crack Propagation Behavior of Wrought Alloy 600 and Weld-Deposited EN82H in an Elevated Temperature Aqueous Environment," Service Experience, Structural Integrity, Severe Accident, and Erosion in Nuclear and Fossil Plants, PVP Vol. 303, The American Society of Mechanical Engineers, pp. 21-36, 1995.

57. Van Der Sluys, W. A., B. A. Young, and D. Doyle, "Corrosion Fatigue Properties on Alloy 690 and some Nickel-Based Weld Metals," Assessment Methodologies for Preventing Failure: Service Experience and Environmental Considerations, PVP Vol. 410-2, R. Mohan, ed., American Society of Mechanical Engineers, New York, pp. 85-91, 2000.

58. Lindstrom, R., P. Lidar, and J. Lagerstrom, "Crack Growth of Alloy 182 in Simulated Primary Side PWR Environment," Proc. of the 8th Intl. Symp. on Environmental Degradation of Materials in Nuclear Power Systems-Water Reactors, S. M. Bruemmer, ed., American Nuclear Society, La Grange Park, IL, pp. 422-429, 1997.

59. Brown, C. M., and W. J. Mills, "Effect of Water on Mechanical Properties and Stress Corrosion Behavior of Alloy 600, Alloy 690, EN82H Welds, and EN52 Welds," Corrosion, 55 (2), pp. 173-186, 1999.

60. Mills, W. J., and C. M. Brown, "Stress Corrosion Crack Growth Rates for Alloy 82H Welds in High Temperature Water," Proc. 11th Intl. Conf. on Environmental Degradation of Materials in Nuclear Power Systems-Water Reactors, NACE International, Houston, TX, 2003.

61. Magdowski, R., and M. Speidel, "Stress Corrosion Crack Growth of Weld Material Alloy 182 in Simulated PWR Environments," Institute of Metallurgy, Swiss Federal Institute, Internal Report No. 226, Zurich, Jan. 2001.

62. Attanasio, S., J. V. Mullen, J. W. Wuthrich, W. W. Wilkening, and D. S. Morton, "Stress Corrosion Crack Growth Rates (SCCGRs) for Alloy 182 and 82 Welds," The Vessel Penetration Inspection, Crack Growth and Repair Conference, Gaithersburg, MD, 2003.

63. Bamford, W. H., J. P. Foster, and R. S. Pathania, "An Investigation of Alloy 182 Stress Corrosion Cracking in Simulated PWR Environment," Proc. of the Ninth Intl. Symp. on Environmental Degradation of Materials in Nuclear Power Systems-Water Reactors, F. P. Ford, S. M. Bruemmer, and G. S. Was, eds., The Minerals, Metals, and Materials Society, Warrendale, PA, pp. 279-294, 1999.

64. Bamford, W. H., J. P. Foster, K. R. Hsu, L. Tunon-Sanur, and A. McIlree, "Alloy 182 Weld Crack Growth, and its Impact on Service-Induced Cracking in Operating PWR Plant Piping," Proc. Tenth Intl. Conf. on Environmental Degradation of Materials in Nuclear Power Systems-Water Reactors, NACE International, Houston, TX, 2001.

65. Cassagne, T., D. Caron, J. Daret, and Y. Lefevre, "Stress Corrosion Crack Growth Rate Measurements in Alloys 600 and 182 in Primary Loops Under Constant Load," Proc. of the Ninth Intl. Symp. on Environmental Degradation of Materials in Nuclear Power Systems-Water Reactors, F. P. Ford, S. M. Bruemmer, and G. S. Was, eds., The Minerals, Metals, and Materials Society, Warrendale, PA, pp. 217-224, 1999.

66. Le Hong, S., J. M. Boursier, C. Amzallag, and J. Daret, "Measurement of Stress Corrosion Cracking Growth Rates in Weld Alloy 182 in Primary Water of PWR," Proc. Tenth Intl. Conf. on Environmental Degradation of Materials in Nuclear Power Systems-Water Reactors, NACE International, Houston, TX, 2001.

67. Jacko, R. J., R. E. Gold, G. V. Rao, K. Koyama, and A. Kroes, "Results of Accelerated SCC Testing of Alloy 82, Alloy 182 and Alloy 52M Weld Metals," The Vessel Penetration Inspection, Crack Growth and Repair Conference, Gaithersburg, MD, 2003.

68. Tsutsumi, K., H. Kanasaki, K. Yoshimoto, Y. Nomura, S. Asada, and T. Yonezawa, "SCC Growth Rate of Nickel Based Alloy 132 Weld Metal in PWR Water," Proc. 11th Intl. Conf. on Environmental Degradation of Materials in Nuclear Power Systems-Water Reactors, NACE International, Houston, TX, 2003.

Appendix A: Crack Growth Rate Data for Davis-Besse and V. C. Summer Ni-base alloys

A.1 Specimen N3CL-1 of Alloy 600 in PWR water at 316°C

Table A1. Crack growth results for 1/4–T CT specimen N3CL-1 of Alloy 600 in PWR water[a] at 316°C

Test Period	Test Time, (h)	Conduc - tivity (μS/cm)	R Load Ratio	Rise Time, (s)	Down Time, (s)	Hold Time, (s)	K_{max}, (MPa $m^{1/2}$)	ΔK, (MPa $m^{1/2}$)	Growth Rate, (m/s)	Allowed K_{max}, (MPa $m^{1/2}$)	Kapp – K_{max},[b] (%)	Crack Length (mm)
Pre a	51	21.0	0.26	1	1	0	19.0	14.1	5.07E-09	20.3	-6	5.993
Pre b	71	–	0.28	5	5	0	18.4	13.3	3.09E-09	20.1	-8	6.117
1	115	–	0.53	30	4	0	20.0	9.4	4.30E-10	19.9	1	6.199
2	194	18.5	0.54	300	4	0	20.3	9.4	2.55E-10	19.9	2	6.240
3a	225	18.5	0.52	300	4	0	21.5	10.3	8.88E-11	19.8	9	6.269
3b	316	14.7	0.51	300	4	0	23.2	11.4	2.63E-10	19.7	18	6.353
4	436	12.8	0.71	300	4	0	24.0	7.0	1.10E-10	19.6	22	6.400
5	676	15.4	0.70	1000	12	0	23.1	6.9	negligible	19.6	18	6.398
6	722	15.4	0.51	300	4	0	23.7	11.6	4.42E-10	19.5	22	6.471
7a	818	13.0	0.50	1000	12	0	23.2	11.6	5.45E-11	19.4	20	6.493
7b	868	13.0	0.51	1000	12	0	24.2	11.8	3.73E-10	19.3	25	6.562

[a]Simulated PWR water with 2 ppm Li, 1000 ppm B, and ≈2 ppm dissolved hydrogen. Effluent DO was <10 ppb.
[b]Based on flow stress.

A.2 Specimen N3CC-2 of Alloy 600 in PWR water at 316°C

Table A2. Crack growth data for 1/4–T CT specimen N3CC-2 of Alloy 600 in PWR water[a] at 316°C

Test Period	Test Time, (h)	Conduc - tivity (μS/cm)	R Load Ratio	Rise Time, (s)	Down Time, (s)	Hold Time, (s)	K_{max}, (MPa $m^{1/2}$)	ΔK, (MPa $m^{1/2}$)	Growth Rate, (m/s)	Allowed K_{max}, (MPa $m^{1/2}$)	Kapp – K_{max},[b] (%)	Crack Length (mm)
Pre a	189	22	0.31	5	5	0	21.9	15.1	7.52E-10	19.8	10	6.243
1	383	20	0.51	300	4	0	21.1	10.3	2.13E-11	19.8	6	6.270
2	457	17	0.51	30	4	0	21.7	10.6	6.05E-11	19.7	10	6.335
3	550	16	0.51	300	4	0	21.6	10.6	9.46E-12	19.7	10	6.338
4	580	15	0.51	30	4	0	23.6	11.5	8.59E-10	19.5	20	6.415
5	765	15	0.50	300	12	0	23.5	11.7	8.87E-11	19.5	21	6.471
6	885	15	0.70	300	12	0	23.7	7.1	5.28E-11	19.4	22	6.492
7	912	16	0.51	300	12	0	23.7	11.6	1.01E-10	19.4	22	6.502
8	1197	20	0.52	300	12	3600	24.3	11.7	6.92E-11	19.3	26	6.541
9	1365	21	0.48	300	12	0	23.2	12.1	7.53E-11	19.3	25	6.617
10	1530	21	1.00	–	–	–	23.3	–	9.67E-11	19.2	21	6.658

[a]Simulated PWR water with 2 ppm Li, 1000 ppm B, and ≈2 ppm dissolved hydrogen. Effluent DO was <10 ppb.
[b]Based on flow stress.

A.3 Specimen N3CC-3 of Alloy 600 in PWR water at 316°C

Table A3. Crack growth data for specimen N3CC-3 of Alloy 600 in PWR water[a] at 316°C

Test Period	Test Time, (h)	Conduc - tivity (μS/cm)	R Load Ratio	Rise Time, (s)	Down Time, (s)	Hold Time, (s)	K_{max}, (MPa $m^{1/2}$)	ΔK, (MPa $m^{1/2}$)	Growth Rate, (m/s)	Allowed K_{max}, (MPa $m^{1/2}$)	Kapp – K_{max},[b] (%)	Crack Length (mm)
Pre a	50	20	0.36	0.25	0.25	0	19.7	12.6	1.35E-08	27.6	-29	12.777
Pre b	55	20	0.35	0.25	0.25	0	19.1	12.4	8.41E-09	27.5	-30	12.872
Pre c	72	19	0.33	5.0	5.0	0	18.8	12.6	2.03E-09	27.4	-31	12.943
Pre d	78	19	0.32	0.5	0.5	0	19.6	13.3	1.31E-08	27.2	-28	13.065
1	97	18	0.50	12	4	0	19.5	9.7	9.08E-10	27.1	-28	13.157
2	122	18	0.49	60	4	0	19.6	10.0	3.55E-10	27.1	-28	13.186
3	147	18	0.48	300	4	0	19.8	10.3	2.80E-10	27.1	-27	13.206
4	174	17	0.63	1,000	12	0	20.0	7.4	2.18E-10	27.0	-26	13.249
5a	230	16	1.00	-	-	-	19.3	0.0	7.85E-11	27.1	-29	13.218
5b	339	15	1.00	-	-	-	19.7	0.0	1.25E-10	26.9	-27	13.319
6a	386	14	1.00	-	-	-	24.9	0.0	2.28E-10	26.8	-7	13.404
6b	529	12	1.00	-	-	-	25.1	0.0	1.55E-10	26.7	-6	13.510
7	648	12	1.00	-	-	-	30.1	0.0	negligible	26.5	13	13.637

[a]Simulated PWR water with 2 ppm Li, 1000 ppm B, and ≈2 ppm dissolved hydrogen. Effluent DO was <10 ppb.
[b]Based on flow stress.

A.4 Specimen J11CC-1 of Alloy 182 J–groove weld in PWR water at 316°C

Table A4. Crack growth data for specimen J11CC-1 of Alloy 182 J–groove weld in PWR water[a] at 316°C.

Test Period	Test Time, (h)	Conductivity (µS/cm)	R - Load Ratio	Rise Time, (s)	Down Time, (s)	Hold Time, (s)	K_{max}, (MPa $m^{1/2}$)	ΔK, (MPa $m^{1/2}$)	Growth Rate, (m/s)	Allowed K_{max}, (MPa $m^{1/2}$)	$K_{app} - K_{max}$,[c] (%)	Crack Length (mm)
Pre a	145	17.2	0.32	0.5	0.5	0	21.3	14.8	4.05E-08	20.9	2	6.153
Pre b	186	17.2	0.32	50	50	0	20.6	14.3	1.27E-09	20.7	0	6.264
1	331	15.6	0.51	300	4	0	20.6	10.3	1.13E-10	20.5	1	6.333
2	453	13.0	0.70	1000	12	0	21.4	6.5	5.71E-12	20.5	4	6.342
3a	644	22.2	0.51	1000	12	0	21.2	10.8	3.88E-11	20.5	4	6.363
3b	745	20.0	0.50	1000	12	0	21.1	10.7	negligible	20.4	3	6.382
4	937	14.7	0.50	1000	12	0	22.5	11.5	8.25E-12	20.4	10	6.392
5	987	14.7	0.50	300	12	0	22.5	11.5	5.53E-11	20.4	10	6.401
6	1106	18.2	0.49	300	12	3600	22.6	11.6	negligible	20.4	11	6.402
7	1178	18.9	0.52	30	4	0	22.9	11.2	7.93E-10	20.2	13	6.525
8	1248	17.2	0.49	300	12	0	22.9	11.9	1.06E-10	20.1	14	6.550
9	1415	16.1	0.49	300	12	3600	22.9	6.0	negligible	20.2	14	6.543
10	1443	18.2	0.49	30	12	0	23.2	12.1	1.13E-09	20.0	16	6.616
11	1513	18.5	0.49	300	12	0	27.3	14.2	3.00E-10	19.8	38	6.742
12a	1548	18.5	0.49	300	12	3600	27.6	14.3	3.98E-11[d]	19.8	40	6.747
12b	1607	18.2	0.52	300	12	3600	29.9	0.0	3.01E-11[e]	19.7	52	6.777
13	1948	16.7	1.0	–	–	–	28.5	0.0	2.20E-11[f]	19.7	45	6.797

[a]Simulated PWR water with 2 ppm Li, 1000 ppm B, and ≈2 ppm dissolved hydrogen. Effluent DO was <10 ppb.
[b]Based on flow stress.
[d]Based on total crack extension during the period. From superposition model, CGR during the constant load was estimated to 1.68E-11 m/s.
[e]From superposition model, CGR during the constant load was estimated to 1.63E-11 m/s.
[f]Based on total crack extension during the period.

A.5 Specimen J11CC-3 of Alloy 182 J–groove weld in PWR water at 316°C

Table A5. Crack growth data for specimen J11CC-3 of Alloy 182 J–groove weld in PWR water[a] at 316°C

Test Period	Test Time, (h)	Conduc - tivity (μS/cm)	R Load Ratio	Rise Time, (s)	Down Time, (s)	Hold Time, (s)	K_{max}, (MPa $m^{1/2}$)	ΔK, (MPa $m^{1/2}$)	Growth Rate, (m/s)	Allowed K_{max}, (MPa $m^{1/2}$)	Kapp – K_{max},[b] (%)	Crack Length (mm)
Pre a	78	21	0.31	0.25	0.25	0	17.8	12.3	6.55E-08	29.4	-39	12.373
Pre b	104	21	0.32	10	10	0	17.9	12.2	7.17E-09	29.1	-38	12.605
1	221	18	0.50	60	4	0	18.7	9.4	7.44E-10	28.5	-34	13.049
2	412	20	0.51	300	12	0	18.8	9.2	1.33E-10	28.4	-34	13.134
3	507	20	1.00	–	–	–	18.9	0.0	3.92E-11[c]	28.5	-34	13.099
4	580	19	0.50	300	12	0	20.8	10.4	2.30E-10	28.3	-26	13.233
5	742	15	0.50	1000	12	0	21.0	10.5	7.12E-11	28.3	-26	13.254
6a	864	13	1.00	–	–	–	21.0	0.0	3.93E-11[c]	28.3	-26	13.204
6b	934	13	0.51	12	12	3600	20.9	10.2	3.66E-11	28.3	-26	13.204
7a	937	13	0.51	1000	12	0	21.0	10.3	–	28.3	-26	13.240
7b	941	19	0.70	1000	12	0	26.5	8.0	–	28.2	-6	13.295
8	1079	33	0.70	12	12	3600	26.6	8.0	4.00E-11	28.2	-6	13.271
9	1084	33	0.70	1000	12	0	26.8	8.0	–	28.2	-5	13.312
10	1248	31	0.70	12	12	3600	30.9	9.3	4.65E-11	28.2	10	13.327
11	1349	29	0.70	1000	12	0	31.0	9.3	8.23E-11	28.0	10	13.410
12	1516	28	0.70	12	12	3600	30.7	9.2	negligible	28.1	9	13.368
13	1537	28	0.70	300	12	0	30.9	9.3	–	28.0	10	13.405

[a]Simulated PWR water with 2 ppm Li, 1000 ppm B, and ≈2 ppm dissolved hydrogen. Effluent DO was <10 ppb.
[b]Based on flow stress.
[c]Values estimated from the total crack extension during the test period and not from the slope of the crack length vs. time plot.

A.6 Specimen WCR–01 of Alloy 82 weld in PWR water at 320°C

Table A6. Crack growth results for specimen WCR–01 of Alloy 82 weld in PWR water[a] at 320°C.

Test Period	Test Time, (h)	O_2 Conc., (ppb)	Load Ratio R	Rise Time, (s)	Down Time, (s)	Hold Time, (s)	K_{max},[b] (MPa $m^{1/2}$)	ΔK, (MPa $m^{1/2}$)	CGR_{env}, (m/s)	Estimated CGR_{air}, (m/s)	Crack Length, (mm)
Pre a	100	<10	0.32	1	1	0	22.9	15.5	2.83E-09	4.16E-08	12.289
Pre b	124	<10	0.31	0.5	0.5	0	22.8	15.8	4.86E-09	8.60E-08	12.351
Pre c	140	<10	0.29	5	5	0	21.9	15.6	1.72E-09	7.80E-09	12.379
Pre d	146	<10	0.30	0.25	0.25	0	22.7	15.9	9.34E-09	1.72E-07	12.484
1	258	<10	0.30	30	2	0	22.9	11.4	1.39E-10	6.34E-10	12.649
2	380	<10	0.51	30	2	0	22.4	11.0	2.06E-10	5.58E-10	12.736
3	523	<10	0.50	300	12	0	22.4	11.2	3.18E-11	5.95E-11	12.779
4	593	<10	1.00	–	–	–	22.9	0.0	4.11E-11	–	12.789

[a]Simulated PWR water with 2 ppm Li, 1000 ppm B, and ≈2 ppm dissolved hydrogen. Conductivity was 22 ± 3 µS/cm, and pH was 6.4.

[b]At the end of the test the maximum allowed K_{max} based on the final load was 28.8 MPa $m^{1/2}$.

A.7 Specimen BCR–01 of Alloy 82 SMA weld in PWR water at 320°C

Table A7. Crack growth data for specimen BCR–01 of Alloy 182 SMA weld in PWR water[a] at 320°C

Test Period	Test Time, (h)	O_2 Conc., (ppb)	Load Ratio R	Rise Time, (s)	Down Time, (s)	Hold Time, (s)	K_{max},[b] (MPa $m^{1/2}$)	ΔK, (MPa $m^{1/2}$)	CGR_{env}, (m/s)	Estimated CGR_{air}, (m/s)	Crack Length, (mm)
Pre a	31.0	<10	0.30	0.25	0.25	0	20.0	14.0	4.00E-09	1.03E-07	12.046
Pre b	54.0	<10	0.30	0.25	0.25	0	20.7	14.5	1.82E-08	1.20E-07	12.269
Pre c	71.0	<10	0.30	0.25	0.25	0	21.2	14.6	2.50E-08	1.27E-07	12.407
Pre d	75.0	<10	0.30	0.25	0.25	0	20.7	14.3	2.42E-08	5.75E-08	12.573
1	386.0	<10	1.00	–	–	–	20.8	0.0	2.35E-11	-	12.616
2a	389.0	<10	0.50	0.25	0.25	0	24.2	12.1	1.49E-08	9.76E-08	12.715
2b	413.0	<10	0.50	0.25	0.25	0	24.4	12.2	1.25E-08	1.00E-07	12.905
3	507.0	<10	0.50	50	2	0	25.2	12.6	3.16E-10	5.76E-10	13.041
4	839.0	<10	1.00	–	–	–	25.4	0.0	2.34E-11	-	13.057
5	842.0	<10	0.30	1	1	0	28.0	19.6	5.04E-08	1.02E-07	13.291
6a	845.0	<10	0.50	1	1	0	27.9	13.9	8.18E-09	4.36E-08	13.369
6b	869.0	<10	0.50	1	1	0	28.7	14.3	9.17E-09	4.88E-08	13.514
7	939.0	<10	0.50	300	12	0	28.8	14.4	2.79E-10	1.66E-10	13.569
8	1,340.0	<10	1.00	–	–	–	30.2	0.0	4.49E-11	-	13.594
9	1,343.0	<10	0.30	1	1	0	33.0	23.1	5.73E-08	2.01E-07	13.791
10	1344.0	<10	0.50	1	1	0	33.6	16.8	1.44E-08	9.36E-08	13.869
11	1346.0	<10	0.50	300	12	0	33.2	16.6	5.78E-10	2.95E-10	13.901
12	1702.0	<10	1.00	–	–	–	33.9	0.0	4.14E-11	-	13.930

[a]Simulated PWR water with 2 ppm Li, 1000 ppm B, and ≈2 ppm dissolved hydrogen. Conductivity was 22 ± 3 µS/cm, and pH was 6.4.

[b]At the end of the test the maximum allowed K_{max} based on the final load was 27.5 MPa $m^{1/2}$.

A.8 Specimen WLR–01 of Alloy 82 SMA weld in PWR water at 320°C

Table A8. Crack growth data for specimen WLR–01 of Alloy 82 SMA weld in PWR water[a] at 320°C.

Test Period	Test Time, (h)	O_2 Conc. (ppb)	Load Ratio R	Rise Time, (s)	Down Time, (s)	Hold Time, (s)	K_{max},[b] (MPa $m^{1/2}$)	ΔK, (MPa $m^{1/2}$)	CGR_{env}, (m/s)	Estimated CGR_{air}, (m/s)	Crack Length, (mm)
Pre a	103	<10	0.30	0.5	0.5	0	19.8	13.8	8.22E-09	5.05E-08	12.640
Pre b	167	<10	0.30	50	2	0	19.6	9.8	2.61E-10	2.12E-10	12.719
Pre c	196	<10	0.30	1	1	0	16.7	8.4	1.35E-10	5.54E-09	12.729
Pre d	215	<10	0.30	0.5	0.5	0	19.7	9.8	2.82E-09	2.15E-08	12.837
Pre e	226	<10	0.30	0.25	0.25	0	19.3	13.5	1.20E-08	9.13E-08	13.017
Pre f	265	<10	0.50	1	1	0	23.0	11.5	1.52E-08	2.04E-08	14.251
1	315	<10	0.50	50	2	0	22.6	11.3	5.93E-10	3.73E-10	14.349
2	389	<10	0.70	1000	12	0	22.8	7.1	2.31E-10	5.35E-12	14.418
3	504	<10	0.70	1000	12	0	23.5	7.7	1.60E-10	6.96E-12	14.531
4	841	<10	1.00	-	-	-	23.2	0.0	2.07E-11	-	14.531
5	1082	<10	1.00	-	-	-	31.2	0.0	5.43E-12	-	14.590
6	1203.0	<10	0.70	1000	12	0	31.0	9.3	2.04E-11	1.71E-11	14.590
7	1392.0	<10	0.70	300	12	0	31.3	9.4	1.94E-11	6.01E-11	14.602
8	1398.0	<10	0.30	0.5	0.5	0	34.7	24.3	1.03E-07	5.03E-07	15.614
9	1417.0	<10	0.50	100	12	0	38.1	19.1	7.01E-09	1.62E-09	16.099
10	1439.0	<10	0.50	300	12	0	41.9	20.9	8.00E-08	7.95E-10	16.410
11	1466.0	<10	0.50	50	2	0	43.7	21.8	2.03E-09	5.55E-09	16.656
12	1531.0	<10	0.50	300	12	0	44.6	22.3	8.95E-10	1.00E-09	16.854
13	1634.0	<10	0.50	1000	12	0	46.6	23.3	4.12E-10	3.60E-10	16.964
14	2469.0	<10	1.00	-	-	-	49.8	0.0	7.71E-11	-	17.182

[a]Simulated PWR water with 2 ppm Li, 1000 ppm B, and ≈2 ppm dissolved hydrogen. Conductivity was 22 ± 3 µS/cm, and pH was 6.4.

[b]At the end of the test the maximum allowed K_{max} based on the final load was 21.7 MPa $m^{1/2}$.

NRC FORM 335 (9-2004) NRCMD 3.7

U.S. NUCLEAR REGULATORY COMMISSION

BIBLIOGRAPHIC DATA SHEET

(See instructions on the reverse)

1. REPORT NUMBER (Assigned by NRC, Add Vol., Supp., Rev., and Addendum Numbers, if any.)

NUREG/CR 6964
ANL- 07/12

2. TITLE AND SUBTITLE

Crack Growth Rates and Metallographic Examinations of Alloy 600 and Alloy 82/182 from Field Components and Laboratory Materials Tested in PWR Environments

3. DATE REPORT PUBLISHED

MONTH	YEAR
May	2008

4. FIN OR GRANT NUMBER

Y6388

5. AUTHOR(S)

B. Alexandreanu, O. K. Chopra, and W. J. Shack

6. TYPE OF REPORT

Technical

7. PERIOD COVERED *(Inclusive Dates)*

February 2007

8. PERFORMING ORGANIZATION - NAME AND ADDRESS *(If NRC, provide Division, Office or Region, U.S. Nuclear Regulatory Commission, and mailing address; if contractor, provide name and mailing address.)*

Argonne National Laboratory
9700 South Cass Avenue
Argonne, IL 60439

9. SPONSORING ORGANIZATION - NAME AND ADDRESS *(If NRC, type "Same as above"; if contractor, provide NRC Division, Office or Region, U.S. Nuclear Regulatory Commission, and mailing address.)*

Division of Fuels, Engineering and Radiological Research
Office of Nuclear Regulatory Research
U.S. Nuclear Regulatory Commission
Washington, DC 20555-0001

10. SUPPLEMENTARY NOTES

Samantha Crane and Hipolito J. Gonzalez, NRC Project Managers

11. ABSTRACT *(200 words or less)*

In light water reactors, components made of nickel-base alloys are susceptible to environmentally assisted cracking. This report summarizes the crack growth rate results and related metallography for field and laboratory-procured Alloy 600 and its weld alloys tested in pressurized water reactor (PWR) environments. The report also presents crack growth rate (CGR) results for a shielded-metal-arc weld of Alloy182 in a simulated PWR environment as a function of temperature between 290°C and 350°C. These data were used to determine the activation energy for crack growth in Alloy 182 welds. The tests were performed by measuring the changes in the stress corrosion CGR as the temperatures were varied during the test. The difference in electrochemical potential between the specimen and the Ni/NiO line was maintained constant at each temperature by adjusting the hydrogen overpressure on the water supply tank. The CGR data as a function of temperature yielded activation energies of 252 kJ/mol for a double-J weld and 189 kJ/mol for a deep-groove weld. These values are in good agreement with the data reported in the literature. The data reported here and those in the literature suggest that the average activation energy for Alloy 182 welds is on the order of 220-230kJ/mol, higher than the 130 kJ/mol commonly used for Alloy 600. The consequences of using a larger value of activation energy for SCC CGR data analysis are discussed.

12. KEY WORDS/DESCRIPTORS *(List words or phrases that will assist researchers in locating the report.)*

Crack Growth Rate
Stress Corrosion Cracking
Alloy 600
Ni-base welds
PWR Environment

13. AVAILABILITY STATEMENT

unlimited

14. SECURITY CLASSIFICATION

(This Page)

unclassified

(This Report)

unclassified

15. NUMBER OF PAGES

16. PRICE